DEPARTMENT OF CHEMISTRY
UNIVERSITY OF JYVÄSKYLÄ
RESEARCH REPORT No. 147

CATALYTIC ACTIVITY OF PALLADIUM-BASED NANOSTRUCTURES IN THE CONVERSION OF SIMPLE OLEFINIC HYDRO- AND CHLOROHYDROCARBONS FROM FIRST PRINCIPLES

BY
JENNI ANDERSIN

Academic Dissertation
for the Degree of
Doctor of Philosophy

To be presented, by permission of the Faculty of Mathematics and Science of the University of Jyväskylä, for public examination in Auditorium FYS1, on November 29th 2011, at 12 o'clock noon

Jyväskylä, Finland
ISBN 978-951-39-4461-2 (nid.)
ISSN 0357-346X
ISBN 978-951-39-4966-2 (PDF)

Preface

The work presented in this thesis was carried out at the Nanoscience Center (NSC) of the University of Jyväskylä during 2007-2011. Funding from the Academy of Finland through project 118532, and travel grants from National Graduate School in Nanoscience and Technical University of Denmark are gratefully acknowledged.

I was lucky to have Dr. Karoliina Honkala as my supervisor; I could not have hoped for a more dedicated, professional, and friendly mentor throughout the five years of research. I want to acknowledge the fruitful collaboration with Dr. Núria López, MSc. Lauri Nykänen, and MSc. Pauli Parkkinen. I warmly thank Dr. Vesa Apaja, MSc. Perttu Luukko, Dr. Esa Räsänen, and Dr. Sami Malola for helping me out with some computer and software related technical issues. I am thankful to associate professor Anders Hellman and professor Matti Hotokka for their detailed evaluation with kind and constructive comments of the present thesis. Dr. Andre Clayborne is warmly thanked for revising the language. I also want to express my thanks to Professors Hannu Häkkinen and Robert van Leeuwen for shedding light on the fields of materials science and density functional theory.

I have been privileged to conduct my work surrounded by brilliant and delightful people. MSc. Tero Isotalo, Dr. Thomas Kühn, MSc. Petri Myöhänen, Dr. Michael Ruggenthaler, MSc. Minna Nevala, Dr. Pentti Frondelius, Dr. Adrian Stan, MSc. Anna-Maija Uimonen, Dr. Klaas Giesbertz, Dr. Olga Lopez-Acevedo, MSc. Johan Lindgren, MSc. Liisa Antila, Dr. Claudia Rocha and those who come to mind after this is printed, our discussions have been inspirational and I truly value the things I have learned from you concerning science, life, the universe and everything. Also I would like to thank the NSC people in general for making the working atmosphere receptive, warm, and fun.

I am most grateful to my family and friends outside the university for being wonderful company on this journey on the 3rd rock from the sun. Especially warm thanks to my parents, Jouko and Pirjo, for the inexhaustible support and encouragement you have provided. Finally thank you Lauri, my soul mate and husband, for making everything worthwhile.

Jyväskylä, October 2011

Jenni Andersin

Abstract

In the work presented in this thesis density functional theory calculations are carried out to study Pd-catalyzed decomposition of ethene and hydrodechlorination of trichloroethene. The focus is in the search of active surface structures, and in the identification of probable reaction mechanisms.

Our results show that under low coverage ethylene dehydrogenates over Pd(111) via CH_2-CH_2* → CH-CH_2* (CH_2-CH_3*) → CH-CH_3* → C-CH_3* → C-CH_2* → C-CH* → C-C*. The step edges scramble the picture only at the very end of the reaction coordinate by facilitating C-C bond breaking over dehydrogenation at C-CH level. Although the steps do not promote selectivity among the C-H and C-C activations, they bring down the barriers for the elementary reactions. Steps also facilitate the incorporation of carbon into the immediate subsurface area, from where the atoms move to decorate the step edges.

Trichloroethene hydrodechlorination mechanism is found to follow CCl_2C-ClH* → CCl-CClH* → CCl-CH* → C-CH* → C-CH_2* → CH-CH_2* → CH_2-CH_2*. Surface chlorine resulting from the dehalogenations weakens the binding of the adsorbates and reduces the gap between the dechlorination and hydrogenation barriers, but is not expected to affect the overall reaction route. The change in Gibbs free energy between the gas phase molecule and the activated surface species explain the experimentally observed reactivity ordering among chlorinated ethenes: Although vinyl chlorine has a stronger C-Cl bond than TCE, it dechlorinates faster when introduced from the gas phase to the catalyst surface.

The active and resistant Pd/Au core-shell structures for room temperature TCE HDC were identified as 2D Pd islands on Au nanoparticle. According to the formation energies, these structures are the most stable ones, if no intermixing of Pd into the Au is allowed. Although the mixed structures are found energetically more favorable, they bind reactants poorly. Thus, the barriers for intermixing are presumably not crossed at room temperature, which is in unison with several experimental studies. The Au(111) supported Pd island was calculated to offer clearly more reactive ground for TCE HDC compared to pure Pd(111) in terms of activation barriers and reaction energies.

Author's address Jenni Andersin
Department of Chemistry
University of Jyväskylä
Finland

Supervisor Docent Karoliina Honkala
Department of Chemistry
University of Jyväskylä
Finland

Reviewers Associate Professor Anders Hellman
Competence Centre for Catalysis and Department of Applied Physics
Chalmers University of technology
Sweden

Professor Matti Hotokka
Laboratory of Physical Chemistry
Åbo Akademi University
Finland

Opponent Senior Staff Scientist Thomas Bligaard
SUNCAT Center for Interface Science and Catalysis
Stanford University
USA

List of publications

I J. Andersin, N. Lopez and K. Honkala. *DFT Study on the Complex Reaction Networks in the Conversion of Ethylene to Ethylidyne on Flat and Stepped Pd.* J. Phys. Chem. C **113**, 8278 (2009).

II L. Nykänen, J. Andersin and K. Honkala. *First-principles calculations of the initial incorporation of carbon into flat and stepped Pd surfaces.* Phys. Rev. B **81**, 075417 (2010).

III J. Andersin and K. Honkala. *DFT study on complete ethylene decomposition on flat and stepped Pd* . Surf. Sci. **604**, 762 (2010).

IV J. Andersin and K. Honkala *First principles investigations of Pd-on-Au nanostructures for trichloroethene catalytic removal from groundwater.* PCCP **13**, 1386 (2010).

V J. Andersin, P. Parkkinen and K. Honkala *Palladium-catalyzed hydrodehalogenation of chlorinated olefins: Theoretical insights into the reaction mechanism.* Manuscript.

The author has done all the numerical work in the publications I, III, IV and V, and part of it in II using the density functional theory codes Dacapo and GPAW. She has written the first drafts of I, III, IV and V and participated actively in the writing of II. Furthermore, the author has contributed to the paper J. S. Hummelshøj *et al.*, *DFT based screening of ternary alkali-transition metal borohydrides - a computational materials design project* J. Chem. Phys. **131**, 014101 (2009), which is excluded from the thesis.

Contents

Abbreviations

ANEB	adaptive nudged elastic band
ASE	Atomic Simulation Environment
BEP	Brønsted-Evans-Polanyi (relation)
BFGS	Broyden-Fletcher-Goldfarb-Shanno (numerical optimization scheme)
CINEB	climbing image nudged elastic band
DCE	dichloroethene
DFT	density functional theory
DOS	density of states
ELF	electron localization function
GGA	generalized gradient expansion approximation
GPAW	grid projector augmented wave
HDC	hydrodechlorination
HK	the Hohenberg-Kohn theorem
IUPAC	International Union of Pure and Applied Chemistry
KS	Kohn-Sham
KSDFT	Kohn-Sham density functional theory
LDA	local density approximation
LDOS	local density of states
MAE	mean absolute error
MD	molecular dynamics
MEP	minimum energy path
ML	monolayer
NEB	nudged elastic band
PAW	projector augmented wave
PBE	Perdew-Burke-Ernzerhof (energy functional)
PES	potential energy surface
RLS	rate limiting step
RPBE	a revised Perdew-Burke-Ernzerhof (energy functional)
TCE	trichloroethene
TS	transition state
TST	transition state theory
PCE	perchloroethene
VC	vinyl chloride
XC	exchange correlation

1 Introduction

1.1 About chemistry on metal surfaces

My first encounter with the concept of catalysis dates back to the late 1980's. While traveling in my aunt's car, I was told that the unpleasant smell filling the cabin originated from a device called a catalytic converter. Later on I learned that this device is in fact very important in modern days, as it makes the poisonous by-products of gasoline combustion less harmful. The automobile "cat" provides an excellent, everyday example of a phenomenon called heterogeneous catalysis. Catalysis in general refers to a process where the rate of a chemical reaction increases due to a substance called catalyst, which lowers the energy input needed to trigger the reaction. The process is called heterogeneous, if the reactants and the catalytic material are in different phases. In the automobile catalytic converter, the reactants including hydrocarbons, carbon monoxide, and nitrogen oxides, come from the *gas* stream exiting the combustion engine, whereas the catalytic material, finely dispersed platinum group metal on a substrate, is in a *solid* phase. The unsaturated surface metal atoms bind the impinging molecules providing them first of all a ground to interact. Moreover, adsorption on the metal surface loosens, and in some cases directly breaks the existing bonds in the molecules, thereby speeding up the reaction. The product molecules desorb from the surface back to the gas phase freeing sites for the new reactants. Returning to our example, in one of the reactions catalyzed by the converter in a car, an O_2 molecule dissociates upon adsorption forming two oxygen atoms. Oxygen then reacts with adsorbed CO forming CO_2, which leaves the metal surface.

The impact of heterogeneous catalysis to modern society is far from being restricted only to pollution control. The principles are applied in the industrial scale production of innumerable chemical compounds including fuels, fertilizers, and fine chemicals. Thus, it is not surprising that the area has attracted lots of attention in the form of Nobel prizes, the latest one being granted for German physicist, Gerhard Ertl in 2007 (see his Nobel Lecture, Ref. [1]). The huge potential of heterogeneous catalysis, realized already in many ways, has been an important motivation and boost for the development of surface science (see *e.g.* Refs. [2, 3]). This research field was long grounded exclusively on the experimental methods, such as scanning probe techniques, electron-, and vibrational spectroscopy. Even though the measurements are sophisticated, their data can sometimes be hard to interpret. This is where the necessity of quantum mechanical modeling of the systems steps into the picture. The data

obtained from the "computer experiments" involving explicit treatment of individual atoms of the studied system, has successfully complemented experimental results, as well as provided independent information. In fact, the intensive interplay between experiment, theory, and computational modeling has reached a point where industrially relevant catalytic reactions can be described from fundamentals [4]. The real progress in computational chemistry has been made during the last two decades along with the growth of computer power and improvements in methods and algorithms. One method stands out as superior to the others when modeling a surface of a catalyst - the Kohn-Sham density functional theory (KSDFT). The power of the theory lies in its simplicity compared to wave function based methods, making it applicable to large quantum mechanical systems. In 1998 the Chemistry Nobel prize was granted for one of the developers of KSDFT, Walter Kohn (see his Nobel lecture in Ref. [5])

1.2 Background for this thesis

The ability of Pd to catalyze reactions involving organic molecules has long been acknowledged. Palladium's moderate propensity toward holding on to molecules allows the reactants to first rearrange into products, then secondly lets them leave the surface. The motivation for the work conducted in this thesis arose from the incompleteness in current understanding of how palladium surface catalyzes the decomposition of ethylene and the hydrodechlorination of trichloroethylene. This study contributes on one hand to the knowledge of the entire field of related reactions by treating prototypes of olefinic (chlorinated) hydrocarbon chemistry over closed packed platinum group metal surfaces. On the other hand these particular reactions are relevant subjects for study already in themselves, as explained in the following discussion concerning the current understanding of the reactions.

1.2.1 Ethylene decomposition over palladium

The ongoing interest toward ethylene interaction with platinum group metals owes to the fact that ethylene is involved in many catalytic reactions proceeding over transition metals, such as polymerization, synthesis of functionalized olefins, and acetylene hydrogenation. Moreover, hydrocarbon interaction with metals is known to produce strongly held carbonaceous residues, "coke", which can affect the catalyst performance. For some reactions the effect might be beneficial and for some detrimental [6]. Some residues, such as ethylidyne (C-CH_3), may also act as spectator species, which do not contribute to the function of the catalyst [7, 8, 9].

Figure 1.1 shows the experimentally derived temperature dependence of ethylene de-

composition over Pd(111) catalyst [10]. Five distinct evolution steps have been identified: below room temperature ethylene adsorbs molecularly onto the surface (1). Spectroscopic measurements [11, 12, 9, 13, 8] and DFT calculations [14, 9, 15, 16] have identified two main chemisorption modes: di-σ-mode, where two metal atoms participate to the bonding, and π-mode, where one metal binds the molecule. If a Pd surface is exposed to ethylene at room temperature, the adsorption results in immediate formation of ethylidyne (2). Upon heating beyond 350 K ethylidyne dehydrogenates to C-CH_x (3), whose exact chemical composition is not known. Further heating leads to complete decomposition to carbon atoms (4) which beyond 440 K start to penetrate into the lattice (5).

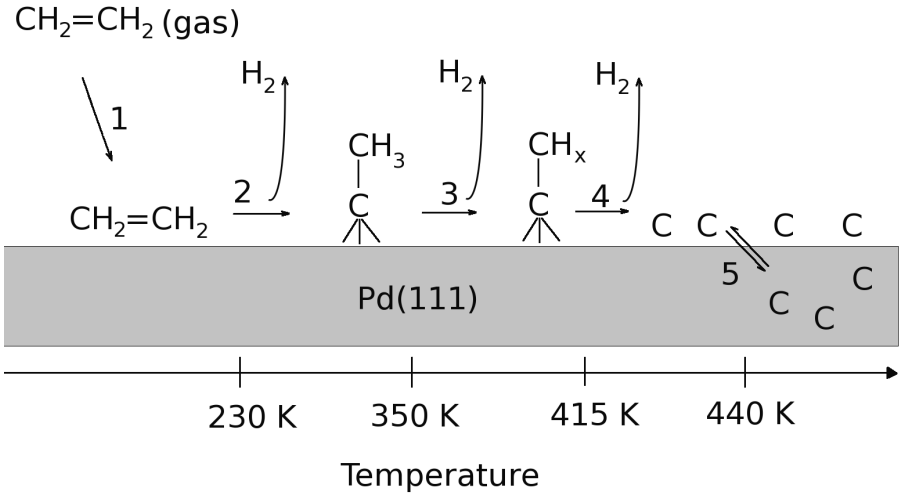

Figure 1.1: Experimentally derived scheme for ethene decomposition over Pd(111) surface as function of temperature. Adapted from the study by Gabasch *et al.* [10]

The ethylene decomposition over Pd is an example of a surface catalysis problem best resolved by combining experimental and computational expertise. The measurements outline the reaction mechanism, but *e.g.* the gap related to the transient ethylene-ethylidyne conversion can only be attained by a theoretical examination. The mechanism for this particular step on Pd has been addressed by DFT studies [14, 17] which show that the reaction most likely proceeds via the formation of vinyl (CH-CH_2) and ethylidene (CH-CH_3) intermediates, and that the ethylene dehydrogenation to vinyl is the rate-determining step. From ethylidyne forwards the C-C framework has been computationally shown to stay intact during the dehydrogenation to C-CH [18]. The investigations conducted in the present thesis consolidate the reaction scheme, and furthermore shed light on the role of ever-present defects, such as step edges, in the metal surface on the reaction mechanism and energetics.

1.2.2 Pd-catalyzed hydrodechlorination of trichloroethene

A chlorinated form of ethylene, trichloroethene (TCE, $Cl_2C{=}CClH$) is synthesized in large quantities for versatile industrial use *e.g.* as a solvent. Poor handling and disposal practices of the compound have contaminated groundwater at numerous sites worldwide. As the exposure to TCE has been linked to severe health effects such as liver damage and cancer [19], there has been an ongoing effort to remove it before it enters the drinking water. Conventional treatment methods, such as activated carbon adsorption, often merely relocate the contaminant from one site to another. With help of catalytic hydrodechlorination (HDC), the compound can be eliminated once and for all:

$$C_2Cl_3H + 4H_2 \rightarrow C_2H_6 + 3HCl \tag{1.1}$$

To date, Pd-catalyzed water phase HDC of TCE has been studied extensively [20, 21, 22, 23, 24, 25], and potential of Pd catalysts for commercial applications has been demonstrated [26]. However, there are still unresolved issues concerning the reaction mechanism and catalyst deactivation.

Regarding the mechanism for TCE HDC over Pd, the scientific community appears to divide into two schools. The absence of chlorinated by-products from TCE HDC has been explained by a *direct* reaction pathway comprised of a removal of multiple chlorines without the formation of partially chlorinated intermediates, dichloroethene (DCE) and highly toxic vinyl chloride (VC) [20, 21, 27]. Another school of scientists supports the *sequential* pathway proceeding through DCE and VC [28, 29]. They explain the non-appearance of lesser chlorinated compounds by their higher reactivity, which is observed when the molecules are introduced onto the surface from either water [24] or gas phase [30]. The TCE $\rightarrow$ DCE conversion would then be the rate-determining process followed by fast reductions to ethene and ethane. Interestingly, the reactivity ordering of chloroethenes does not follow the supposed ease of C-Cl bond breaking: C-Cl bond(s) get stronger the less there are chlorines in the ethene. This has raised speculations that the addition of hydrogen, rather than the cleavage of Cl, would determine the rate of TCE reductive dechlorination. The C-H bond formation would be followed by an instant C-Cl bond breaking and re-establishment of the double bond to prevent the formation of chlorinated ethanes.

Other unresolved questions, closely related to transitioning the Pd-catalyzed HDC into practice, deal with the tendency of the catalyst to deactivate over time. Chloride is a known poison in Pd-based catalysis and is present in natural groundwater as well as released from the reaction [31, 32, 33]. It lowers the TCE conversion dramatically [34], and for VC it has been suggested to change the preferred reaction mechanism from hydrodechlorination to hydrogenation [35]. Thus, it is important to promote the Cl

removal from the surface. HCl discharge may be facilitated by using bases (see Ref. [36] and references therein), but a very promising alternative to enhance the deactivation resistance, is to alloy Pd with another metal. A catalyst composed of Pd decorated Au nanoparticles (NP:s) has been shown to exhibit very good resistance against chloride and sulfide poisoning [37]. Moreover, the activity of TCE HDC greatly improves on Pd supported by Au nanoparticles [38, 39, 37]: the rate constant is over 70 times higher compared to a Pd/Al_2O_3 catalyst [38]. Catalytic activity was discovered to be specifically sensitive to a Pd coverage showing a volcano-shape coverage dependence as depicted in Figure 1.2. While the optimal catalyst was suggested to have 70 % Pd coverage, its exact composition and the contribution of gold to the function of Pd has remained speculative. However, a recent X-ray absorption spectroscopy study provides evidence of mainly 2-dimensional Pd islands surrounding the Au particle [29].

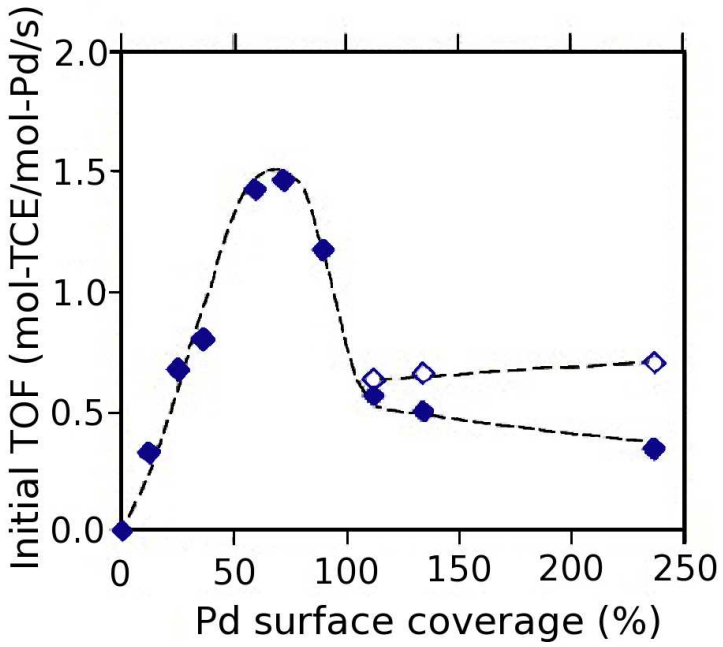

Figure 1.2: Volcano-shaped dependence of initial TCE HDC turnover frequency on the coverage of palladium on gold particle. The open diamonds beyond 100 % coverage correspond to values normalized to exposed Pd atom content. Adapted from Ref. [39].

Our work aims at shedding light on the unresolved issues of TCE HDC reaction mechanism and the structure and function of Pd/Au bimetal catalyst.

2 Theoretical aspects of reactivity in heterogeneous catalysis

The rational design of more efficient catalysts for the future calls for recognizing the active sites and key intermediates for the reaction. Using computational methods, these can be identified through systematic scanning of possible reaction sites and relative stabilities of the species presumably involved in the reaction. These are directly related to the ability of the catalyst surface to bind molecules and break and/or form bonds. The binding strength of the intermediates ($\leftrightarrow$ adsorption energies) often correlate with the facility of the corresponding elementary reaction ($\leftrightarrow$ activation energy), which is why the reactivity of the catalytic material can be often described by the concepts of adsorption. These types of relations are most useful since they simplify the theoretical problems and thereby reduce the computational cost when screening the potential catalysts.

The following discussion has been divided to address first the physics and chemistry of adsorption; second, the relevant concepts related to molecule activation; third, the ways to link the energetics of these processes together; and finally, the boundary conditions for a catalyst to maximize the reaction rate.

2.1 Adsorbate-surface interactions and the d-band model

Within this thesis the reactions are considered to be of Langmuir-Hinshelwood type, *i.e.* all the reactants are first adsorbed on the surface where they vibrate and bonds are broken/formed. Thus, the primary step of all the studied reactions is the adsorption of the reactants from gas or liquid phase onto the surface of condensed material. According to the degree of perturbation in the atom's/molecule's electronic structure upon adsorption, the process can be roughly classified to be either physi- or chemisorptive. An atom/molecule is considered chemisorbed if there is a formation of covalent bonding between the adsorbate and the surface, whereas physisorption is characterized by weak Van der Waals -type of interaction.

The energy change related to the adsorption is called adsorption energy (E_{ads}). Through-

out the thesis, the quantity is given as

$$E_{ads}(A) = E(SA) - E(S) - E(A), \tag{2.1}$$

where E(SA) is the energy of the surface with the adsorbate, E(S) is the energy of the surface, and E(A) is the energy of the isolated adsorbate. Note, that the adsorption energy corresponding to an exothermic adsorption process has a negative sign. A term binding energy is used as an opposite of the adsorption energy value.

2.1.1 The d-band model of adsorption

Let us take a look at the simple qualitative scheme of the chemisorption process with the aim to get a grasp on the essentials of this physico-chemical phenomenon. The discussion follows the theoretical work of Hammer and Nørskov, who formulated the d-band model of adsorption [40] to explain the binding and activity trends on a variety of metal surfaces.

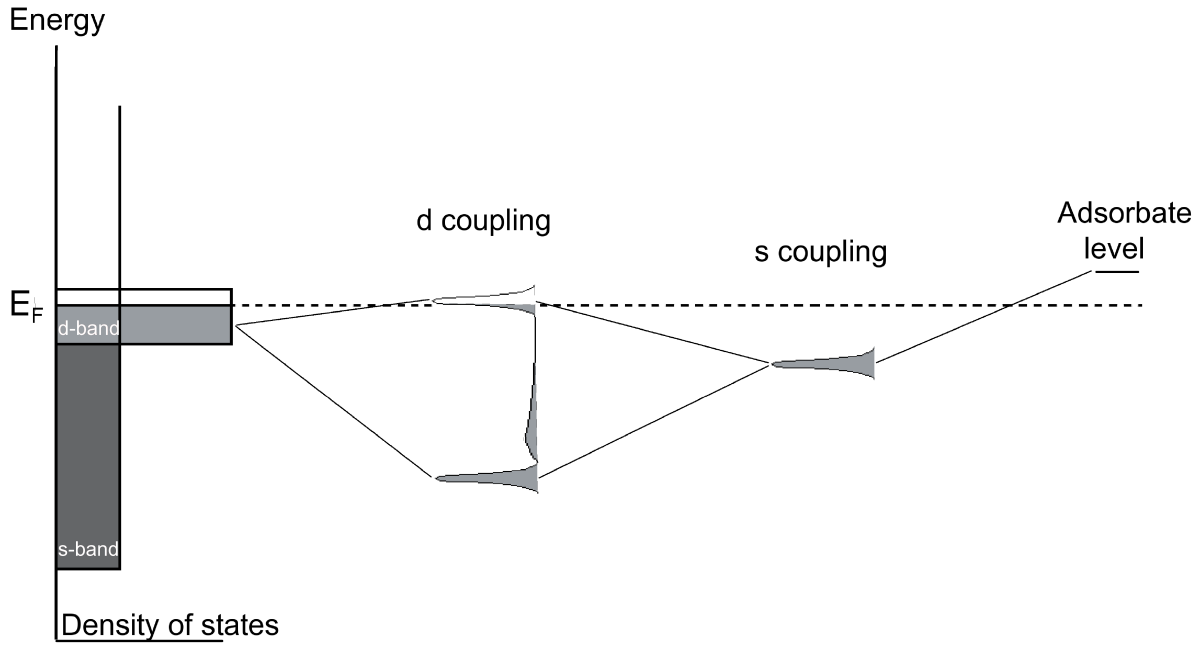

Figure 2.1: Schematics of the chemisorption bond formation between the adsorbate and a transition metal surface.

When an atom/molecule from gas phase approaches the surface of a metal, its states start to interact with the valence states of the surface atoms. The valence states form bands of different widths; the s-band is a broad one while much narrower band is

formed by the d-states. Coupling to the broad s-band leads to chemisorption, where the adsorbate level merely broadens and shifts down in energy. The narrower the metal band, the stronger the interaction between the states, and the more the situation resembles a simple two-state problem; Coupling to the narrow d-band gives rise to the formation of bonding and antibonding states. Figure 2.1 illustrates the mixing of an atom and metal orbitals as a two-step process. First, the sharp adsorbate state is coupled to the metal s-states resulting in a single resonance well below the Fermi-level. Next the formed hybrid states interact with the metal d-band giving rise to two levels, the lower bonding, and the higher antibonding with respect to the adsorption.

One of the assumptions made in the d-band model is that the coupling to the broad s-band is independent of the transition metal, and the contribution from the d-electrons determines the variations in binding strengths. In the d-coupling step the bonding state is populated while the occupation of the anti-bonding state depends on the position of the metal d-band relative to the Fermi energy. If the d-band starts to rise above the Fermi level, the resulting antibonding state ends up above the Fermi-level and becomes unoccupied. This means that a high-lying d-band is associated with stronger binding.

2.1.2 Factors governing the interaction strength

Let us next take a look at the effects that determine the shape and position of the d-band. As explained above, the d-band is closely related with the ability of the metal to bind adsorbates and is thereby linked to the reactivity of the surface. Often even the simplest d-band descriptor, the center of gravity of the d-band (ϵ_d)), has been shown to correlate well with the reactivity parameters for various systems (see Ref. [41] and references therein).

Varying the element

Moving from left to right across the transition metals in the periodic table, the ϵ_d decreases. Coupling this trend to the position of the antibonding state accounts for the better binding ability of early transition metals compared to noble metals. Chemisorption gets weaker also when moving down within a group. This is explained by the higher orthogonalization energy cost for more extended d-orbitals.

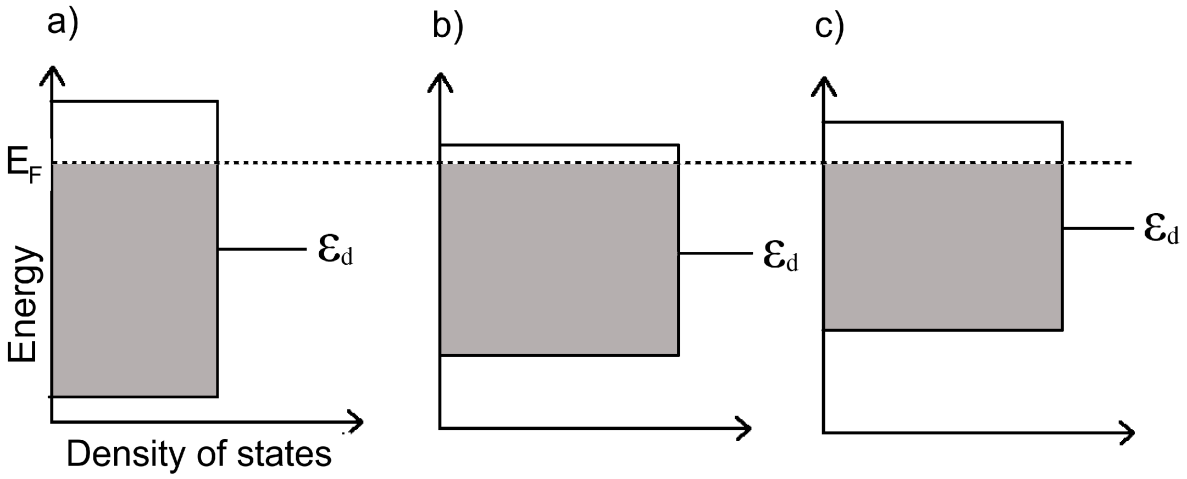

Figure 2.2: Schematic illustration of the effect of tensile strain or reduced coordination on the d-band of a late transition metal. a) d-band is more than half-filled; b) exposure to the strain of reduced coordination results in decreasing band-width; c) d-band shifts up to maintain the number of d-electrons.

Straining and coordination

The d-band of the metal surface can be modified without varying the element. This is done by introducing a strain to the lattice, or by changing the coordination of the metal atoms. These effects have been shown to alter the electronic and catalytic properties of transition metal surfaces [42, 43, 44, 45, 46, 47]. A tensile straining is obtained for example by growing a metal pseudomorphically on a substrate that has a larger lattice constant. This results in narrowing of the d-band due to the reduced overlap of the states. Band narrowing occurs also when the metal atoms become less coordinated, i.e. have fewer nearest neighbors. Low-coordinated sites, such as steps, kinks, and metal particle corners, are always present in the working catalysts, and even the crystals used in the surface science experiments are never entirely perfect. If the active metal is a late-transition metal, the band narrowing leads to the up-shift of the d-band. The reasoning for this is illustrated in figure 2.2, which shows the schematics of a d-band of a late transition metal subjected to a tensile strain or a reduction in the atom coordination. When the bandwidth decreases, the only way to preserve the degree of d-band filling and thereby satisfy the charge conservation is to shift the d-band upwards in energy, which leads to stronger interaction with the adsorbates. For an early transition metal the effect is exactly the opposite [48].

Alloying

Yet another method to modify the reactivity of the metal surface is by alloying it with other metal(s) [49, 50, 51]. The catalytic properties of multimetallic nanoparticles or clusters can be tuned by varying the chemical composition, atomic ordering, and size all at the same time. This provides a flexible ground for the search of active and selective materials. Often the nanoalloy exhibits synergistic properties that cannot be identified as an intermediate property of the constituent metals, but rather something beyond. For instance, when a Pd layer is deposited on top of Au(111), the tensile strain and the weak interaction between Pd and Au makes the Pd overlayer more reactive compared to the pure Pd(111) surface [51].

As one can see, the reactivity of the surface can result from a quite complex interplay between various electronic and geometric effects. The complexity calls for a systematic categorization of different factors governing the adsorption strength. The influence of alloying is typically discussed in terms of ensemble and ligand effects [52, 53]. While these concepts are frequently used in the literature, their definitions are not always transparent. In the present thesis the following definitions for the different effects are used.

Ligand effects account for the changes in adsorption strength due to the variations in the elements *surrounding* the fixed adsorption site. The ensemble effect on the other hand is a *direct* effect, related to the variations in the composition of the binding site itself. Let us take an example to make the sorting more clear, and consider an ethene adsorption on palladium-gold alloy. A Pd-Pd bridge represents one possible ensemble to which the adsorbate could bind to. This Pd dimer could be bound only to gold atoms, or it could have other Pd atoms in the neighborhood. These different ligand surroundings affect the electronic structure of the Pd dimer leading to different adsorption strengths for ethene. On the other hand, if the surroundings are kept fixed, and the other Pd in the ensemble is replaced by Au, one would be dealing with the ensemble effect. In practice, the ligand and ensemble effects are often difficult to decouple, and moreover, they are usually accompanied by the strain and coordination effects introduced earlier. Computational methods are well-suited to disentangle these effects and examine them separately.

2.2 Accessing the kinetic parameters

So far we have mainly been considering (meta)stable atomic arrangements of atomic or molecular species adsorbed on the metal surface. Next we will extend our discussion to concern unstable atomic configurations, which need to be crossed in order for a

transition to take place. A transition can be a chemical reaction where a bond forms or breaks or a diffusion of an atom on a catalyst surface.

In principle the transitions could be simulated directly via electronic structure calculations using molecular-dynamics (MD). In this method atoms and molecules are allowed to interact with each other for a period of time to obtain required statistics. The severe drawback in direct simulation for treating many systems of interest is the so-called rare event problem: the transitions occur on time scales much longer than the periods of atomic vibrations. There can easily be 10^{10} vibrational periods between the relevant transition events, meaning that the required MD simulation might take thousands and thousands of years!

2.2.1 (Classical) transition state theory

Fortunately one can access the chemical kinetics also by other techniques. The rate constant, k, which describes how efficiently the reactant is converted into product, can be calculated by treating the studied system with equilibrium statistical mechanics. This is in fact possible because the transitions are so rare - thermodynamic equilibrium can be thought to prevail among reactants for all degrees of freedom between the events of interest. This so-called strong-coupling assumption is the first one of the key presumptions made in the transition state theory (TST). The other basic assumption of the theory has to do with the concept of the transition state (TS). It is often referred as a single configuration of the atomic system, but within the formulation of TST, the transition state should be thought of as "a *set* of states that all reactive trajectories must pass through and which is never encountered by any nonreactive trajectories" [54]. This set of states forms a "dividing surface" separating reactants from products, and in TST it is assumed to represent a "point of no return": once the transition state is reached, the reactants form products. Other approximations of TST are the Born-Oppenheimer treatment of nuclei-electron system (see the beginning of chapter 3.1.1), and the classical treatment of motion - quantum mechanical tunneling effects are neglected.

The powerful discovery made in 1930's by Eyring was that all the quantities needed for the formulation of the TST rate constant are available from the potential energy surface (PES) [55] which is constructed by associating every atomic configuration with the corresponding energy. Figure 2.3 portrays a PES of a fictitious transition. If the system consists of N atoms, the energy surface becomes 3N dimensional, expressing the energetic information for each set of x-, y-, and z-coordinates of N nuclei. In a conventional TST scheme, the (3N-1)-dimensional dividing surface passes through the saddle point of the PES. Note that traditionally the saddle point atomic configuration is referred as a transition state of the system, even though the meaning of TS in the formulation of the TS theory is something different, as explained earlier. This

nomenclature is adopted also in the studies enclosed by the present thesis. The term "activated complex" is also used in this thesis for the saddle point configuration of the atoms.

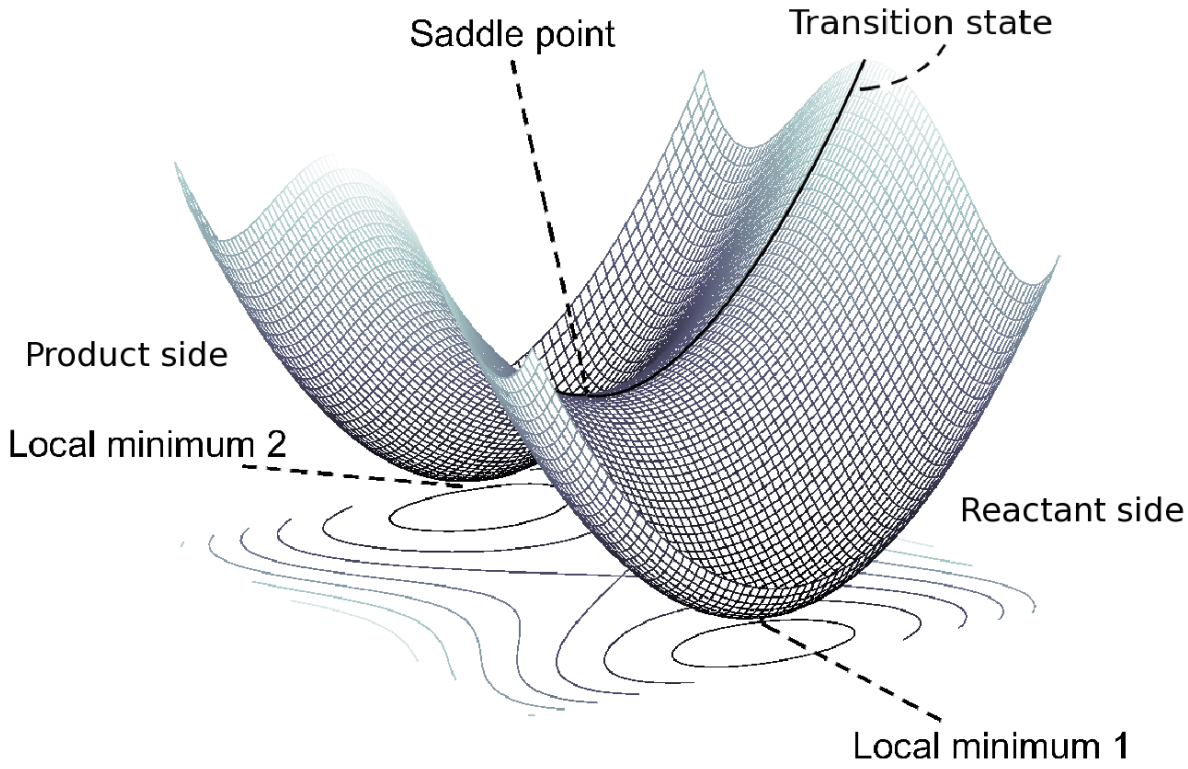

Figure 2.3: Model of a potential energy surface showing two local minima connected by a saddle point. The transition state is the dividing surface (in this case 1-dimensional) between the minima.

Let us next take a look at the cursory derivation of the transition state theory rate constant under the harmonic approximation. For more information, see references [56, 57, 58].

The rate constant for elementary reaction according to the TST is obtained from the product

$$k_{TST} = P_{TS} \cdot r_{TS}, \tag{2.2}$$

where P_{TS} is the probability of finding the system (initially in the reactant region R) in the infinitesimal TS region, and r_{TS} is the rate of crossing the TS from reactant side to the products.

Since the reactant is assumed to have reached equilibrium conditions, the probability

factor can be calculated using a ratio of the partition functions over TS (dividing surface with an infinitesimal width) and reactant region R. For the same reason the velocity can be evaluated from the Boltzmann distribution, and equation 2.2 can be written

$$k_{TST} = \frac{Z^{TS}}{Z^{R}} \cdot \sqrt{\frac{k_B T}{2\pi\mu}} = \frac{\int_{TS} e^{-V(\mathbf{r_1},...,\mathbf{r_N})/k_B T} d\mathbf{r_1}...d\mathbf{r_N}}{\int_{R} e^{-V(\mathbf{r_1},...,\mathbf{r_N})/k_B T} d\mathbf{r_1}...d\mathbf{r_N}} \cdot \sqrt{\frac{k_B T}{2\pi\mu}}, \tag{2.3}$$

where V is the potential energy, k_B is the Boltzmann constant, T the temperature, $\mathbf{r_1}, ..., \mathbf{r_N}$ the atomic positions, and μ is an effective mass of the system in motion across the transition state.

The harmonic approximation for TST rate constant applies well to systems such as molecules on the solid surface, where atoms vibrate around stationary points. Since the statistical weight is greatest at the minimum of the reactant region (V_{min}), and at the saddle point of the TS region (V_{SP}), it is best to carry out the harmonic expansion of the potential energy about these points. Once this is done, one can plug these functions into the configuration integrals in equation 2.3, and the harmonic TST rate constant can be written

$$k_{HTST} = \frac{\prod_i^{3N} \nu_{min,i}}{\prod_i^{3N-1} \nu_{SP,i}} e^{-(V_{SP}-V_{min})/k_B T}, \tag{2.4}$$

where ν_i are the positive normal mode frequencies. The quantity

$$V_{SP} - V_{min} := E_{act} \tag{2.5}$$

is referred to as the activation energy throughout the thesis. In terms of (Gibbs) free energy of activation ($\Delta G^{\ddagger}$), the TST rate coefficient can be recasted as [56]

$$k_{HTST} = \frac{k_B T}{h} e^{-\Delta G^{\ddagger}/k_B T} = \frac{k_B T}{h} e^{\Delta S^{\ddagger}/k_B} e^{-\Delta H^{\ddagger}/k_B T}, \tag{2.6}$$

where h is the Planck constant, $\Delta S^{\ddagger}$ refers to entropy of activation, and the enthalpy of activation $\Delta H^{\ddagger} \approx E_{act}$. Note that we arrived to Equation 2.4 by classical considerations. The harmonic TST rate coefficient can be tuned into a more accurate version by replacing the partition functions by their quantum mechanical counterparts, and by treating also zero-point vibrations and tunneling effects.

The harmonic TST approximation has the same form with the empirically observed behavior of rate coefficient

$$k = Ae^{-E/k_BT}, \tag{2.7}$$

which was introduced already in 1880's by S. Arrhenius and J.H. van't Hoff. The prefactor A having a unit $1/s$ is related to vibrational entropy (compare to Eqs. 2.4 and 2.6 for motive), and is called the frequency factor or attempt frequency of the reaction. The rate constant is thus often interpreted as a total number of reaction attempts per second multiplied by a Boltzmann probability factor corresponding to the energy barrier for the reaction. (Note that conventionally the activation energy of the reaction is identified as E from fitting experimental data to equation 2.7, and following the International Union of Pure and Applied Chemistry (IUPAC) guidelines, the potential energy gap between the reactants and the transition state should rather be called the threshold energy.)

2.2.2 Comparing the measured and calculated energies of activation

Arrhenius expressions are valid solely for elementary reactions. This raises a question: how can one relate the experimentally obtained, *apparent* activation energy, E_{act}^{app}, of a composite reaction (including e.g. adsorption of the reactants and the bond activations on the surface) to the features of PES?

Basically the apparent activation energy can be considered to consist of three contributions: i) the activation energy E_{act} corresponding the rate limiting step (RLS) for the reaction (sometimes referred to as a *real* or *intrinsic* activation energy as distinct from the E_{act}^{app}), ii) formation energy of the reactants that participate to the RLS (the liberated heat is used to overcome the intrinsic barrier), and iii) desorption energy of the reaction intermediates on the surface multiplied by the number of sites used for the RLS. This represents the cost needed for freeing the adsorption sites.

The third contribution means essentially that the apparent activation energy is not a constant, but depends on the surface coverage, which in turn is governed by the pressure and the temperature of the gas. To piece together the analytic expression for the E_{act}^{app}, one needs a kinetic model describing the reaction of interest. As a simple illustrative example, consider a dissociative adsorption

$$AB + * \rightleftharpoons AB* \tag{2.8}$$

$$AB* + * \rightleftharpoons A* + B*, \tag{2.9}$$

where * denotes a surface site. According to the kinetic model introduced in Ref. [59], the apparent activation energy for this reaction can be written

$$E_{act}^{app} = E_{act}(diss) + \Delta E_{ads} - 2\Delta E_{ads}\theta_{AB}, \tag{2.10}$$

where $E_{act}(diss)$ is the real activation barrier for dissociating the bond, ΔE_{ads} is the adsorption energy of the AB, and θ_{AB} is the coverage of the reactant on the surface. The equation 2.10 can be rationalized as follows: For a relatively empty surface (low pressure or high temperature, $\theta_{AB} \approx 0$), the apparent activation energy is an amount $|\Delta E_{ads}|$ lower than the real activation energy of the dissociation because the released energy can be used to overcome the barrier (assuming exothermic adsorption). For high coverages (high pressure of low temperature, $\theta_{AB} \approx 1$) the apparent activation energy is obtained by adding $|\Delta E_{ads}|$ to the intrinsic barrier. This is because there are no available sites for dissociation, and it costs $|\Delta E_{ads}|$ to free a site from the surface.

2.3 Linear energy relations and reactivity optimization

Since the determining of the activation energies is far from being a simple task, correlations have been developed to map the reactivity information to easily accessible descriptors, such as the binding energies of atoms.

The widely used family of relations links the reaction activation energy and the binding strength of reaction intermediates (ΔE) together. These Brønsted-Evans-Polanyi (BEP) relations in chemistry date back to the first half of the twentieth century [60, 61], but it is not until recently, by utilizing systematic DFT calculations, that BEP dependence has been shown to apply also to heterogeneous catalysis. As an example, dissociations of diatomic molecules over various transition metals establish phenomenal universality in the BEP behavior [62, 63], see Figure 4.16.

The linear correlation between the transition state energy and the intermediate state or reaction energy arises from the fact that the activated molecule has properties of the reactants ($\leftrightarrow$ early TS) and/or the products ($\leftrightarrow$ late TS). Variations in the intermediate states will thus be reflected in the transition state. The universality for a certain type of reaction, for example a bond dissociation on a fcc(111) surface, is explained by the independence of the transition state structure of the atoms present. However, the BEP line for instance in the case of N_2 dissociation on a number of

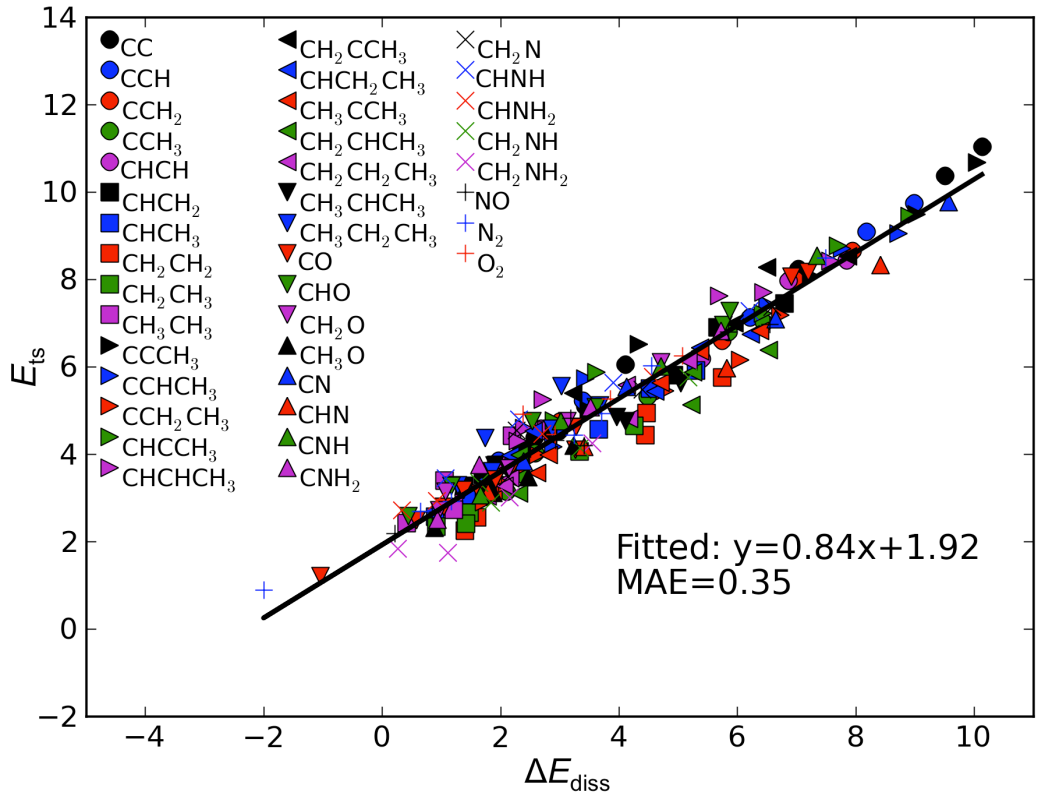

Figure 2.4: Brønsted-Evans-Polanyi relationship between the transition state energies and final state energies for bond dissociation reactions on various stepped transition metal surfaces. Each data point is associated with the corresponding reactant undergoing the C-C, C-O, C-N, N-O, N-N, or O-O dissociation. The MAE stands for the mean absolute error. The Figure is taken from Ref. [63].

different metals is seen to shift downwards when moving from close-packed facets to more open surfaces, such as the ones containing steps [64]. The discrepancy in this case arises at least partly from the geometric effect: the stabilization offered by the low-coordinated step sites is more pronounced for the transition state, because on the step the activated molecule is bound to five atoms whereas on the terrace four atoms contribute to the stabilization of the activated species [65].

Another linear correlation relates the adsorption energy of molecule on a given surface to the adsorption energy of the atom via which the molecule is adsorbed on the same surface. [66, 67, 68] Combined with the BEP relation, this scaling scheme provides a tool for constructing a potential energy surface for reactions from easily accessible quantities, namely the binding energies of the atoms. This has been done, for example, to model ethanol decomposition energetics on several transition metals [69].

The most catalytically active surface is not the one that holds on to the molecules the strongest and lowers the activation barriers the most. For sure it cannot be the

most inert one either. The surface giving the maximum activity for a desired reaction provides an optimal trade-off between the ability to bind reactants/reaction intermediates and break/form bonds, and the inertness for allowing the products to desorb from the surface. The proper degree of inertness also assures that the surface stays clean from fragments poisoning the active sites. However, the strongly adsorbed atoms/molecules on the surface do not necessarily inhibit the catalytic turnover if they are mobile enough in order to "step aside" and free sites for new reactants. The mobility can be a consequence of the adsorbate induced restructuring of the metal surface [70].

The above described trade-off, referred to as Principle of Sabatier, is manifested in the volcano-shaped curves, which result if the activity of catalyst for a certain reaction is plotted against a parameter describing the ability of the catalyst to bind molecules. The volcano plots offer useful guidelines in the search of active catalysts. Combined with the universality of the BEP line for a class of reactions, it turns out that the optimal catalysts are the same for reactions belonging to the same class [71], and the adsorption energies turn into a criterion in the search of the most active catalyst.

3 Computational methods

All the results presented in this thesis have been obtained from calculations performed by codes based on density functional theory (DFT). DFT describes the electronic states of materials in terms of the 3-dim. electron density. This is a great simplification to the wave function theory treatment, which involves a $3N$-dim. antisymmetric wave function of a system with N electrons.

In this chapter an overview of the density functional theory applied in the form introduced by Kohn and Sham, and its implementations used in the calculations of this thesis, is given. For a detailed derivations and discussion concerning the KSDFT, see *e.g* Refs. [72, 73, 74, 75]

3.1 Density functional theory

3.1.1 The electronic many-body problem

Underlying most formulations of the theories treating molecules and solids is the Born-Oppenheimer approximation which rests on the fact that the masses of the nuclei are large compared to the masses of electrons [72]. Consequently, the nuclei move substantially slower than the electrons, allowing the latter to be considered to remain in their ground state configuration. The many-electron system can then be treated separately from the nuclear framework and the problem to be addressed is finding the ground-state energy of the electronic system in external potential set by the nuclei. This can be done by solving the lowest eigenvalue of equation

$$\hat{H}\Psi = E\Psi, \tag{3.1}$$

where $\hat{H}$ is the Hamiltonian operator, Ψ is the many-body wave function with all the electron coordinates as variables, and E the total energy of the system.

Applying atomic units ($e = a_0 = m_e = \hbar = 1$) the Hamiltonian for a system of N electrons is

$$\hat{H} = -\frac{1}{2}\sum_{i=1}^{N}\nabla_i^2 + \sum_{i=1}^{N}V_{ext}(\mathbf{r}_i) + \sum_{i=1}^{N}\sum_{j>i}^{N}\frac{1}{|\mathbf{r}_i - \mathbf{r}_j|}, \tag{3.2}$$

where the first term represents the kinetic energy of the electrons (T), the second term stands for the interactions with the external charges (V_{ext}), and the last term incorporates the repulsion energy between the electrons (W).

The systems having practical relevance may consist of 10^{23} electrons and solution to the eigenvalue problem 3.1 for Hamiltonian 3.2 turns out to be beyond reach. Fortunately, one does not need the 3N-dimensional antisymmetric wave function $\Psi(\mathbf{r}_1, \mathbf{r}_2, ..., \mathbf{r}_N)$ to calculate the energy. It is possible to get along in terms of the three-dimensional electronic density

$$n(\mathbf{r}) = \int |\Psi(\mathbf{r}, \mathbf{r}_2, ..., \mathbf{r}_N)|^2 d\mathbf{r}_2 ... d\mathbf{r}_N. \tag{3.3}$$

3.1.2 The Hohenberg-Kohn theorems

In the formulation of the density functional theory the use of the particle density as a basic quantity determining properties of the many-particle system was put on a firm theoretical basis. This was done in 1964 by Hohenberg and Kohn [76] who derived and proved the theorems that lie in the heart of DFT. The first of the HK theorems states that there exists an invertible mapping between the set of potentials and the set of ground state densities. Since the V_{ext} and thereby the Hamiltonian is uniquely determined by the ground state electron density (except for an irrelevant constant shift), the expectation values of all the ground state observables are obtained from knowing the ground state density. Particularly the total energy can be written as

$$E[n] = T[n] + W[n] + V_{ext}[n]. \tag{3.4}$$

The expectation value of $\hat{T} + \hat{W}$ defines the so called Hohenberg-Kohn functional $F_{HK}[n] = T[n] + W[n]$ which is independent of the external potential and is therefore the same for all Coulomb systems. The second HK theorem states that the ground state density minimizes the functional $E[n] = F_{HK} + V_{ext}[n] = F_{HK} + \int d\mathbf{r} V_{ext}(\mathbf{r}) n(\mathbf{r})$, and the minimum is obtained when the condition

$$\frac{\delta F_{HK}[n]}{\delta n(\mathbf{r})} + \frac{\delta V_{ext}[n]}{\delta n(\mathbf{r})} = 0, \tag{3.5}$$

or equivalently

$$\frac{\delta F_{HK}}{\delta n(\mathbf{r})} = -V_{ext}(\mathbf{r}) \tag{3.6}$$

is fulfilled.

3.1.3 The Kohn-Sham construction

The HK theorems as such do not offer any practical scheme for calculations. Kohn and Sham [77] resolved the problem by constructing a fictional non-interacting system, for which the HK theorems can be applied, since they do not involve any special properties of the particle-particle interaction. The idea is that the density of the real system with interacting particles could be reproduced in a non-interacting system experiencing some external potential. When this density is obtained, it can be plugged into the energy functional to obtain the ground state energy as stated by the first HK theorem.

The Kohn-Sham (KS) system is described by Hamiltonian

$$\hat{H}_s = \hat{T}_s + \hat{V}_s[n], \tag{3.7}$$

where $\hat{T}_s$ corresponds the kinetic energy of the non-interacting particles, and $\hat{V}_s$ is the external potential.

The ground state wave function $\Psi_s[n]$, that can be written as a Slater determinant of the single particle states ϕ_i (KS orbitals), satisfies

$$\hat{H}_s\Psi_s[n] = E_s\Psi_s[n]. \tag{3.8}$$

It can be shown that the energy E_s is a sum of the eigenvalues ϵ_i of the single particle Schrödinger equation, which for a spin-compensated system is

$$(-\frac{1}{2}\nabla^2 + V_s[n](\mathbf{r}))\phi_i(\mathbf{r}) = \epsilon_i\phi_i(\mathbf{r}) \tag{3.9}$$

density being given by

$$n(\mathbf{r}) = 2\sum_{i=1}^{N} |\phi_i(\mathbf{r})|^2. \tag{3.10}$$

The task now is to find the potential V_s, in which the single particle system reproduces the density of the interacting system. Kohn and Sham rewrote the universal functional with the help of the non-interacting system as

$$F_{HK}[n] = T_s[n] + V_H[n] + E_{xc}[n], \tag{3.11}$$

where V_H is the classical Coulombic interaction energy, and $E_{xc}[n]$ is the exchange-correlation functional including all the many-body effects excluded from T_s and V_H.

Applying the second HK theorem (substituting the equation 3.11 to the equation 3.6) one gets

$$\frac{\delta T_s[n]}{\delta n(\mathbf{r})} + \frac{\delta V_H[n]}{\delta n(\mathbf{r})} + \frac{\delta E_{xc}[n]}{\delta n(\mathbf{r})} = -V_{ext}(\mathbf{r}). \tag{3.12}$$

The functional derivatives can readily be calculated for the known functionals $V_H[n]$ and $T_s[n]$, while approximations for the unknown exchange-correlation part must be found. The connection to the sought-after single particle potential $V_s(\mathbf{r})$ of the KS system is obtained from the kinetic energy derivative which can be shown to be

$$\frac{\delta T_s[n]}{\delta n(\mathbf{r})} = -V_s(\mathbf{r}). \tag{3.13}$$

Denoting the derivatives of the classical Coulomb energy and the exchange-correlation energy as $V_H[n](\mathbf{r})$ and $V_{xc}[n](\mathbf{r})$ and combining Eqs. 3.12 and 3.13 one can express the searched potential as

$$V_s[n](\mathbf{r}) = V_{ext}[n](\mathbf{r}) + V_H[n](\mathbf{r}) + V_{xc}[n](\mathbf{r}). \tag{3.14}$$

Using this expression in the KS equations given in 3.9 and 3.10 leads to a determining equations for the ground state density.

Since the KS equations are coupled and highly non-linear, they need to be solved numerically. In practice, one starts by generating an initial density, which is used to construct the $V_s[n]$. The equations 3.9 are then solved with this potential, and new

guess for the density is calculated from the obtained eigenstates via equation 3.10. The procedure is repeated to self-consistency, i.e. until the density does not change in the iteration. Finally the density is inserted into the energy functional that yields the total energy of the system. The remaining task is to find good approximations for the exchange-correlation energy and -potential.

3.1.4 Exchange and correlation energy

The exchange-correlation (XC) energy is the Coulomb interaction between each electron and an exchange-correlation hole (missing charge density) surrounding it. The hole is created by self-interaction correction, that is a classical effect forbidding the electron from interacting with itself, the Pauli exclusion principle, and Coulomb repulsion. The first two effects account for the exchange energy, E_x, which is present even for non-interacting system, and the last effect is responsible for the correlation part, E_c [74]. The parts are usually treated separately, and the total XC-energy is obtained from the sum $E_{xc} = E_x + E_c$.

Several different type of functionals have been developed to incorporate the XC effects. The quality of the descriptions has a strong influence on the accuracy of the calculations, since the exchange-correlation is the only part that is approximated in the Kohn-Sham DFT. A typical strategy for constructing a functional is to proceed by fulfilling different physical constraints, such as the known properties of the XC-hole.

Local density approximation

Consider an electronic system where the density variations are relatively smooth. If the space is divided into small boxes with volume d$\mathbf{r}$, a box at the coordinate $\mathbf{r}$ can then be approximated to contain homogeneous electron gas of density $n(\mathbf{r})$. Each box contributes to the XC energy by amount that is equal to the XC energy per particle in the box, $\epsilon_{xc}^{hom}(n(\mathbf{r}))$, times the number of electrons in the box, $n(\mathbf{r})d\mathbf{r}$. The total XC energy is the sum over all boxes:

$$E_{xc}^{LDA}[n] = \int d\mathbf{r} n(\mathbf{r}) \epsilon_{xc}^{hom}(n(\mathbf{r})). \tag{3.15}$$

This is called the local-density approximation (LDA) of the XC energy [78]. Owing to the construction of LDA, it is exact for one system - the homogeneous electron gas. Surprisingly, LDA works reasonably well also for systems with strong electron density variations, such as atoms and molecules. The most notable of the LDA deficiencies

is its tendency to overbind. The errors in binding energies can be well over 1 eV (see Ref. [75] for the review of the LDA performance).

Generalized gradient approximation

As one climbs higher in the "ladder of functionals" [79], *i.e.* derives corrections to LDA, the XC description becomes less and less local. The next step from the LDA is to include the local gradients of the density into the picture which leads to XC energy of the form

$$E_{xc}^{GGA}[n] = \int d\mathbf{r} n(\mathbf{r}) \epsilon_{xc}^{GGA}[n(\mathbf{r}), \nabla n(\mathbf{r})]. \tag{3.16}$$

In practice this means carrying out a Taylor expansion of the LDA XC functional relative to density variation. However, at the same time one has to enforce some constraints on the gradient expansion in order to preserve a physically well-behaving XC-hole. This procedure leads to generalized gradient approximation (GGA).

The calculations carried out in the present thesis employ GGA functionals PBE [80] and RPBE [81]. The construction of these functionals follows the same logic, and thus they incorporate the same physics and satisfy the same physical constraints. The only difference is in the mathematical form of the exchange energy [81]. In general, the choice for the proper XC functional depends on the investigated system as well as on which properties of the system one is interested in. Whereas one functional works well for predicting binding energies, however, it might fail to give good approximations for lattice constant. The PBE family of functionals is known to give good estimates for adsorption energies on transition metal surfaces, and are thus a rational choice for the problems dealt within this thesis. The overbinding of PBE and RPBE are reported to be around 0.5 eV and 0.3 eV, respectively [81].

3.2 DFT implementations and numerical schemes

There are various schemes within which to perform the self-consistent solution of the KS equations. Besides the proper XC functional, one has to select a model to describe the surface, the representation of the KS orbitals, and a way to treat the core electrons of the atoms. Some basic aspects related to these topics are covered within this section.

3.2.1 Modeling the catalytic surface

Let us consider a catalyst surface we wish to model. Typically there is some substrate material on top of which the active metal particles are distributed. The metal facets might be very regular, or contain steps and other defects. Moreover there are possibly many different metals present, or there are some non-metallic atoms incorporated into the metal lattice. In any case, the real catalyst surface might subsume a great deal of complexity.

The first step in the modeling of the surface is to choose representative areas of the supposed catalyst structure. Then there are basically two methods to limit the system size treatable by DFT calculations with a bearable cost: a cluster method and a slab method. In the cluster method the interesting part of the surface is treated as an isolated cluster of atoms that has the same symmetry with the bulk surface. The electronic structure of a metal cluster, especially if there are too few atoms, might however differ a great deal compared to the extended metal surface. In the slab representation put to use in the calculations of this thesis the problem is avoided by making use of the periodicity of the crystal.

Even though the periodicity is naturally invoked within the plane of the metal surface, the symmetry breaks in the direction normal to the surface plane. Some calculations schemes, such as the plane-wave approach introduced later, calls for the appliance of periodic boundary conditions in every direction. Thus the unit cell to which these conditions are applied, has to contain vacuum in the vertical direction to minimize the interactions between the successive metal slabs (see Figure 3.1b)). This kind of cell is referred to as a supercell. The size of the supercell in the surface plane defines the adsorbate coverage. Figure 3.1 also illustrates how to model an isolated cluster of atoms (Fig. 3.1a)) and a bulk of a material (Fig. 3.1c)) within a periodic calculations scheme.

3.2.2 Wave function representations

The Kohn-Sham states are commonly expanded into a basis set to express the problem with numerically accessible matrix equations. The basis functions can be localized atomic orbitals, or fully delocalized plane-waves. The discretization of equations can also be done by representing the functions with a real-space grid. In this scheme, the values of the wave functions are given on the points of a three-dimensional grid in real space instead of in terms of a basis set.

Describing the fast varying core wave functions or the core region of the valence wave function is inefficient leading to high computational cost. Therefore the plane-

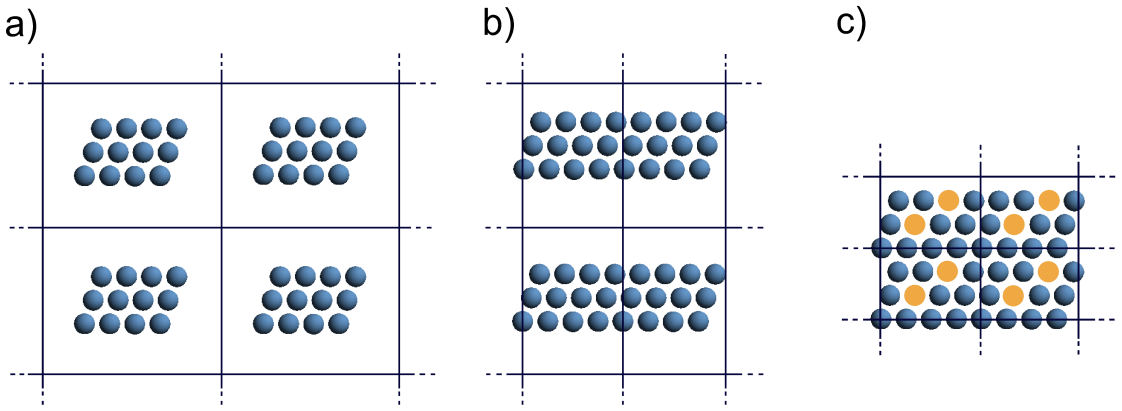

Figure 3.1: Schematic side view of a cell geometry used in a periodic calculation of a) a cluster of atoms, b) a surface modeled by a slab, and c) a bulk of a material with impurity atoms. In each case three replicas of the cell are shown.

wave and real-space representation are frequently used in conjunction with methods in which the core region is described with smoother states. This can be achieved by applying a pseudopotential [72, 82, 83], or projector augmented wave (PAW) [84, 85, 86] formalism.

The very basic ideas of concerning the numerical schemes employed in the present thesis are introduced in the following sections. The discussion is grouped according to how the methods are implemented in the used program packages: The DACAPO [87] code employs plane-waves in conjunction with pseudopotentials, whereas GPAW [88, 89] performs the calculation in a real-space grid using the PAW formalism.

The pseudopotential plane-wave method

Plane-wave basis is a natural choice for expanding the KS single-particle eigenstates when dealing with extended systems with periodicity. Plane-waves are the exact solution of the homogeneous electron gas, and following the Bloch's theorem [90] the periodic potential modifies the eigenfunctions so that one can write the expansion as

$$\phi_{i,\mathbf{k}_n}(\mathbf{r}) = \sum_{\mathbf{G}} c_{\mathbf{G}}^{\mathbf{k}_n} e^{i(\mathbf{k}+\mathbf{G})\mathbf{r}}, \tag{3.17}$$

where the vector $\mathbf{k}$ is a reciprocal vector in the first Brillouin zone, and $\mathbf{G}$ is a reciprocal lattice vector. Solutions corresponding to the same $\mathbf{k}$ are labeled with the band index n. The allowed values for $\mathbf{k}$ form a continuum, and thus the $\mathbf{k}$-space needs to be

discretized for calculations. In this thesis, the Monkhorst-Pack [91] sampling for **k**-points has been used. Also the number of **G** vectors is infinite, but since the coefficients $c_{\mathbf{G}}^{\mathbf{k}_n}$ for the plane-waves with lower kinetic energy are more important, the number of plane-waves used in equation 3.17 can be truncated by introducing a cutoff energy E_{cut}: Only those wave vectors $(\mathbf{k}+\mathbf{G})$ satisfying the condition

$$\frac{1}{2}|\mathbf{k}+\mathbf{G}|^2 \leq E_{cut} \tag{3.18}$$

are taken into account. The required size of a basis set is then simply tested by checking the convergence of the total energy against varying the E_{cut}.

Since expanding the oscillatory core wave functions or the core region of the valence wave function into plane waves is very inefficient, the plane-waves are often used in conjunction with pseudopotentials [72, 82, 83]. The idea is to replace the effective all-electron potential within a radius R_{cut} from the nucleus by a much weaker new potential that has a nodeless ground state wave function (see Figure 3.2). It is required that the new potential produces exactly the same energy eigenvalue as the original all-electron state, and that the pseudo wave function matches the all-electron wave function outside the R_{cut}.

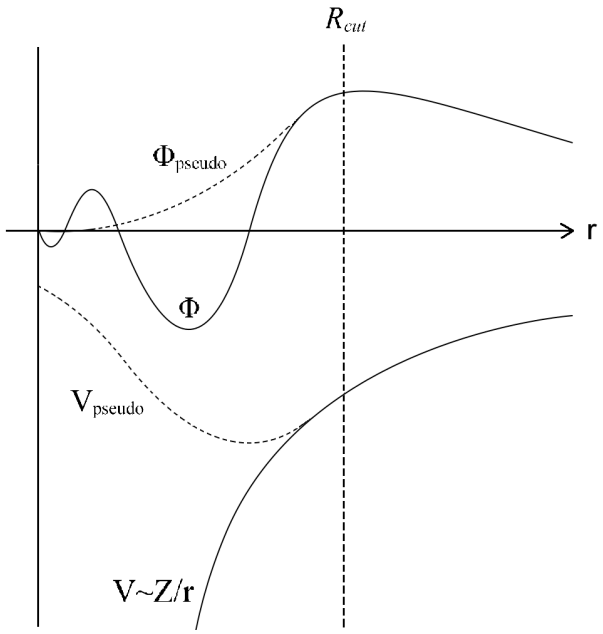

Figure 3.2: Schematic illustration of an all-electron wave function (Φ), pseudo wave function (Φ_{pseudo}), the corresponding Coulomb potential (V), and pseudopotential (V_{pseudo}).

Since the core electron states interact very little with the states of surrounding atoms,

it is justified to construct the pseudopotential for an isolated atom (frozen core approximation). The construction scheme used in the present work was introduced by Vanderbilt [92]. His so-called ultrasoft pseudopotentials are non-norm-conserving meaning that they do not preserve the charge enclosed inside the R_{cut}, but on the other hand they are very smooth, and thus further reduce the number of plane-waves needed.

Grid-based projector augmented wave approach

In a real space grid method the wave functions, densities, and potentials are represented by their values over a set of points in three-dimensional space. The accuracy of the scheme is controlled by the value of grid spacing (typically around 0.2 Å), and the finite difference approximations used for calculating derivatives.

Although the memory needed for representing a wave function with certain accuracy is typically one order of magnitude larger in a real space grid compared to a plane wave basis, there are some aspects by which the grid-based description surpasses the use of plane waves. Whereas the boundary conditions for a plane-wave calculation are necessarily periodic, a real-space method provides an option to employ both free and periodic boundary conditions. However, the size of the unit cell has to be large enough towards vacuum to provide enough space to fit the wave function. Another advantage has to do with the fact that within a grid-based scheme, the parallelization of operations can be conducted efficiently via a simple domain decomposition.

Due to the relatively large memory footprint of the real-space grid representations, it is especially important to describe the core region as "softly" as possible - the smoother the pseudo wave function, the coarser the grid on which it can still be accurately represented. One way to achieve this is to use ultrasoft pseudopotentials, or, as done for example in the GPAW code, the projector augmented wave method (PAW) [84, 85, 86]. The PAW formalism is closely related to the pseudopotentials in a sense, that it was developed by combining ideas from pseudopotential and LAPW (linearized augmented-plane-wave) methods. Unlike the pseudopotential method, the PAW is an all-electron method allowing access to the true wave functions. At the root of the PAW formalism lies a linear transformation, $\hat{\tau}$, which maps the true all-electron KS wave functions $|\Psi_n\rangle$ onto numerically convenient, auxiliary wave functions $|\tilde{\Psi}_n\rangle$ (n labels the band index and k-point of the state):

$$|\Psi_n\rangle = \hat{\tau}|\tilde{\Psi}_n\rangle. \tag{3.19}$$

Now the KS equations are expressed formally as

$$\hat{\tau}^\dagger \hat{H} \hat{\tau} |\tilde{\Psi}_n\rangle = \hat{\tau}^\dagger \hat{\tau} |\tilde{\Psi}_n\rangle \epsilon_n, \tag{3.20}$$

where $\hat{H}$ is the effective one-particle Hamilton operator.

The linear transformation operator modifies the auxiliary wave function in each atomic region yielding a wave function with a correct nodal structure. Thus, the operator has a form "identity plus atomic contributions",

$$\hat{\tau} = 1 + \sum_a \hat{\tau}^a, \tag{3.21}$$

where $\hat{\tau}^a$ accounts for the difference between the true and the auxiliary wave function within a so-called augmentation sphere with a certain cut-off radius around the nucleus a.

As in the pseudopotential scheme, the wave functions of the core electrons are treated separately in a frozen-core approximation, and the valence pseudo wave functions are orthogonal to the core states.

3.3 Probing the stationary points of PES

So far the discussion has revolved around how to obtain a correct electronic structure for a fixed arrangement of nuclei. The rest of the chapter is dedicated on how to find stable arrangements and transition state structures for a given set of atoms. As discussed in the chapter 2.2.1, these correspond to the local minima and first order saddle points in the potential energy surface $E(\mathbf{R})$.

Both DACAPO and GPAW program packages are designed to work together with the Atomic Simulation Environment (ASE) [93] interface, which provides optimization methods used in the present thesis.

3.3.1 Optimizing the atomic structures

The relaxation of a metal lattice or a molecule starts with an educated guess for the nuclei locations $\mathbf{R}$, for which one calculates the electron density and the total energy E($\mathbf{R}$). This total energy represents the potential energy of this atom ensemble, since the system is frozen. The forces acting on the ions I are obtained from the gradient

$$\mathbf{F}_I = -\frac{\partial E(\mathbf{R})}{\partial \mathbf{R}_I}. \tag{3.22}$$

Geometry relaxation algorithms locate the extrema of the PES by minimizing this quantity below some predetermined maximum value. The method used in the present thesis is based on the Quasi-Newton scheme, and more specifically, its BFGS approximation (named after the inventors, C.G. Broyden, R. Fletcher, D. Goldfarb, and D.F. Shanno).

Quasi-Newton method is based on the ideas introduced by Sir Isaac Newton, who proposed an iterative solution for finding extrema for nonlinear functions. In his method one looks at a local quadratic approximation to the function by expanding the first terms of the Taylor series. If the function is quadratic to begin with, one arrives at the extremum in a single step. If not, the extremum of the quadratic approximation function serves as a point for generating a new local approximation and so on. The calculation of the second derivatives (Hessian) is computationally expensive. The Quasi-Newton method provides a way to produce the Hessian more cheaply, using the information from the current iteration by analyzing the gradient vectors. For further details, see for example Ref. [94].

3.3.2 Finding the transition states

There are various different methods for locating the saddle points of PES. Due to the nature of the first order saddle point, these methods usually involve some type of maximization of one degree of freedom and minimization with respect to all the others. The task comes down to tracing the so-called minimum energy path (MEP). The MEP is the path with the greatest statistical weight connecting the initial and final states. At any point along the MEP, the force acting on atoms has a non-zero component only along the path, and the energy is stationary for all the perpendicular degrees of freedom. The maxima on the MEP are saddle points on PES.

An important part of locating the transition state structures is the validation of the supposed saddle point. This is done via vibrational analysis, where the normal modes related to the reaction coordinate are calculated. If one of these is imaginary, the curvature of the PES in the corresponding direction is negative, and the system is at transition state. All the transition states found in the present thesis are verified through vibrational analysis.

The methods used for searching the transition states in the present thesis, the drag method and the nudged elastic band method, are addressed in the following pages.

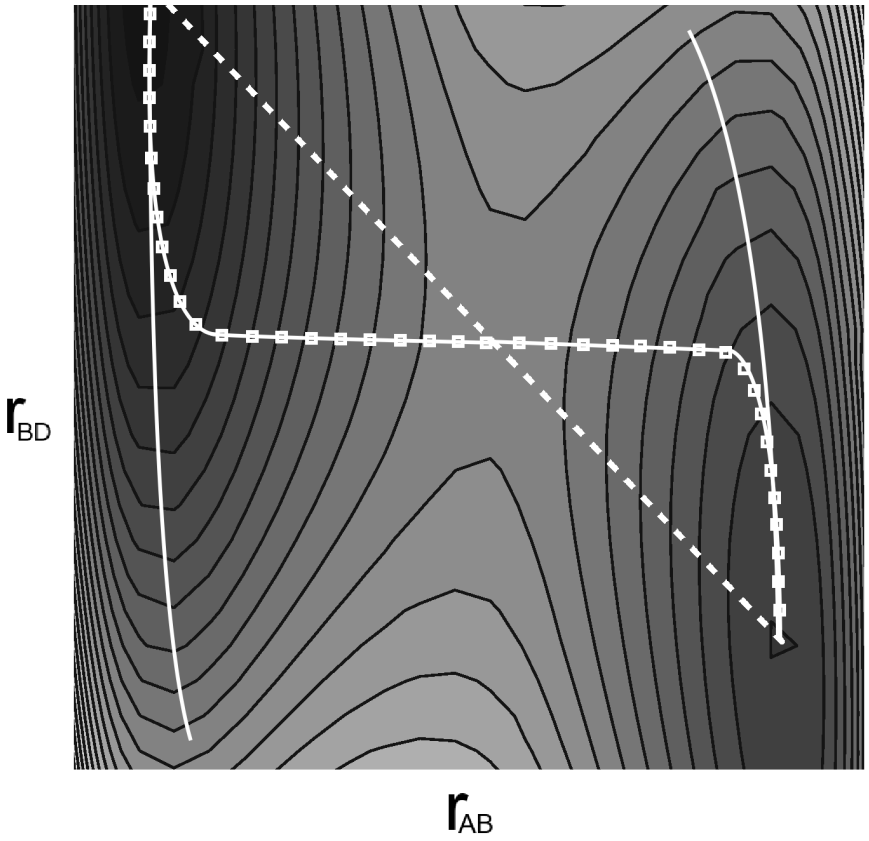

Figure 3.3: A schematic contour plot of the PES, reconstructed using the model potential II from Ref. [95]. The potential is applied to a system, where atoms A, B, C, and D are confined to a line, atom B can form a bond with either one of two fixed atoms A or C, and atom D is coupled in a harmonic way to atom B. The horizontal and vertical axes give the A-B and B-D distances, respectively. The deeper shade of the gray corresponds the lower value of the total energy. Whereas the reaction path found by the drag method (simple solid line) fails to go through the saddle point, the MEP is traced by the NEB method (line with the squares). The dashed line shows the direct interpolation between the end points of the calculations. This can be used as a starting guess for the MEP.

The drag method

The most intuitive and simplest method to solve the problem starts off by choosing an initial configuration corresponding to a local minimum in the PES, and a reaction coordinate, such as a distance between two atoms. Then the system is removed from the equilibrium by "dragging" stepwise along the chosen reaction coordinate. Within every step, the reaction coordinate is kept fixed while the other degrees of system are allowed to relax. At some point the system reaches another local minimum, after which the configuration corresponding the highest energy is tested for the normal modes.

While this so-called drag method works well for several cases, sometimes it fails to bring the system to the saddle point. The failure of the drag method is illustrated in Figure 3.3. The shown PES is reconstructed using the model potential II from Ref. [95]. The relaxed systems with one degree of freedom frozen tend to fall to the valley bottom, *i.e.* along the direction of least curvature starting from the minimum. This is shown with the simple solid lines across the model PES. The saddle point region of the MEP (depicted by the line with squares) exists "sideways" from this valley path, which is why the direction of the reaction coordinate remains at a large angle to the direction of the unstable mode at the saddle point, and the most important region of the MEP is completely missed. Moreover, the traced path is not unambiguous, but depends on whether one starts from the reactant or product state.

The nudged elastic band -method

The nudged elastic band method (NEB) [95, 96, 97] is among the most efficient ways to trace the MEP. It makes use of a two point boundary condition, i.e. the starting point for a NEB calculation is the fixing of the initial and final state configurations. Let us denote the atomic configurations of these states as $\mathbf{R}_0$ and $\mathbf{R}_N$, respectively. Next, N-1 "images" are interpolated between these states giving a set of images $\{\mathbf{R}_0, \mathbf{R}_1, \mathbf{R}_2, ..., \mathbf{R}_N\}$. The images are then coupled via virtual springs with force constant k, and the resulting "band" is strung between the two fixed end points. Minimizing an object function

$$S(\mathbf{R}_1, \mathbf{R}_1, \mathbf{R}_2, ..., \mathbf{R}_{N-1}) = \sum_{i=1}^{N-1} E(\mathbf{R}_i) + \frac{1}{2} k \sum_{i=1}^{N} (\mathbf{R}_i - \mathbf{R}_{i-1})^2. \qquad (3.23)$$

with respect to the intermediate images $\mathbf{R}_1, \mathbf{R}_2, ..., \mathbf{R}_{N-1}$ would then set the elastic band to lie on the MEP. However, there are some problems with this simple approach. Imagine a bumpy 2D landscape with two pits connected by a chain of strings. The force from the landscape gradient would lower the chain to follow the valleys, and the harmonic force would assure, that there are images also in the saddle point region. Now it is easy to picture in mind the difficulties that one might face. In the regions where the MEP is curved, the elastic band tends to cut corners and get pulled off from the minimum energy path due to the spring forces. Also, the images tend to slide down toward the endpoints due to the potential energy gradient, resulting in lowest resolution in the most relevant region *i.e.* near the saddle point.

Both of these problems can be dealt with using a force projection, termed "nudging". The corner-cutting is caused by the component of the spring force perpendicular to the path, whereas the the parallel component of the true force accounts for the down-

sliding. In the NEB method, the force acting on each image only contains the parallel component of the spring force and perpendicular component of the true force. If the local unit tangent to the path at each image is $\hat{\tau}_i$, the NEB force on image i to be minimized is

$$\mathbf{F}_i = -\nabla E(\mathbf{R}_i)|_\perp + \mathbf{F}_i^s \cdot \hat{\tau}_i \hat{\tau}_i, \tag{3.24}$$

where $\mathbf{F}_i^s$ is the spring force, and $\nabla E(\mathbf{R}_i)|_\perp = \nabla E(\mathbf{R}_i) - \nabla E(\mathbf{R}_i) \cdot \hat{\tau}_i \hat{\tau}_i$.

While the "nudging" provides an effective improvement to the plain chain-of-states methods, there might still emerge problems if too few images land in the neighborhood of the saddle point. This could happen for example if the energy barrier is narrow compared to the length of the MEP. A so-called climbing image NEB [98] (CINEB) fixes the problem by making one of the images to climb up along the band to converge on the highest saddle point. This is done by first running a few iterations with regular NEB, and then modifying the force on the image corresponding to the highest energy. The rewritten force makes the image move up the PES along the band, and down in the direction perpendicular to the band. The CINEB method also makes use of variable spring constants to increase the density of images near the top of the energy barrier. Another modification to the NEB method is the so-called adaptive NEB [99] (ANEB), which increases the resolution in the neighborhood of the saddle point. The method starts with only three intermediate images (total five images with the end points included) and lets the NEB calculation converge to some given accuracy. Next, the image corresponding the highest energy is identified, and the two adjacent images are chosen as a starting point for the next calculation. This procedure is repeated until there is an image at the saddle point.

4 Results and discussion

This chapter is divided into three main sections. The first one covers the ethene decomposition on Pd, and the other two deal with the trichloroethene hydrodechlorination. The focal points are in the identification of the reactive sites and the most probable reaction paths based on the energy profiles. Details concerning the computational setups and geometries of the surface species are mostly left out from the discussion, but can be found in the attached articles.

Let us begin by looking at the general picture of the (chlorinated) ethene adsorption on palladium, the starting point of the studied reactions. At low coverage (chlorinated) ethenes adsorb on closed packed Pd in di-σ fashion, illustrated in Figure 4.1. The adsorption mode is characterized by a C-C bond elongation and partial hybridization toward sp^3 character. The planar chloroethene restructures to resemble an eclipsed chlorinated ethane with two sigma bonds made to the metal atoms. In general, the preferred binding mode of (chlorinated) hydrocarbon species is always characterized by the tendency of carbons to satisfy the tetravalency. Figure 4.1 shows also an isosurface of the electron localization function (ELF). The function plots the probability of finding paired electrons in certain part of space, and can therefore be interpreted as an indicator of covalent bonds in the system. It is seen that upon adsorption the ELF reduces between the carbon atoms and appears between the carbon and Pd atoms, consistent with the shift to sp^3 character.

Following the (chlorinated) ethene adsorption, there are several alternative routes for fragmenting the adsorbate to its atomic constituents (as in ethene decomposition) and an even larger amount of ways to replace chlorine atoms with hydrogen (as in trichloroethene hydrodechlorination). This is a direct result from the possibility of bonds to either form or to dissociate at every intermediate stage. The way to trace the most probable reaction route is by carefully examining the kinetic barriers of all possible elementary steps at each stage; then picking the one with the lowest barrier, and choosing this to be along the reaction coordinate. Often the information from earlier studies helps to limit the calculations to address only a certain subset of all possible reaction mechanisms. We acknowledge that our calculations apply only to the low coverage regime since the coadsorbates affect the binding energies and activation barriers [17]. However, when it comes to a qualitative analysis of the most probable reaction pathway, *e.g* identifying the slow and fast reaction steps by comparing the barrier heights, the coverage can be expected to play less integral role.

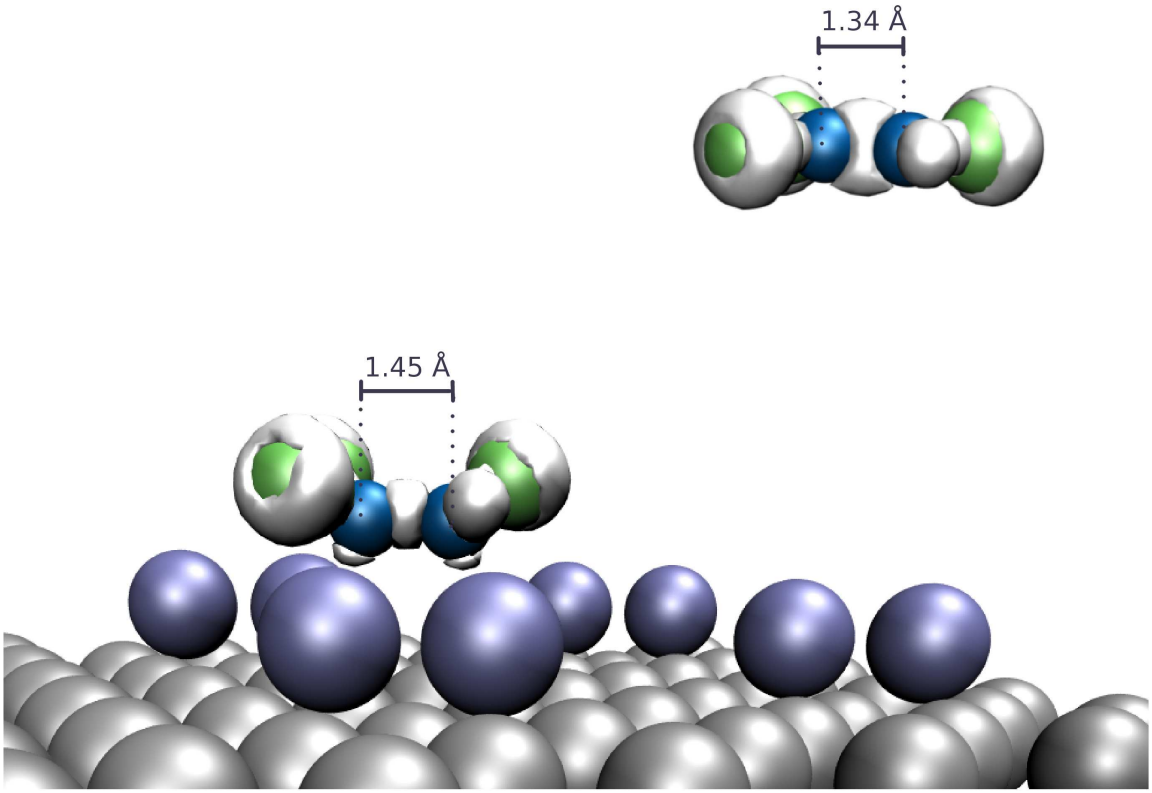

Figure 4.1: Adsorption of TCE (C=blue, Cl=green, H=white) onto Pd (light blue) dimer located on top of Au(111) surface (gray). The upper molecule is not interacting with the surface, and the lower one is chemisorbed onto the surface. An isosurface of the electron localization function (value 0.70) is shown in light gray.

4.1 Ethene decomposition on flat and stepped palladium

First, ethene decomposition to its atomic constituents on closed-packed Pd surfaces is addressed. We did not confine ourselves to study reactions over an ideal Pd(111) interface, but decided to model a typical defect within it, a step. This one-dimensional discontinuity within a Pd(111) terrace was modeled with a Pd(211) surface. Both surface models are built using a supercell of 4 atomic layers, each layer containing 6 atoms. This gives adsorbate coverage of 1/6. Figure 4.2 shows a top view of the unit cells.

The summary of the calculated reaction energetics is given in Table 4.1 and the proposed reaction scheme based on the kinetic barriers is illustrated in Figure 4.3. The following discussion is arranged to follow the reaction coordinate starting from the ethylene-ethylidyne conversion, and proceeding toward the Pd/C phase formation.

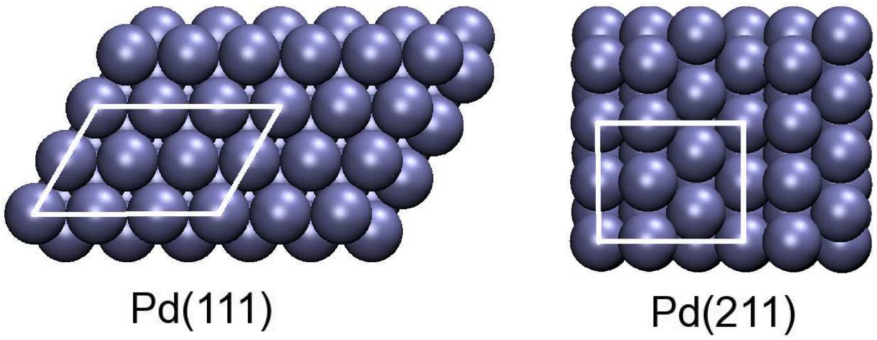

Figure 4.2: Top view of the unit cells (shown as white quadrilateral) used in modeling the Pd(111) and Pd(211) surfaces.

4.1.1 Ethylene-Ethylidyne conversion

Ethylene adsorbs to the adjacent Pd atoms in a di-σ fashion (see Figs. 4.4a) and c)), with adsorption energies of -0.36 and -0.69 eV on a flat and stepped surface, respectively. (The measured ethylene desorption energy at low-coverage regime is 0.56 eV [100].) Close behind in stability ($\sim$ 0.1 eV for both flat and stepped surface) follows the top site, where the ethylene is found to bind through the π orbital (see Figs. 4.4e) and g)). However, molecular adsorption of ethylene on Pd(111) occurs only at temperatures below 300 K. At room temperature or higher, the ethylene dosing leads to instant formation of ethylidyne. The conversion must involve a breaking and formation of C-H bond. According to our calculations, the C-H activations are surface-mediated, because direct H-1,2-shifts have very high barriers. Based on the calculated activation energies of all alternative elementary reactions we propose that ethylene disproportionates to yield vinyl (CH-CH_2) and ethyl (CH_2-CH_3) on Pd. Both of these can further produce ethylidyne through the formation of ethylidene intermediate as depicted in Figure 4.3. The initial and transition state geometries belonging to the suggested reaction scheme are illustrated in Figures 4.4 and 4.5. The potential energy profile showing the energetics for the coexistent reaction paths is given in Figure 4.6. The route CH_2-CH_2* $\rightarrow$ CH-CH_2*+H* $\rightarrow$ CH-CH_3* $\rightarrow$ C-CH_3*+H* (1), is depicted in the left part of the PES, and the route CH_2-CH_2*+H* $\rightarrow$ CH_2-CH_3* $\rightarrow$ CH-CH_3* $\rightarrow$ C-CH_3*+H* (2) is shown on the righthand side. The (apparent) activation energy for the reaction C_2H_4(g) $\rightarrow$ CH-CH_2* + H* over Pd(111) is 0.89 eV. Assuming that at temperatures $T > 0$ the entropy loss upon adsorption increases the free energy of activation ($\Delta G^{\ddagger}$=$\Delta H^{\ddagger}$-T$\Delta S^{\ddagger}$) when compared to the reactions between the surface species, this dissociative adsorption step represents the bottleneck for the overall reaction on Pd(111) since the barriers for subsequent reactions are 0.90 and 0.34 eV. The route (2) requires the hydrogen from the route (1), and thus the ethylene dehydrogenation is expected to be the limiting step for both reaction paths.

Table 4.1: Reaction Energies, ΔE, and activation barriers, E_{act}, both in eV, for all the computed reactions in the ethylene decomposition to atomic C and H on Pd.

	Step no.	ΔE (111)	E_{act} (111)	ΔE (211)	E_{act} (211)
dehydrogenation					
$H_2C\text{-}CH_2^*+^* \leftrightarrow HC\text{-}CH_2^* + H^*$	1	0.38	1.25	0.47	1.13
$H_2C\text{-}CH_3^*+^* \leftrightarrow H_2C\text{-}CH_2^* + H^*$	2	-0.29	0.65	-0.29	0.55
$H_2C\text{-}CH_3^*+^* \leftrightarrow HC\text{-}CH_3^* + H^*$	3	0.05	0.96	0.06	0.67
$HC\text{-}CH_3^*+^* \leftrightarrow HC\text{-}CH_2^* + H^*$	4	0.04	0.94	0.18	1.04
$HC\text{-}CH_3^*+^* \leftrightarrow C\text{-}CH_3^* + H^*$	5	-0.68	0.34	-0.10	0.77
$C\text{-}CH_3^*+^* \leftrightarrow C\text{-}CH_2^* + H^*$	6	0.5	1.35	0.51	1.40
$C\text{-}CH_2^*+^* \leftrightarrow C\text{-}CH^* + H^*$	7	0.74	1.48	0.52	1.14
$C\text{-}CH^* + ^* \leftrightarrow C\text{-}C^* + H^*$	8	0.74	1.59	0.24	1.02
$CH^* \leftrightarrow C^* + H^*$	9	0.46	1.48	-0.23	0.80
C-C splitting					
$C\text{-}CH^* + ^* \leftrightarrow C^* + CH^*$	10	-0.01	1.50	-0.20	1.41
$C_2^* + ^* \leftrightarrow 2C^*$	11	0.29	1.43	-0.67	1.65
$H_2C\text{-}CH_2^*+^* \leftrightarrow 2CH_2^*$	12	1.16	2.12	0.96	1.69
$C\text{-}CH_3^*+^* \leftrightarrow C^* + CH_3^*$	-	1.38	>2.50	0.41	1.70
$C\text{-}CH_2^*+^* \leftrightarrow C^* + CH_2^*$	-	1.14	2.76	0.35	2.02

In addition to the particularly low barrier for ethylidene → ethylidyne conversion over Pd(111), the process stands out also because it is the only one having a significantly higher barrier on the stepped surface. This reflects the fact that the product species is less stable on Pd(211) (by ∼0.1 eV when calculated with respect to a gas-phase C-CH_3 radical). The best adsorption geometries of ethylidyne on Pd(111) and Pd(211) are shown in Figures 4.7a) and c). In both cases the structures have the lower carbon bonding to three Pd atoms and the internuclear axis is pointing directly away from the plane defined by these Pd atoms. However on the stepped surface, two of the bonds are formed to atoms on the low-coordinated edge. This suggests the binding should be stronger compared to the flat surface and shows that although the d-band center descriptor works well in many cases, it might sometimes fail to predict the adsorption trends. This is understandable since the ϵ_d is the simplest parameter describing the electronic structure and neglects the detailed structure of the d states that interact with the adsorbate. Understanding why the ϵ_d parameter fails to predict the ethylidyne binding would require elaborate electronic-structure analysis, such as conducted in the work by Vojvodic [101].

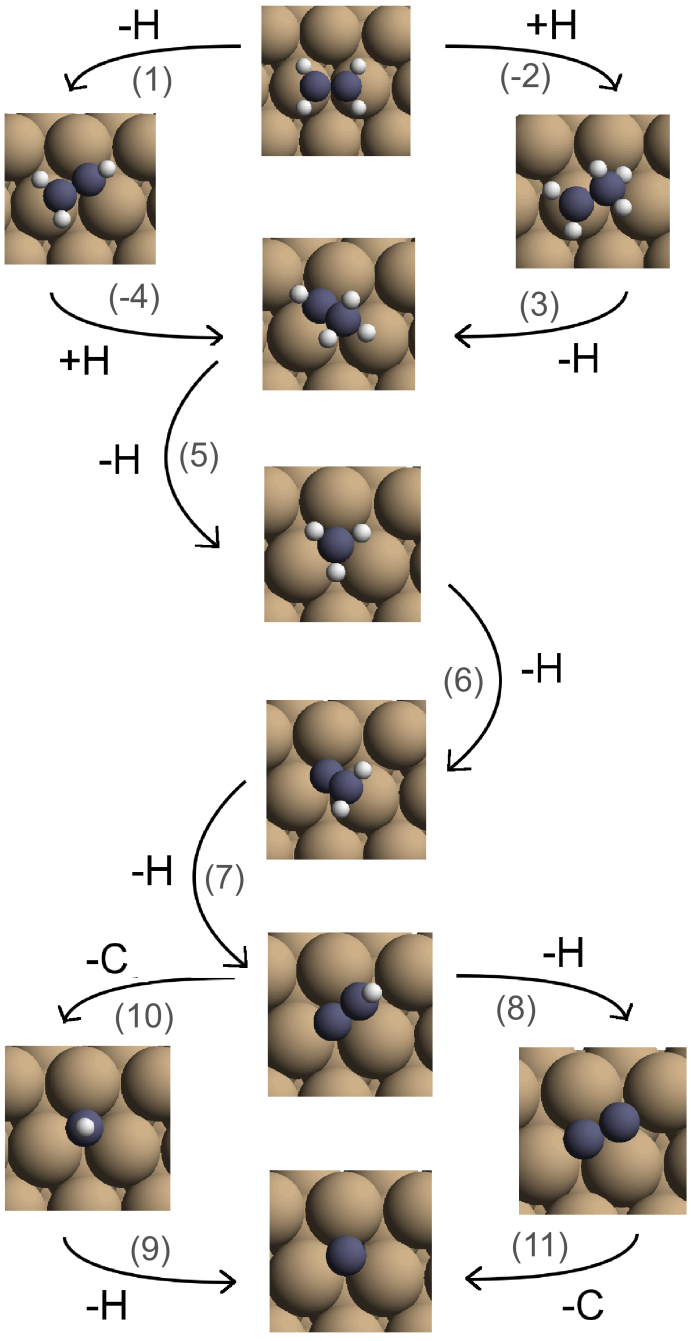

Figure 4.3: Proposed reaction steps from ethylene to atomic carbon on Pd surfaces. The numbering for reactions corresponds to the one used in Table 4.1

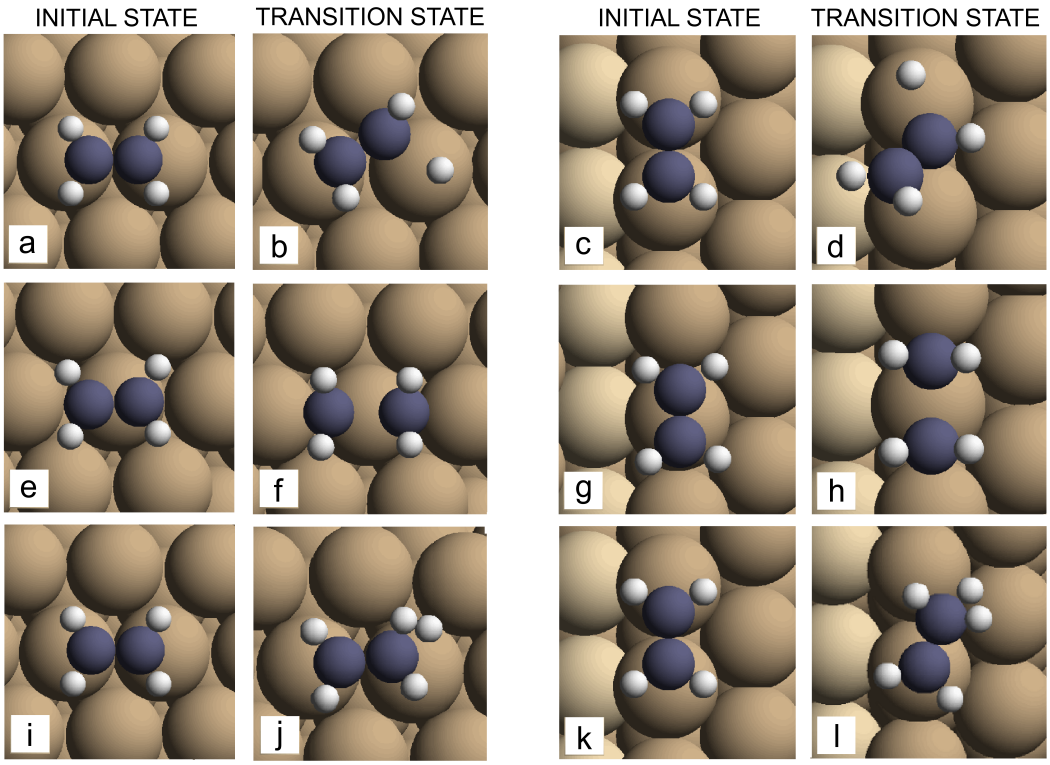

Figure 4.4: Optimized initial and transition state geometries for (a)-(d) ethylene dehydrogenation, (e)-(h) ethylene dissociation, and (i)-(l) ethylene hydrogenation on flat (left block) and stepped (right block) palladium surface. In the calculations, the hydrogen atom (not shown in the figure) is considered adsorbed in its most stable configuration infinitely far from the ethylene prior to the hydrogenation reactions. Brown color stands for palladium, blue for carbon, and white for hydrogen. In the step site illustrations, the lower terrace is marked with the lighter shade of brown.

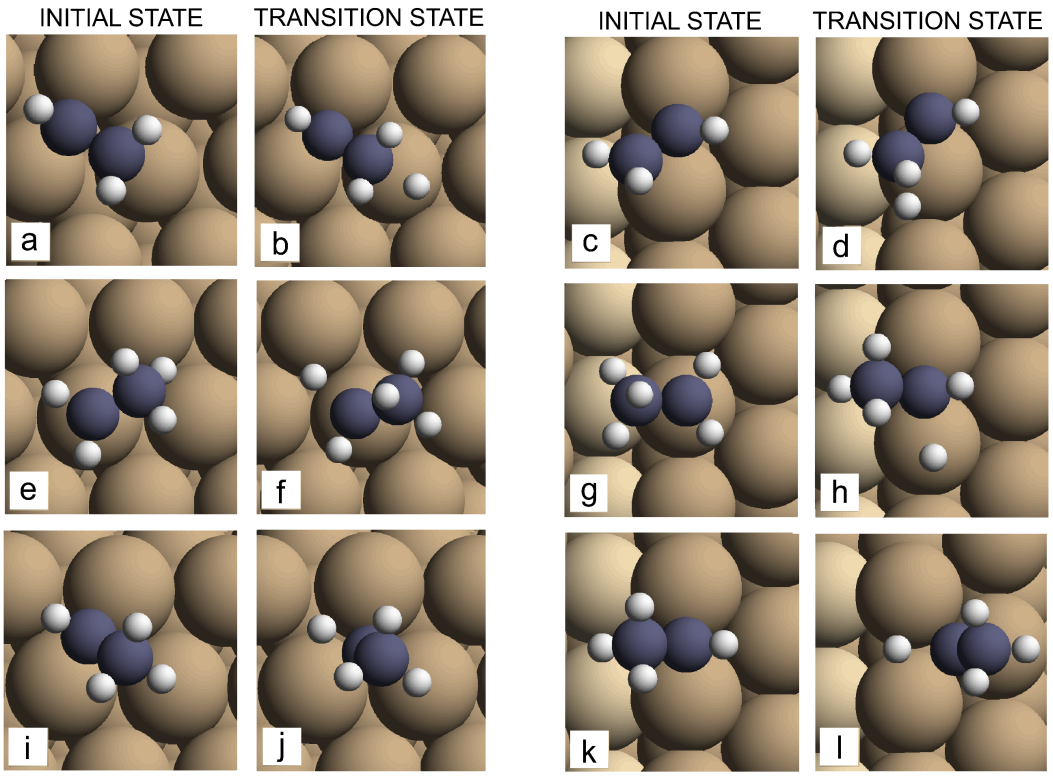

Figure 4.5: Optimized initial and transition state geometries for (a)-(d) vinyl hydrogenation, (e)-(h) ethyl dehydrogenation, and (i)-(l) ethylidene dehydrogenation on flat (left block) and stepped (right block) palladium surface. In the calculations, the hydrogen atom (not shown in the figure) is considered adsorbed in its most stable configuration infinitely far from the ethylene prior to the hydrogenation reactions. Brown color stands for palladium, blue for carbon, and white for hydrogen. In the step site illustrations, the lower terrace is marked with the lighter shade of brown.

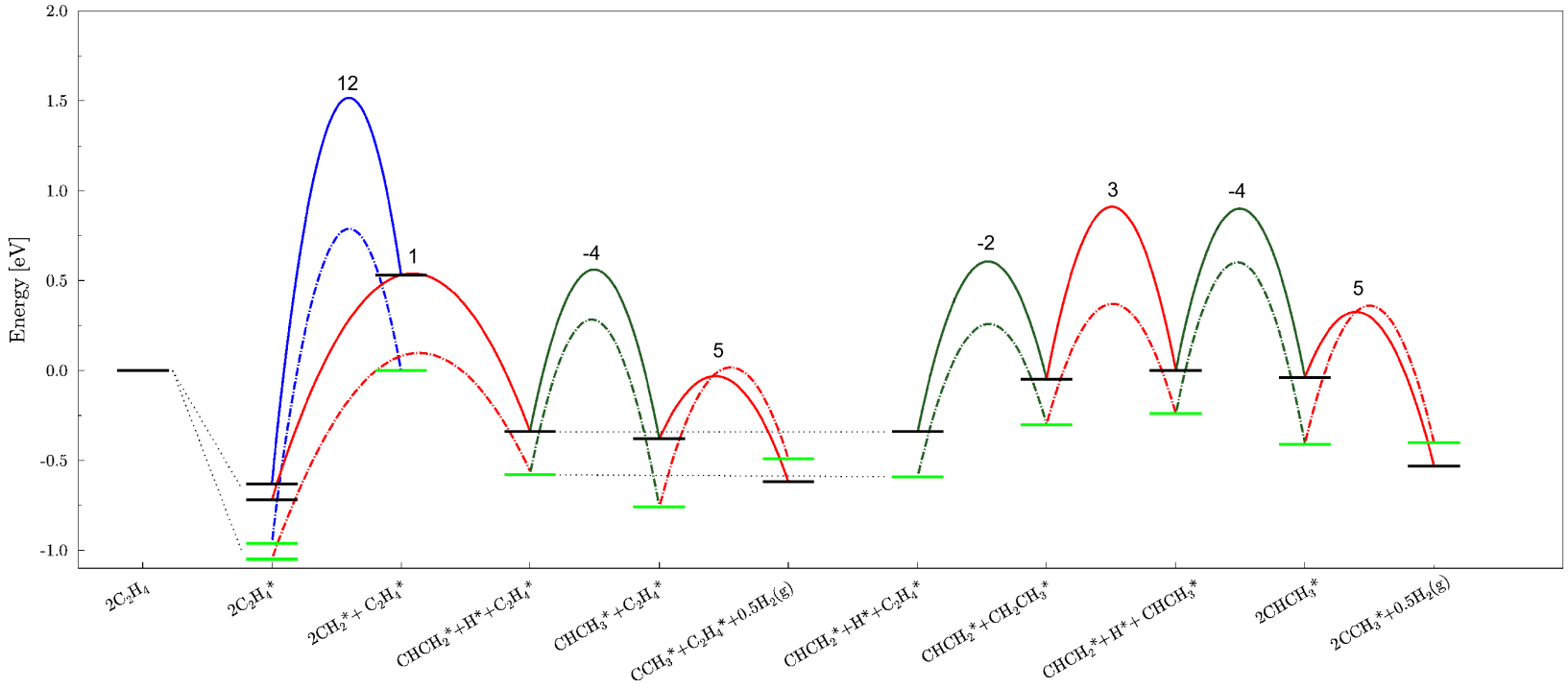

Figure 4.6: Potential energy diagram for ethylene decomposition to ethylidyne on Pd(111) and Pd(211) surfaces. Black (green) line represents the adsorption energies of the different hydro-carbon species on Pd(111) (Pd(211)). Transition state energies for C-C bond breaking, dehydrogenation, and hydrogenation reactions are illustrated with blue, red, and green lines, respectively. The solid line refers to a Pd(111) and dashed line to the Pd(211) surface. Note that the curved lines are drawn only to guide the eye, and only the top of the curves have an actual meaning depicting the transition state energies. The zero of energy is two ethylene molecules far away from the clean surface. Another ethylene molecule is needed to provide a hydrogen atom for ethylene hydrogenation step. It is assumed that there is a reservoir of molecules on the terrace, *i.e.* those molecules or fragments that are not involved in a particular reaction step sit on a terrace.The numbering for reactions corresponds to the one used in Table 4.1

To summarize, our computational evidence shows that the kinetics of room temperature ethylene-ethylidyne conversion on Pd(111) is governed by the ethylene dehydrogenation to vinyl with the reaction route passing through the ethylidene intermediate and agrees with predictions made by other computational groups [14, 17]. Although there is no experimental evidence concerning the exact reaction path on Pd, the activation energy has been estimated for the whole CH_2-CH_2(g) $\rightarrow$ C-CH_3* conversion near room temperature using kinetic models with measured data. Interestingly enough, the same data set seems to be used to derive two different activation energies for the process, 0.95 ± 0.04 eV [8] and 0.51 ± 0.05 eV [102]. If we compare our results with the previous experimental activation energy, our terrace result (0.89 eV) agrees reasonably well. If we do the comparison with the more recent value, the step result (0.44 eV) is compatible.

The articles do not provide explanation for the discrepancy but perhaps the analyzes employ different kinetic models. In the latter publication the good agreement with the computational barrier 0.48 eV calculated by Moskaleva *et al.* with PW91 functional was pointed out. However, question arises whether the excellent agreement is at least partly fortuitous. First, the experiments are performed in low pressure, implying that the barriers should be compared with the low-coverage PW91 value (0.1 eV [17]). Second, it is well-known that the PW91 functional overbinds molecules and lowers the intrinsic reaction barriers when compared to the RPBE functional [81, 4]. Indeed, the minimum ethylene binding energy with PW91 (for the highest coverage) is 0.74 eV, which is still 0.4 eV larger than our low-coverage RPBE value for the binding strength. Consequently, the apparent activation energy (the TS energy with respect to the gas-phase ethylene) calculated using PW91 shifts down remarkably compared to the RBPE result. Our RPBE barrier on Pd(111) with respect to the gas phase ethylene is 0.89 eV, $\sim$0.8 eV higher than the low coverage barrier calculated by Moskaleva *et al.* with PW91 functional. Finally, the effect of defects in the Pd(111) surface may well play a role in the reaction. Even though the fraction of step sites in the close-packed surface can be very small, the steps may still play a significant role in the reaction kinetics (see for example [65, 103] and references therein).

4.1.2 Ethylidyne decomposition and onset of PdC phase formation

Measurements show that the ethylidyne adlayer resists heating on Pd(111) up to 350 K, after which it starts to decompose, and at temperatures around 440 K complete carbon coverage is attained [10]. Just like in the case of ethylene-ethylidyne conversion, the exact mechanism for ethylidyne decomposition is not known from the experiments. Thus, computational studies are needed to explain this reaction mechanism.

The potential energy surface depicting the suggested reaction path for the full ethylene decomposition to atomic carbon and hydrogen is presented in Figure 4.8. Our results support the experimental finding that decompositions come into action sequentially with increasing temperature: Barriers related to the ethylidyne decomposition to atomic carbon are ∼0.5 eV higher compared to the activations during the ethylene-ethylidyne conversion on Pd(111). The calculations show that the surface species preceding the formation of CCH* prefer to dehydrogenate than go through the C-C bond cleavage. The majority of the calculated C-C bond cleavage barriers exceed 2 eV and even the lowest barrier (1.7 eV) associated with the ethylidyne decomposition to carbon and methylidyne fragment on Pd(211), does not compete with the reactions involving C-H bond activation. For ethynyl species on Pd(111), the opposite trend occurs, and the C-C cleavage actually costs ∼0.1 less energy than CCH dehydrogenation. The persistence of C-C bond down to C-CH* species is further supported by previous experiments [10, 104] and DFT calculations [18]. Note that C-C bond cleavage has been found to compete with the C-H bond activation on Ni in the presence of steps already at adsorbed ethylene level [103]. The transition state for C-C dissociation in ethylene over Ni(211) was calculated to be ∼0.5 eV lower in energy compared to the transition state for C-H breaking over Ni(111).

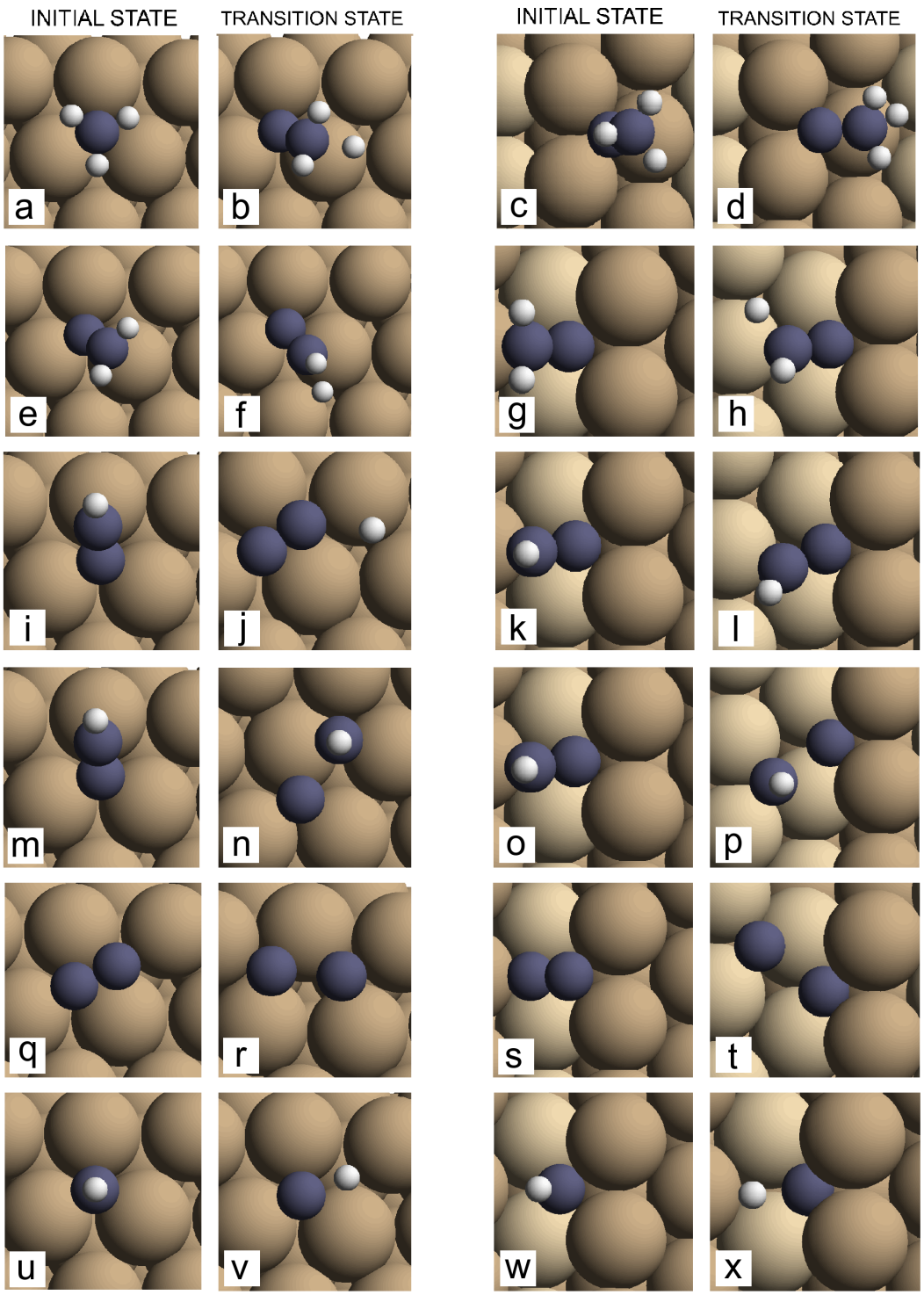

Figure 4.7: Optimized initial and transition state geometries for (a)-(d) ethylidyne dehydrogenation, (e)-(h) vinylidene dehydrogenation, (i)-(l) ethynyl dehydrogenation, (m)-(n) ethynyl dissociation, (q)-(t) carbon dimer dissociation, and (u)-(x) methylidyne dehydrogenation on flat (left block) and stepped (right block) palladium surface. Brown color stands for palladium, blue for carbon, and white for hydrogen. In the step site illustrations, the lower terrace is marked with the lighter shade of brown.

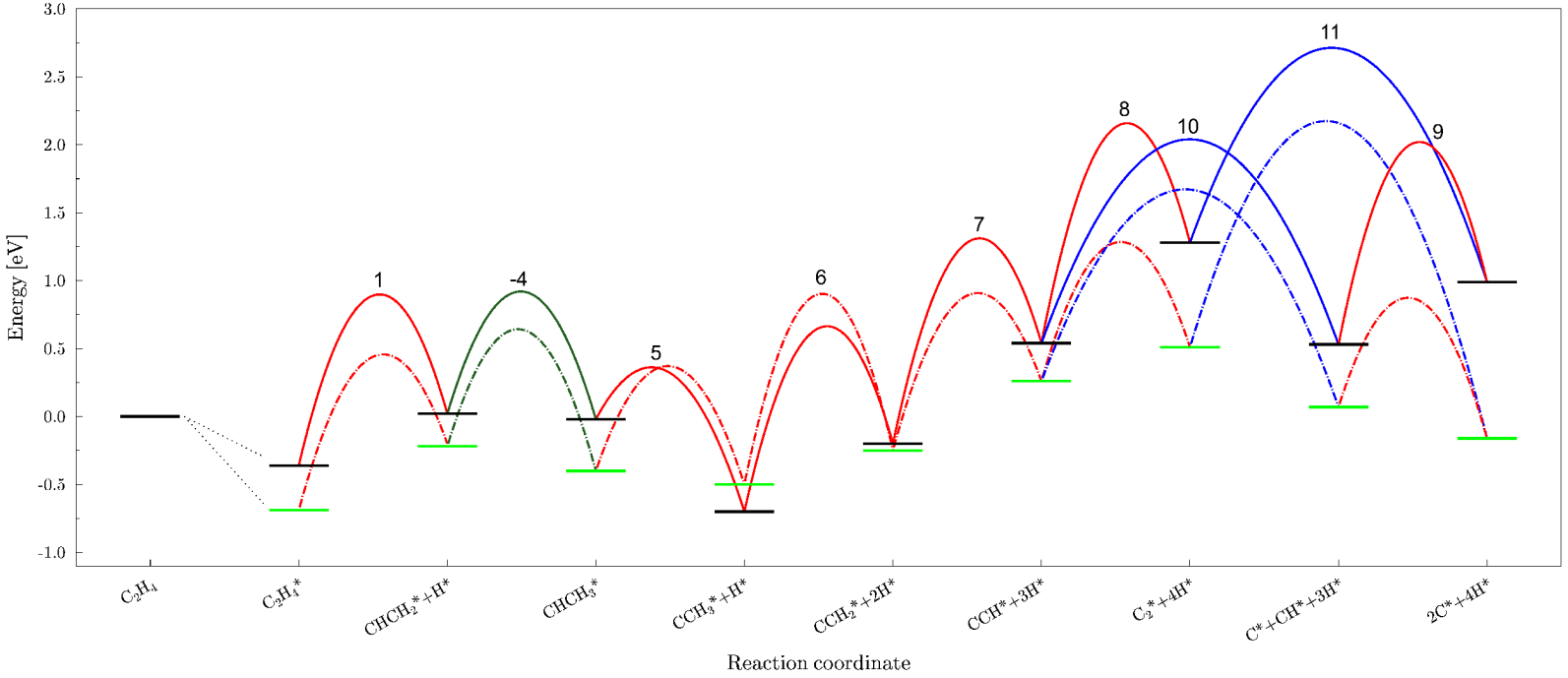

Figure 4.8: Potential energy diagram for ethylene decomposition on Pd(111) and Pd(211) surfaces. Black (green) line represents the adsorption energies of the different hydrocarbon species on Pd(111) (Pd(211)). Transition state energies for C-C bond breaking, dehydrogenation and hydrogenation reactions are illustrated with blue, red and green lines, respectively. The solid line refers to a Pd(111) and the dashed line to the Pd(211) surface. The zero of energy is ethylene far way from the clean surface. The numbering for reactions corresponds to the one used in Table 4.1

Most of the reactions are associated with lower activation barriers on the step compared to the terrace. Outstanding pronounced lowering is seen for the dehydrogenations from vinylidene forwards. The step brings the barrier down by 0.34, 0.57, and 0.68 eV for C-CH_2* → C-CH*+H*, C-CH* → C-C*+H*, and CH* → C*+H*, respectively. The reason behind the observed step effect is illustrated in Figure 4.7 showing the initial and transition states for the reactions from ethylidyne forwards on Pd(111) and Pd(211) surfaces. As the number of H atoms in adsorbed hydrocarbons decreases, the adsorbates begin to favor the 4-fold site under the step edge, where the hydrogen deficient carbons can form more bonds to the metal atoms. Whereas the C_2H_x, $x \geq 3$ species favor adsorption on the upper terrace of the Pd(211), the hydrocarbons C_2H_x, x=0-2, bind to a 4-fold site. This means that the geometric step effect really manifest itself for the dehydrogenated fragments. Steps also scramble the reaction route from ethynyl forward. While the ethylene decomposition to ethynyl can be expected to follow the path ethylene → vinyl (or ethyl) → ethylidene → ethylidyne → vinylidene → ethynyl regardless of the surface geometry, the C-CH* dehydrogenates to yield carbon dimer wherever step sites are available instead. On Pd(111) the preferential reaction of C-CH is the C-C bond cleavage and the production of methylidyne (CH).

At temperatures beyond 440 K the palladium starts to lose its bulk properties due to the migration of carbon atoms into the Pd lattice [10]. This eventually leads to the formation of a PdC phase displaying catalytic properties different from those of pure Pd. Our DFT calculations show that there is a thermodynamic driving force toward for subsurface diffusion. The carbon incorporates the first Pd interlayer with the migration barrier of around 0.5 and 0.1 eV on Pd(111) and Pd(211), respectively. The barriers are smaller than those associated with the lateral diffusion on top of the surface or within the immediate subsurface region, and considerably lower than the barriers needed to accommodate the second interlayer region. This implies that once there carbon produced on the surface, it accesses the region between the first and second Pd layer fast and remains there. Once again, the step sites show pronounced tendency to trap the carbon atoms, and since the 4-fold hollow site under the step edge is found to bind the carbons strongest, the steps can be expected to be readily populated. If the steps play a role in the catalytic reactions at hand, the site blocking by C can be expected to lead to considerable changes in the catalytic properties.

4.1.3 The BEP behavior

While the BEP relations are well established among similar reactions over variety of different elements, fewer studies address the linear trends involving different reactions taking place on the same transition metal. Our results indicate that the response of the changes in activation energies for C_2H_x (x=1-5) dehydrogenation over Pd shows linearity against varying the reaction energies (see Figure 4.9). The higher degree of

dispersion around the Pd(211) line reflects the more complex surface structure. The asymmetry provided by the step edge opens up more possible ways for the atoms in the reaction intermediates and activated complexes to organize themselves compared to the planar terrace. If the stabilization effect of the step edge is systematically more pronounced for the transition state structure compared to the reaction intermediates, the BEP line for stepped surface shifts down from the terrace line. This is seen for example in the studies concerning N_2 dissociation [64, 65], where the transition state stabilization offered by the step site results mostly from geometric effects, as described in section 2.3. In our case the downshift of the BEP line is very modest, only around 0.1 eV. It is difficult to say whether this negligible change in the line intersects actually originates from some geometric or electronic effects, or whether it is just an artifact.

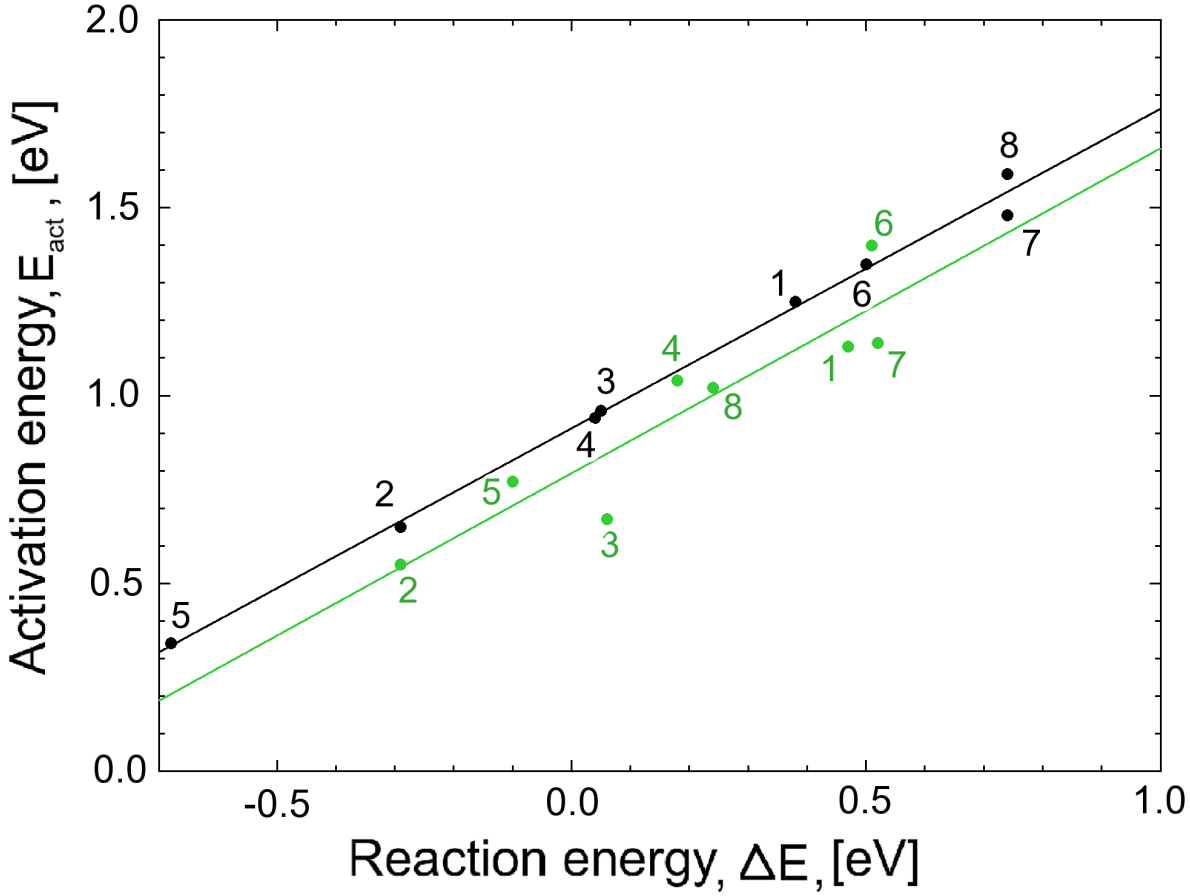

Figure 4.9: Brønsted-Evans-Polanyi type of relationship for the dehydrogenation steps of ethylene on Pd. The energies are given with respect to the initial state of the elementary reactions. Black (green) circles stand for terrace (step) reactions. The numbering for reactions corresponds to the one used in Table 4.1.

The data points characterizing the C-C bond scission deviate notably from the BEP lines for C_2H_x* → C_2H_{x-1}*+H* reactions. Also the points for CH* → C*+H* diverge somewhat. Thus, it can be concluded that the BEP behavior only realizes for certain

type of reactions at the time. The same kind of categorization between the reactions involving C-H, C-O, C-C, O-H is observed for reactions of ethanol over Pd [105] and Pt surfaces [106].

4.2 Pd-catalyzed hydrodehalogenation of TCE

Next, the trichloroethene hydrodechlorination process over Pd(111) is studied with aim to map the energy landscape for the reaction, and shed light on the reaction pathway under debate. Our adsorbate coverage is 1/12 from performing the calculations in the unit cell marked with a solid line in Figure 4.18. To take into account the effects of possible chlorine coadsorbates at the catalyst surface (see the following discussion), the studies have been conducted both on clean and Cl-covered surface. As discussed in the introduction chapter the removal of chlorine from the catalyst surface is essential to maintain its activity. We start by addressing the effect of reaction environment (gas vs. water phase) to the presence of chlorine on the surface.

4.2.1 Effect of reaction environment on surface Cl content

The chlorine from the TCE reduction can be expected to accumulate on the surface if the reaction environment is not appropriate, *i.e.* the Cl solvating water lacks, or the gas phase reaction temperature is below ∼460 K [35]. In order to verify this theoretically, we calculated the desorption and solvation enthalpies for HCl from Pd surface. The energy input might of course depend on kinetic effects, but these have been neglected to a first approximation. Since chemisorbed HCl desorbs recombinatively from Pd(111) [107], we calculated the energy change between a system, where H and Cl are initially chemisorbed infinitely far from each other, and system where HCl is in a gas phase. This choice gives us a desorption enthalpy of 1.30 eV.

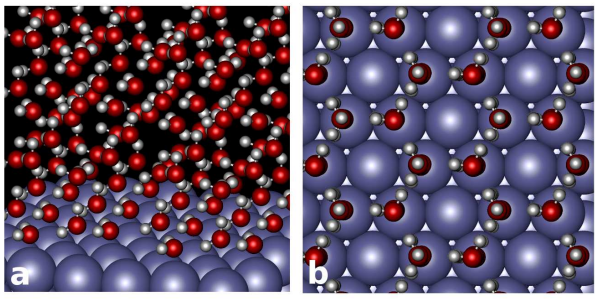

Figure 4.10: Optimized fourfold water bilayer on Pd(111) from the a) side and b) top.

For estimating the effect of water phase to the HCl removal energetics, we incorporated explicit water molecules into our computational cell. The hexagonal ice-like structures with bilayer geometry are suggested to form near the closed-packed transition metal surfaces [108], and have been successfully used to describe the effect of water to the surface chemistry [109]. Thus, we stacked four water layers in an arrangement illustrated in Figure 4.10. Based on the previous DFT calculations, surrounding water molecules ionize HCl into separated Cl^- and H_3O^+ species [110]. Thus, for our final state of HCl solvation, we substituted one H_2O in the third water bilayer by chlorine, and formed a hydronium species from one of the water molecules in the second bilayer, in line with the previous work. The HCl solvation energy is calculated as

$$E_{solv} = [E_{4BL}(Cl^- + H_3O^+) + E_{4BL}] - [E_{4BL}(Cl*) + E_{4BL}(H*)], \qquad (4.1)$$

where $E_{4BL}(Cl^- + H_3O^+)$ is the total energy of the system of Cl^- and H_3O^+ in the water layers, $E_{4BL}(Cl*)$ corresponds a system where chlorine substitutes a water molecule in the adsorbed bilayer, $E_{4BL}(H*)$ gives the energy when hydrogen is located in a 3-fold hollow site within the hexagonal H_2O ring, and finally E_{4BL} stands for the total energy of the mere slab+water -system. The structures correspond the most stable geometries reported in Ref. [111]. The obtained value for E_{solv} is 0.56 eV, which is less than half the desorption energy of HCl into the gas phase. Thus, basing on the enthalpy changes and neglecting the coverage effects, our results indicate that the water phase indeed promotes the removal of HCl from the catalyst surface.

As a first approximation we assume that water phase contributes to the TCE HDC mainly through its coupling with the surface chlorine content. Surrounding water might also affect for example the reaction energetics, but these effects have not been addressed in the present work.

4.2.2 Reaction pathway and the effect of coadsorbed chlorine

Next, the most probable reaction mechanism on the grounds of intrinsic activation energies over clean and Cl-covered Pd(111) is discussed. Figure 4.11 shows the constructed reaction network and all the calculated reaction parameters are listed in Table 4.2. The optimized initial, transition, and final states for the studied reactions on the clean slab are illustrated in Figures 4.12 and 4.13.

On Cl-free Pd(111) dechlorinations are clearly preferred over hydrogenations. The highest barrier in the course of TCE dechlorination (0.55 eV) is still ∼0.15 eV below the lowest hydrogenation barrier of chlorinated species within the reaction network. The initial length of the dissociating C-Cl bond is identified as a fair descriptor of the activation energy. Figure 4.14 shows that the increase in initial bond length leads

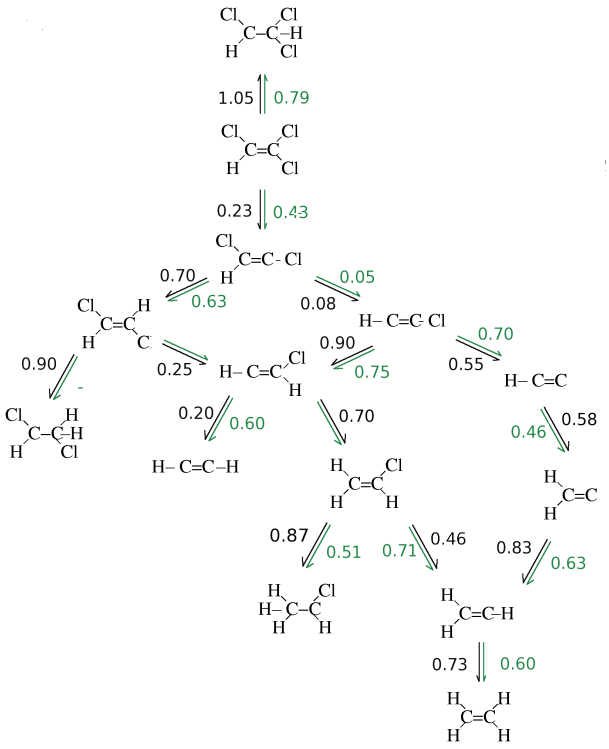

Figure 4.11: The reaction network summarizing the studied candidate elementary steps in the hydrodechlorination of trichloroethene. The black numbers give the calculated activation energies on the clean Pd(111), and the green numbers are the corresponding figures in the presence of coadsorbed chlorine.

to decrease in activation energy. Following the dechlorination steps CHCl-CCl_2* → CHCl-CCl* → CH-CCl* → C-CH*, the C_2 framework hydrogenates to form ethene via vinylidene (-C-CH_2) and vinyl (CH-CH_2). The bottleneck of the overall TCE → ethene conversion is the step C-CH_2*+H* → $CHCH_2$* with activation energy of 0.83 eV. Note, that the evolution through DCE and VC intermediates requires competition between dechlorination and hydrogenation before the formation of the -CCH. Thus, our calculations for Cl free Pd(111) at low adsorbate coverage support the direct reaction pathway, supporting the interpretations from Refs. [20, 21, 27].

Next the effect of coadsorbed chlorine on the reaction energetics is addressed. Our models employ the suggested maximum Cl coverage [112], where the interhalogen separations reach twice the van der Waals radius of Cl. Figure 4.15a) shows the chlorine covered surface, and Figures 4.15b) and c) illustrate the hydrogen and TCE coadsorbed with Cl. The surrounding halogens weaken the binding for both species, but for TCE the effect is strong: binding energy drops ∼0.6 eV resulting in thermoneutral chemisorption. This owes to the fact that TCE requires a relatively large surface area forcing the three chlorines to move closer and maximize the repulsive interactions in the final state of the chemisorption onto the Cl-covered surface. Our

Table 4.2: Reaction energies, ΔE, and activation energies, E_{act}, both in eV, for calculated elementary reactions over clean and chlorine-covered Pd(111) (latter given in parenthesis). The activation energies estimated from the Brønsted-Evans-Polanyi fitting (see 4.16) are marked with an asterisk. The $\Delta G^{\ddagger}$ (see 4.2) counterparts of the activation energies marked with a letter are a) 0.34 eV b) 0.21 eV c) 0.74 eV d) 1.27 eV e) 0.70 eV.

	ΔE	E_{act}
Dechlorinations		
$CClH\text{-}CCl_2^*$ → CClH-CCl* + Cl*	-1.08 (-0.38)	0.23[a] (0.43)
CClH-CCl* → CH-CCl* +Cl*	-0.96 (-0.23)	0.08 (0.05)
CH-CCl* → C-CH* + Cl*	-0.24 (0.13)	0.55 (0.70)
CH_2-CHCl* → CH_2-CH* + Cl*	-0.38 (0.02)	0.46[b] (0.71[c])
CH-CClH* → CH-CH* + Cl*	-0.86 (0.08)	0.21* (0.60*)
Hydrogenations		
CCl_2-CClH* + H* → $CClH_2\text{-}CCl_2^*$	0.19 (-0.21)	1.05[d] (0.79)
CClH-CCl* +H* → CClH-CClH*	-0.20 (-0.25)	0.70 (0.63)
C-CH* + H* → $C\text{-}CH_2^*$	-0.82 (-1.10)	0.58 (0.46)
$C\text{-}CH_2$ +H* → CH-CH_2*	0.21 (-0.05)	0.83 (0.63)
CH-CH_2* +H* → $CH_2\text{-}CH_2^*$	-0.34 (-0.56)	0.73 (0.60)
CH_2-CHCl*+H* → CH_3-CHCl*	0.01 (-0.25)	0.87* (0.51[e])
CH-CCl* +H* → CH-CClH*	0.04 (-0.18)	0.91 (0.77*)
CH-CClH* +H* → CH_2-CClH*	-0.28 (-0.61)	0.70* (0.60*)
CHCl-CClH*+H* → CH_2-CClH*	-0.81 (N/A)	0.90* (N/A)

results show that the chlorine also modifies the reaction energies and activation barriers. In general, chlorine hinders dechlorinations by increasing the activation barriers and making the chlorine cleavage thermodynamically less favorable. Exactly the opposite effect is seen for hydrogenations, which become more feasible in the presence of halogens. The observation can be rationalized from the BEP-behavior of the obtained reaction energetics, depicted in Figure 4.16. While it can be assumed, that the coadsorbed chlorine weakens the binding of both initial and final state adsorbates of the elementary reactions, the effect is stronger in that side of the reaction (reactant or product), where the repulsive interactions are more pronounced. In the case of dechlorination, the final state with an extra Cl accommodated on the surface shifts more upward in energy than the initial state, compared to the chlorine-free surface. This reduction in the exothermicity is reflected in the higher barrier through the BEP rule. The opposite holds for hydrogenation process, where the Pd atoms are more shared in the initial state compared to the final state, and the reactions become more exothermic compared with those taking place on bare Pd(111).

Despite of the converging trend of the activation barriers between C-Cl breaking and C-H forming, coadsorbed chlorine does not have a strong effect on the TCE HDC mechanism. Regardless of the amount of halogens on the surface, TCE loses two chlorines relatively easily forming chlorinated acetylene. However, whereas on the surface of low chlorine loading the next step is clearly the breaking of the last C-Cl bond, the high amount of coadsorbed chlorine triggers competition between the Cl cleavage and C-H bond formation from the CH-CCl* level based on the insignificant differ-

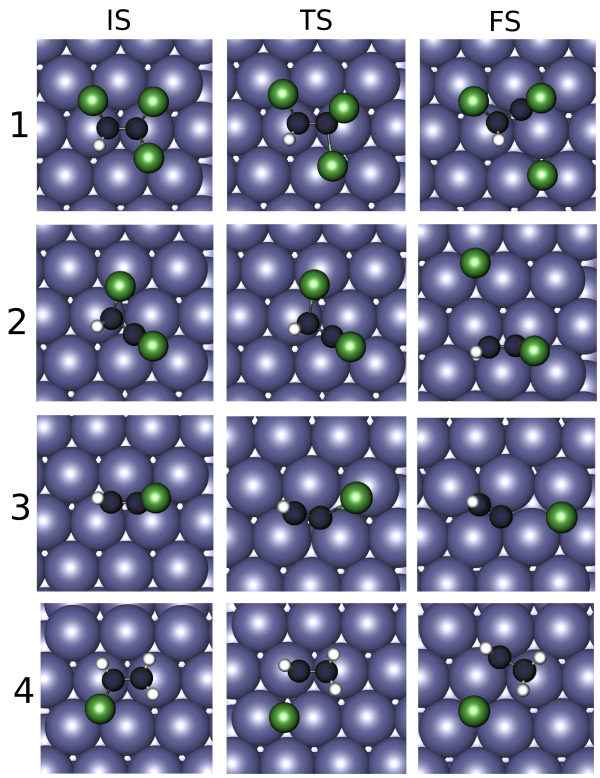

Figure 4.12: The optimized initial, transition, and final state geometries (columns marked with IS, TS, FS accordingly) of the dechlorination of a) TCE, b) C_2Cl_2H, c) C_2ClH, and d) vinyl chloride over Pd(111).

ence (0.05 eV) between the activation energies. This might lead to partial formation of DCE, VC, and acetylene, assuming that CH-CHCl* acts as a precursor for these compounds.

4.2.3 The reactivity ordering among chlorinated ethenes

So far the calculations have suggested that the TCE HDC proceeds via direct pathway, and the rate limiting step (RLS) in the course of bond activations is among the hydrogenations taking place after the chloroethene is dechlorinated to C-CH. Based on the late location of the RLS in the reaction coordinate, the HDC rate dependence on concentration of the reactant should be complex. This implies that the rate constant for the overall reaction cannot be deduced reliably from experiments assuming first order kinetics with respect to the chloroethene disappearance from the gas phase or solution. However, this is what is normally being done, and thus in order to make comparison to experiments, the reactivity ordering among the chlorinated ethenes needs

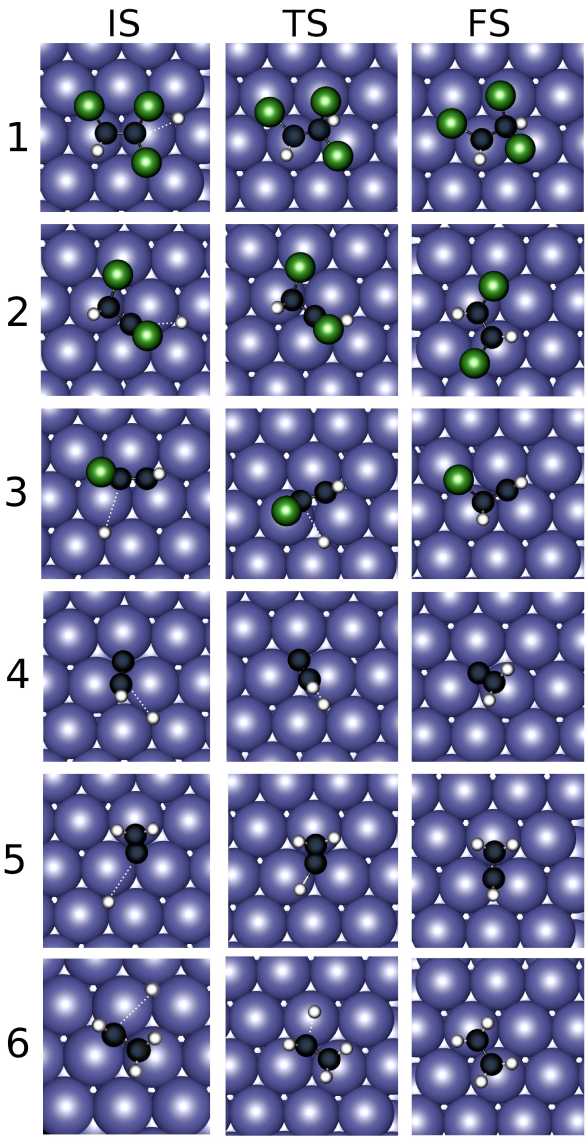

Figure 4.13: The optimized initial, transition, and final state geometries (columns marked with IS, TS, FS accordingly) of the hydrogenation of a) TCE, b) C_2Cl_2H, c) C_2ClH, d) C-CH, e) C-CH_2, and f) CH-CH_2 over Pd(111). The dotted white line connecting the carbon and hydrogen is added to guide the eye.

to be evaluated from adsorption energetics. For doing this, we have considered the apparent activation energies of dissociative (-Cl) and associative (+H) adsorption with vibrational energy and entropy corrections. The free energy of apparent activation is calculated via

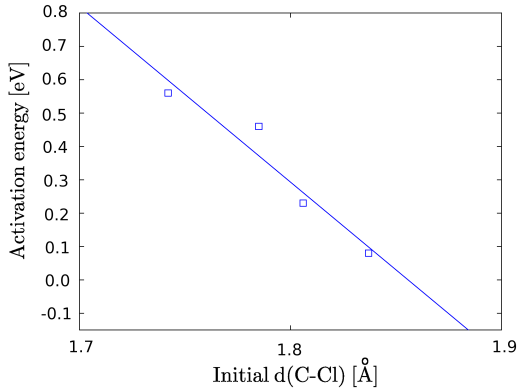

Figure 4.14: Activation energy of the dechlorination steps plotted as a function of the interatomic distance of the activating C-Cl bond in the initial geometry.

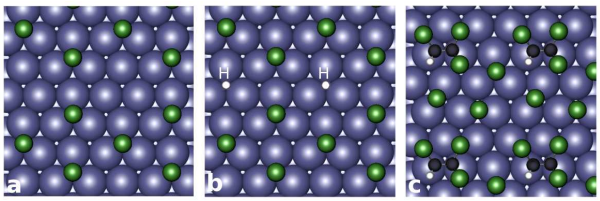

Figure 4.15: The optimized structures of a) chlorine covered Pd(111), b) hydrogen and c) TCE coadsorbed with chlorine on Pd(111).

$$\Delta G^{\ddagger} = E_{TS}^{ZP} - [E_{gas}^{ZP} + E_{slab}^{ZP}] - T\{S_{TS} - [S_{gas} + S_{slab}]\}, \tag{4.2}$$

where E_{TS}^{ZP}, E_{gas}^{ZP}, and E_{slab}^{ZP} are the zero-point energy corrected DFT total energies of the activated complex, chlorinated ethene in gas phase, and the slab, respectively. The entropies of these systems in same order, denoted as S_{TS}, S_{gas}, and S_{slab}, were obtained at 298 K. The entropy for the gas phase species was taken from Ref. [113], and the other two values were calculated using the procedure from Ref. [114].

The $\Delta G^{\ddagger}$ values for TCE dechlorination and hydrogenation over bare Pd are 0.34 and 1.27 eV, respectively. This confirms that TCE is dechlorinated prior to the first H addition step. The calculated $\Delta G^{\ddagger}$ of VC dechlorination is 0.13 eV less than the 0.34 eV obtained for TCE dechlorination. So even though the *intrinsic* reaction barriers and C-Cl bond strengths suggest otherwise, VC dechlorinates faster than TCE when introduced onto the surface. Also, the experimentally observed shift in the VC reaction pathway as reaction conditions change [35] can now be rationalized from the calculated free energies. At low temperatures in the gas phase, when chlorine can be assumed to be present on the surface, VC has been observed to hydrogenate to ethyl chloride rather than hydrodechlorinate to ethane. The calculated $\Delta G^{\ddagger}$ values

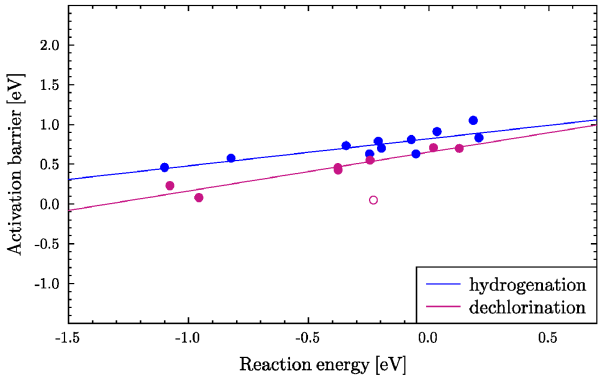

Figure 4.16: The calculated activation energies of the elementary reactions plotted as a function of the corresponding reaction energies. Blue color is used for hydrogenations, and violet for dechlorinations. The point with the largest deviation (reaction $CClH - CCl* \rightarrow CH - CCl* + Cl*$ in the presence of Cl, marked with an open circle) is excluded from the linear fit.

for the VC dechlorination and hydrogenation activations on chlorine-covered surface are 0.74 and 0.70 eV, respectively. Thus, coadsorbed Cl clearly induces competition between C-Cl breaking and C-H forming reaction reactions for VC, supporting the interpretations from measurements [35].

4.3 Characterization of active Pd-Au structures for TCE HDC

Next we aim at explaining the mechanism by which Au promotes the Pd-catalyzed TCE HDC reaction. Given that the precise structure of the Pd/Au bimetallic TCE HDC catalyst lacked evidence by the time we worked with the subject, the essential part of our study consists of identifying the potential Pd/Au structures based on their stabilities and ability to bind the reactants.

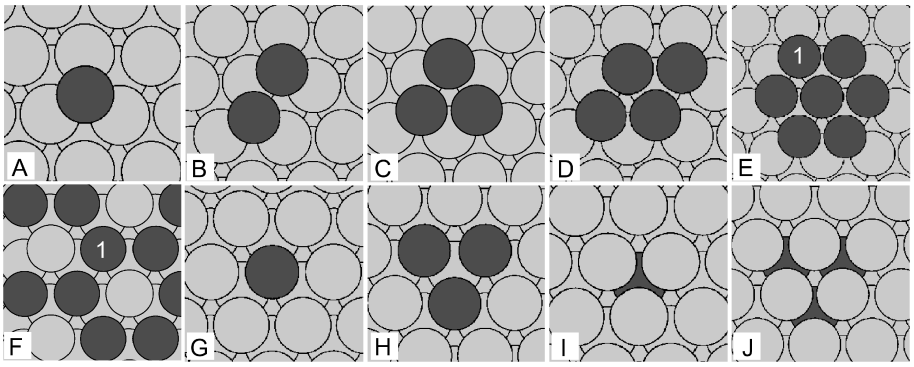

Figure 4.17: The optimized geometries of the Pd/Au structures. (A) Pd_1/Au, (B) Pd $_2$/Au, (C) Pd_3/Au, (D) Pd_4/Au, (E) Pd_7/Au, (F) Pd_8/Au_4- mix-s (G) Pd_1-mix-s, (H) Pd_3-mix-s, (I) Pd_1-mix-ss, and (J) Pd_3-mix- ss. Note that in structures (A)-(E) the Pd ensembles consist of adatoms located on top of Au(111) whereas in structures (F)-(J) Pd's are embedded in the Au(111) lattice replacing Au atoms. The study also covers structures, where the atom marked with "1" in figures (E) and (F) has been replaced by Au. The illustrations of $Pd_6/Au_1/Au$ and Pd_7/Au_5-mix-s are referred to as $1E^{(1)}$ and $1F^{(1)}$.

4.3.1 Modeling the Pd-on-Au catalyst

We have outlined the studied structures to represent compositions of a Au-rich core and Pd-rich surface as suggested by the experiments [39, 115]. The measurements indicate that the most active compositions are Au nanoparticles surrounded by an incomplete shell of Pd atoms and that this shell is most likely in the form of 2D Pd clusters [29]. The most active catalyst is suggested to have 70 % Pd coverage at least when the particle size is varied between 4 and 20 nm [39].

We model the gold nanoparticle facet with a four atom layer thick Au(111) slab, where varying amounts of Pd atoms per unit cell either sit on top of the lattice or replace atoms in either first or second Au layer. Figure 4.17 depicts the set of surface structures chosen to represent the different possibilities, and introduces the used nomenclature. The chosen unit cells are shown in Figure 4.18. In order to rank

the different compositions according to their thermal stability, we have calculated their formation energies defined here as the

$$E_f = [E_{PdAu} + N_{Au}E_{Au-bulk} - (E_{Au-slab} + N_{Pd}E_{Pd-atom})]/N_{Pd}, \tag{4.3}$$

where E_{PdAu}, $E_{Au-bulk}$, $E_{Au-slab}$, and $E_{Pd-atom}$ are the total energies of the PdAu surface, bulk Au (per atom), clean Au(111) slab, and isolated Pd atom, respectively. N_{Pd} is the number of Pd atoms in the alloy structure (per unit cell), and N_{Au} is the amount of gold atoms replaced by Pd (per unit cell). Note that for the Pd islands and the overlayer, N_{Au} equals zero. The more negative value of E_f translates to the more stable configuration.

Figure 4.19 illustrates the stability of the Pd atom in different atomic environments. There is a clear thermodynamical driving force into intermixing of Pd and Au. Among the islands, the Pd atoms are more stable in larger clusters, the flat overlayer being the most energetically favored structure. To test the tendency of Pd atoms to form 3D instead of 2D clusters, we calculated a formation energy for a Pd_4 structure, where the fourth Pd atom is in a 3-fold hollow site on top of a Pd_3 cluster (tetrahedral structure). The obtained formation energy is almost 0.2 eV less negative for the piled structure. Calculations show also that although isolated Pd atoms are not likely to be present on a Au(111) surface, they are preferred in the mixed compositions. The change in the stability can be seen by comparing the formation energies of Pd_1 and Pd_3 mixed structures.

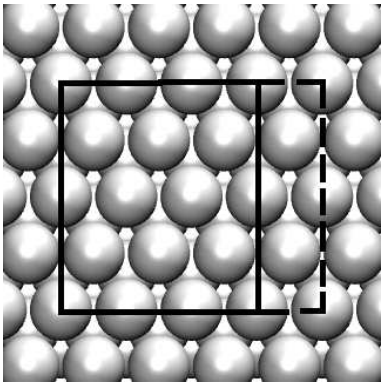

Figure 4.18: Top view of the fcc(111) unit cell(s) used for modeling the Pd/Au(111) surfaces. The larger unit cell (extended by dashed line) was used for setting up the seven atoms containing islet on Au to ensure adequate distance between the cluster and its periodic image, while the smaller cell was employed in the rest of the calculations.

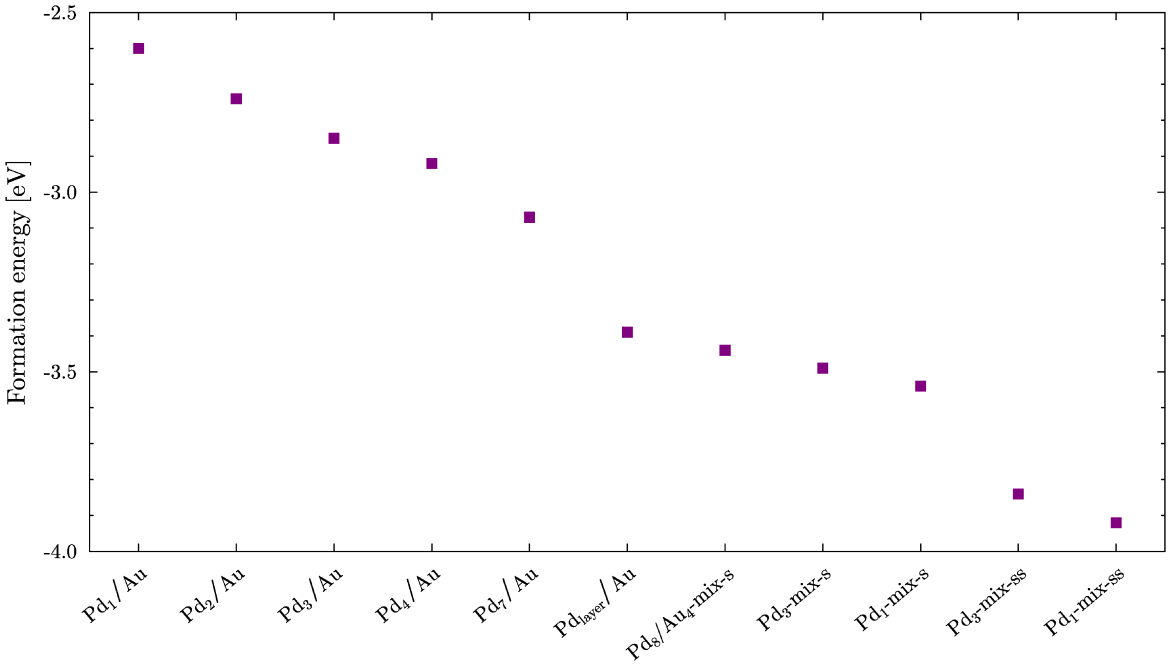

Figure 4.19: The formation energy per Pd atom as a function of the corresponding Pd/Au structure. The nomenclature of the structures is introduced in Figure 4.17.

4.3.2 Adsorption on the Pd/Au surfaces

Next, the abilities of the different Pd/Au surfaces to bind H, Cl, and the ethenes with varying chlorine content are compared. The calculated adsorption energies of TCE, DCE isomers, VC, ethene, chlorine, and hydrogen are collected in Tables 4.3 and 4.4. As expected from the inert nature of gold, pure Au(111) shows low tendency to bind TCE. Replacing Au atoms by Pd on the top layer of Au(111) does not really increase the adsorption ability of the surface. Even if the fraction of implemented Pd atoms is twice as much as that of Au atoms in the surface layer (see Fig. 4.17F), the resulting adsorption energy remains modest, -0.36 eV. Since surface alloy structures bind TCE weakly, it is unlikely that these type of surfaces are responsible for hydrodechlorinating TCE. The Pd islet structures on the other hand exhibit good binding properties, passing also the pure Pd(111). Figure 4.20 shows that the smallest Pd clusters are the most effective for capturing TCE. However, the smallest Pd clusters cannot offer the needed space for the HDC reaction, and this limits the cluster size from below. Note that since the Au clearly promotes the binding of Cl, the effect of alloying to prevent poisoning by chlorine remains unclear.

Table 4.3: Adsorption energies of TCE (E_{ads}(TCE)), d-band centers (E_d), and formation energies (E_f) corresponding to the different surface compositions. All energies are in eV.

Structure	Related Fig(s)	E_{ads}(TCE)	E_d	E_f
Au(111)	-	-0.05	-3.24	-
Pd_1/Au	4.17A,4.20	-0.77	-1.14	-2.60
Pd_2/Au	4.17B,4.20	-1.22	-1.23	-2.74
Pd_3/Au	4.17C,4.20	-1.24	-1.31	-2.85
Pd_4/Au	4.17D,4.20	-1.26	-1.34	-2.92
Pd_7/Au	4.17E,4.20	-1.06	-1.43	-3.07
Pd_{layer}/Au	4.20	-0.63	-1.40	-3.39
Pd(111)	4.20	-0.57	-1.73	-
Pd(111)-strain	-	-0.74	-1.67	-
Pd_8/Au_4-mix-s	4.17F	-0.36	-1.90	-3.44
Pd_1-mix-s	4.17G	0.23	-	-3.54
Pd_3-mix-s	4.17H	-0.14	-	-3.49
Pd_1-mix-ss	4.17I	-0.02	-	-3.92
Pd_3-mix-ss	4.17J	-0.07	-	-3.84

Table 4.4: Calculated adsorption energies (in eV) of chlorinated ethenes, H, and Cl given relative to the corresponding stable gas phase species on different Pd/Au structures.

Adsorbate	Pd_7/Au	Pd_{layer}/Au	Pd(111)
1,1-DCE	-1.10	-0.76	-0.69
cis-DCE	-1.10	-0.73	-0.65
trans-DCE	-1.18	-0.85	-0.75
VC	-1.17	-0.84	-0.77
ethene	-1.19	-0.91	-0.89
Cl	-1.90	-1.94	-1.64
H	-0.64	-0.72	-0.58

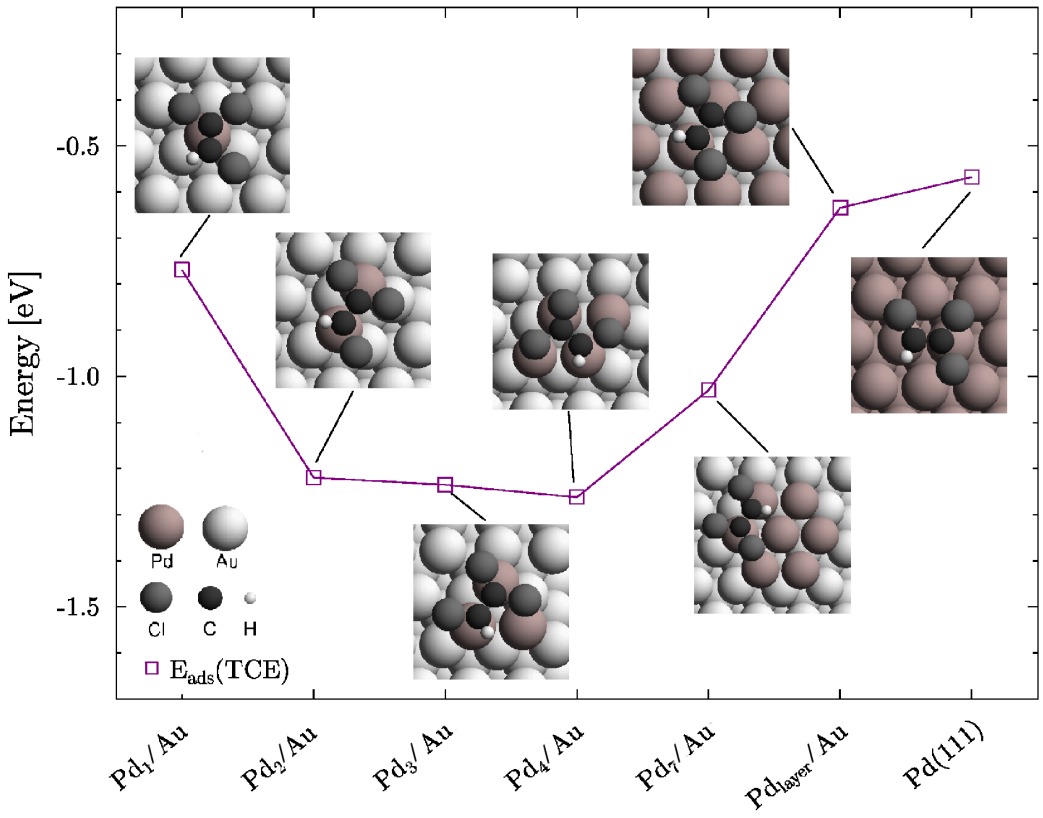

Figure 4.20: Calculated adsorption energies of trichloroethene plotted against the Pd/Au structures with increasing Pd content from left to right. The data points are associated with the illustration of the preferred adsorption geometry. Note that in all structures the Pd atoms are located on top of Au(111), and have not replaced any of the Au atoms.

4.3.3 Explaining the adsorption trends

We now know that the Pd/Au catalyzed TCE HDC is most active over the flat Pd clusters formed on top of Au based on the thermodynamic driving force towards 2D clustering and the ability of these clusters to hold on to the reactant. Our assumption that the thermodynamically most favored Pd/Au mixing is negligible due to the kinetic hindrance is supported by experimental studies [116, 117, 118, 29]. The next interesting question relates to the reasons behind the observed tendencies. As explained in chapter 2, there are various different effects contributing to the binding ability of the bimetallic surface. Keeping the binding ensemble fixed, the total effect of coordination, straining, and ligand surroundings is enclosed in a single parameter, the d-band center of the metal surface. We observe, that the correlation between the TCE adsorption energies and the ϵ_d is very good when the d-states of the topmost metal layer (whether complete or incomplete) are taken into account and the binding ensemble is being fixed to Pd-Pd bridge (see Figure 4.21). The d-band center analysis

shows the reason behind the better binding ability of Pd clusters compared to the Pd/Au mixed structure: combining the effects of coordination, strain, and ligandic surroundings, the d-band center of the Pd clusters ends up closer to the Fermi energy, thus making stronger bonds to the adsorbates.

The correlation in Fig. 4.21 shows universality in a sense that the same plot incorporates data from the mixed Pd/Au structures, strained Pd(111) surface, and Pd clusters on top of Au(111). We have not come across studies where the d-band center would be related to binding properties over such a variety of different types of surfaces within a same graph. Our only points deviating from the otherwise linearly behaving data are the ones corresponding to the adsorption on Pd_{layer}/Au. In short, the full adlayer turns out to bind the molecules weaker than the position of the d-band center position suggests. The fact that the Pd(111) surface strained to the Au lattice dimensions binds the molecules with more or less with the same strength compared to the Pd_{layer}/Au(111), even though the d-band center of the latter is ∼0.3 eV higher, may be explained by the repulsive interaction between the adsorbates and the underlying Au. Similar explanation has been given for hydrogen adsorption trends over Pd_{layer}/Au(111) [119]. It does not, however, explain why the adsorption on Pd_7/Au structure is not weakened by the Au atoms to the same extent, and thus the reason for the somewhat anomalous behavior of Pd_{layer}/Au remains unknown.

Last we note, that varying the ensemble from the Pd-Pd bridge to Pd-Au bridge while maintaining the other effects constant leads to ∼0.6 eV weaker binding. This further supports the conclusion, that the active Pd/Au nanoparticles likely contain Pd clusters on top of Au. In mixed compositions the Pd atoms tend to be isolated between the gold atoms resulting in a reduction of needed Pd-Pd ensembles.

4.3.4 Underlying Au effect on reaction energetics

To test the effect of underlying gold on the catalytic performance of Pd, we calculated the activation energies for TCE HDC on Pd_7/Au(111). This structure manifests a good trade-off between the ability to bind TCE and offer sites for the reactants and products, and has been thus selected as a representative Pd/Au islet for the reactivity studies. According to our results, the surface structure does not affect the relative easiness of the elementary reactions, i.e. the overall reaction route over Pd (see chapter 4.2.2) can be expected to be independent of the presence of gold. However, as expected from the higher lying d-band of the Pd_7/Au(111), the mixed metal surface generally stabilizes the adsorbates and activated species more than the pure Pd surface throughout the whole HDC process. The stabilization is more pronounced for the transition states than for initial states resulting in a lower activation energies for Au containing surface. In fact, for some reactions the barriers differ notably for the two catalyst structures: The reactions CH-CCl* → C-CH* + Cl* and C-CH* + H* →

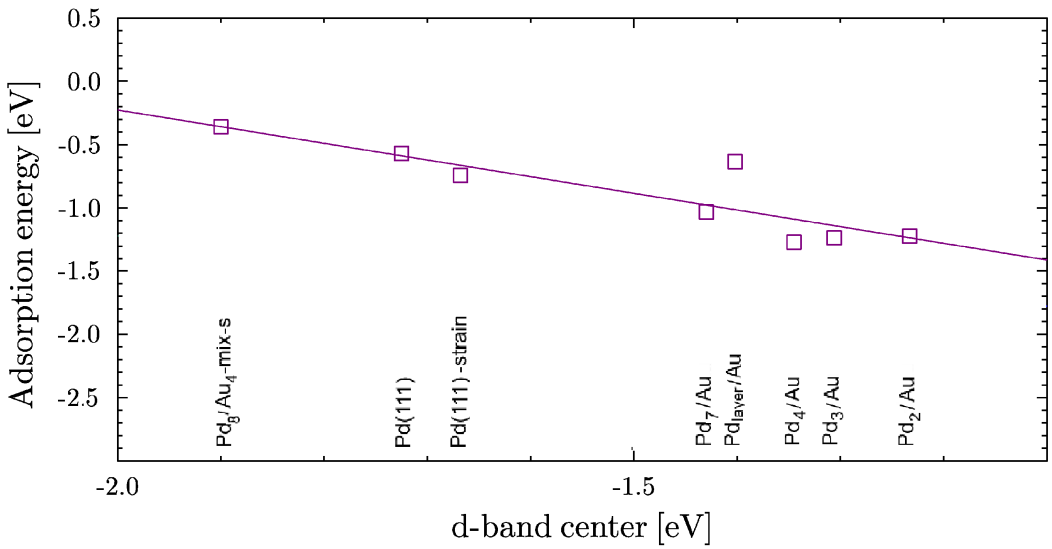

Figure 4.21: The adsorption energies of trichloroethene plotted against the d-band centers (relative to the Fermi energy) of the corresponding structures.

C-CH_2* need 0.30 eV less energy to activate on Pd_7/Au structure. These observations are in unison with the experimental studies reporting notable increase in reactivity of Pd when alloyed with Au [38, 39, 37].

5 Summary and outlook

In the work presented in this thesis, density functional theory calculations were carried out to study Pd-catalyzed decomposition of ethene and hydrodechlorination of trichloroethene. Our results shed light on probable reaction mechanisms and active structures for these reactions.

Our results show that under low coverage ethylene most likely undergoes hydrogenation-dehydrogenations to form ethylidyne on both flat and stepped Pd. The reaction proceeds via vinyl (or ethyl) and ethylidene intermediates where CH_2CH_2* $\rightarrow$ $CHCH_2$* + H* represents the rate-limiting step. The formation of ethylidyne is followed by a series of dehydrogenations toward -CCH species, that finally cleaves to produce atomic carbon. The activation barriers along the reaction coordinate increase from $\sim$1 eV to $\sim$1.5 eV. This agrees with the experimental findings that decompositions come into action sequentially with increasing temperature. Unlike on Ni, the steps do not introduce competition between C-H and C-C bond activation until the very end of the reaction coordinate. However, the step sites do bring down the barriers for activation thereby offering especially active sites for the reactions. Steps also facilitate the incorporation of carbon into the immediate subsurface area, from where the atoms move to decorate the step edges.

Trichloroethene hydrodechlorination mechanism was found to follow a direct pathway through radical-like species. This gives a potential explanation to the experimental product distributions that show a nominal amount of lesser chlorinated species in the presence of excess hydrogen. On a bare Pd(111) surface TCE is quickly dechlorinated to -CCH, which then hydrogenates to ethene via vinylidene and vinyl. The rate-determining step among surface reactions is identified as CCH_2*+H* $\rightarrow$ $CHCH_2$*, which activates with 0.83 eV energy input. The chlorine from the TCE decomposition can be expected to accumulate on the surface at low temperatures or in the absence of solvating water environment. Surface chlorine weakens the binding of the adsorbates and reduces the gap between the dechlorination and hydrogenation barriers. However, it is not expected to affect the overall reaction route. The entropy and zero-point energy corrected apparent activation energies explain the experimentally observed reactivity ordering among chlorinated ethenes. Although vinyl chlorine has a stronger C-Cl bond than TCE, it dechlorinates faster when introduced from the gas phase to the catalyst surface.

The active and resistant Pd/Au core-shell structures for room temperature TCE HDC

were identified as 2D Pd islands on Au nanoparticle. According to the formation energies, these structures are the most stable ones if no intermixing of Pd into the Au is allowed. Although the mixed structures are found energetically more favourable, they bind reactants poorly. Thus, the barriers for intermixing are presumably not crossed at room temperature, which is supported by several experimental studies. The Au(111) supported Pd island was calculated to offer more reactive ground for TCE HDC compared to pure Pd(111) in terms of activation barriers and reaction energies.

The data provided by the present work contribute to the evergrowing computational database needed in the search of better catalysts. On the other hand, the story concerning the studied reactions is not entirely written: the obtained figures are now available as input parameters for microkinetic reaction modeling, hopefully this will be addressed in future studies. As for ethylene decomposition, the effect of surface coke and dissolved carbon on the activity and selectivity of the surface reactions would be natural follow-up topics to the present work. Experiments implicate a variety of ways which carbonaceous surface species and subsurface carbon may contribute to the catalytic properties of the Pd surface, such as electronic structure modification and site blocking (see *e.g.* Refs. [6, 120]). What would also be very interesting to address is how varying the transition metal affects the selectivity of C-C and C-H bond as they break on defects. As we have seen now the ethylene dehydrogenation needs to proceed almost completely over stepped Pd before the two mechanisms start to compete whereas on stepped Ni they compete right from the beginning [103]. As concerns the hydrodechlorination of chlorinated ethenes in groundwater by Pd, there are still many open questions: Does the water phase play a role in the HDC process other than solvating the chlorine from the surface?; Why are Pd/Au structures more resistant toward poisoning by chloride and hydrosulfides [37] as compared to pure Pd?; Could the poorer performance of pure Pd owe to the oxidation of the metal that underlying Au would prevent, as suggested in a recent experimental work? [29]; *etc.* I believe using computational modeling can shed light on the above mentioned unresolved issues.

References

[1] G. Ertl. *Reactions at surfaces: From atoms to complexity (Nobel lecture).* Angew. Chem. Int. Ed. **47**, 3524 (2008).

[2] R.I. Masel. *Principles of adsorption and reaction on solid surface.* John Wiley & Sons, Inc. (1996).

[3] K.W. Kolasinski. *Surface Science - Foundations of Catalysis and Nanoscience.* John Wiley & Sons Ltd (2002).

[4] K. Honkala, A. Hellman, I.N. Remediakis, A. Logadottir, A. Carlsson, S. Dahl, C.H. Christensen and J.K. Nørskov. *Ammonia Synthesis from First-Principles Calculations.* Science **307**, 555 (2005).

[5] W. Kohn. *Nobel Lecture: Electronic structure of matter-wave functions and density functionals.* Rev. Mod. Phys. **71**, 1253 (1999).

[6] E.M. Vass, M. Hävecker, S. Zafeiratos, D. Teschner, A. Knop-Gericke and R. Schlögl. *The role of carbon species in heterogeneous catalytic processes: an in situ soft x-ray photoelectron spectroscopy study.* J. Phys.:Condens. Matter **20**, 184016 (2008).

[7] T.P. Beebe and J.T. Yates. *An in situ infrared spectroscopic investigation of the role of ethylidyne in the ethylene hydrogenation reaction on palladium/alumina.* J. Am. Chem. Soc. **108**, 663 (1986).

[8] D. Stacchiola, F. Calaza, T. Zheng and W.T. Tysoe. *Hydrocarbon conversion on palladium catalysts.* J. Mol. Catal. A **228**, 35 (2005).

[9] M. Sock, A. Eichler, S. Surnev, J.N. Andersen, B. Klötzer, K. Hayek, M.G. Ramsey and F.P. Netzer. *High-resolution electron spectroscopy of different adsorption states of ethylene on Pd(111).* Surf. Sci. **545**, 122 (2003).

[10] H. Gabasch, K. Hayek, B. Klötzer, A. Knop-Gericke and R. Schlögl. *Carbon Incorporation in Pd(111) by Adsorption and Dehydrogenation of Ethene.* J. Phys. Chem. B **110**, 4947 (2006).

[11] L.P. Wang, W.T. Tysoe, R.M. Ormerod, R.M. Lambert, H. Hoffmann and F. Zaera. *Determination of the Bonding and Orientation of Ethylene on Pd(111) by Near-Edge X-ray Absorption Fine Structure and Photoelectron Spectroscopy.* J. Phys. Chem. **94**, 4236 (1990).

[12] J.A. Gates and L.L. Kesmodel. *EELS analysis of the low temperature phase of ethylene chemisorbed on Pd(111).* Surf. Sci. **120** (1982).

[13] D. Stacchiola, L. Burkholder and W.T. Tysoe. *Ethylene at Pd.* Surf. Sci. **511**, 215 (2002).

[14] V. Pallassana, M. Neurock, V.S. Lusvardi, J.J. Lerou, D.D. Kragten and R.A. van Santen. *A density functional theory analysis of the reaction pathways and intermediates for ethylene dehydrogenation over Pd(111).* J. Phys. Chem. B **106**, 1656 (2002).

[15] F. Mittendorfer, C. Thomazeau, P. Raybaud and H.Toulhoat. *Adsorption of unsaturated hydrocarbons on Pd(111) and Pt(111): A DFT study.* J. Phys. Chem. B **107**, 12287 (2003).

[16] Q. Ge and M. Neurock. *Correlation of adsorption energy with surface structure: ethylene adsorption on Pd surfaces.* Chem. Phys. Lett. **358**, 377 (2002).

[17] L.V. Moskaleva, Z-X. Chen, H.A. Aleksandrov, A.B. Mohammed, Q. Sun and N. Rösch. *Ethylene conversion to ethylidyne over Pd(111): revisiting the mechanism with first-principles calculations.* J. Phys. Chem. C **113**, 2512 (2009).

[18] Z.-X. Chen, H.A. Aleksandrov, D. Basaran and N. Rösch. *Transformations of Ethylene on the Pd(111) Surface: A Density Functional Study.* J. Phys. Chem. C **114**, 17683 (2010).

[19] *Trichloroethene in Drinking-water*, Background document for development of "WHO Guidelines for Drinking-water Quality", World Health Organization, (2005).

[20] G.V. Lowry and M. Reinhard. *Hydrodehalogenation of 1- to 3-Carbon Halogenated Organic Compounds in Water Using a Palladium Catalyst and Hydrogen Gas.* Environ. Sci. Technol. **33**, 1905 (1999).

[21] G.V. Lowry and M. Reinhard. *Pd-Catalyzed TCE Dechlorination in Wateer: Effect of [H2](aq) and H2-Utilizing Competitive Solutes on the TCE Dechlorination Rate and Product Distribution.* Environ. Sci. Technol. **35**, 696 (2001).

[22] C.G. Schreier and M. Reinhard. *Catalytic hydrodehalogenation of chlorinated ethylenes using palladium and hydrogen for the treatment of contaminated water.* Chemosphere **31**, 3475 (1995).

[23] F.D. Kopinke, K. Mackenzie and R. Köhler. *Catalytic hydrodechlorination of groundwater contaminants in water and in the gas phase using* Pd/γ-Al_2O_3. Appl. Catal. B **44**, 15 (2003).

[24] K. Mackenzie, H. Frenzel and F.D. Kopinke. *Hydrodehalogenation of halogenated hydrocarbons in water with Pd catalysts: Reaction rates and surface competition.* Appl. Catal. B Env. **63**, 161 (2006).

[25] H. Hildebrand, K. Mackenzie and F.D. Kopinke. *Pd/Fe_3O_4 nano-catalysts for selective dehalogenation in wastewater treatment processes-Influence of water constituents.* Appl. Cat. B **91**, 389 (2009).

[26] M.G. Davie, H. Cheng, G.D. Hopkins, C.A. Lebron and M. Reinhard. *Implementing Heterogeneous Catalytic Dechlorination Technology for Remediating TCE-Contaminated Groundwater.* Environ. Sci. Technol. **42**, 8908 (2008).

[27] Y.-H. Kim and E.R. Carraway. *Dechlorination of chlorinated ethenes and acetylenes by palladized iron.* Environ. Technol. **24**, 809 (2003).

[28] S. Ordóñez, H. Sastre and F.V. Díez. *Hydrodechlorination of aliphatic organochlorinated compounds over commercial hydrogenation catalysts.* Appl. Catal., B **25**, 49 (2000).

[29] Y.-L. Fang, K.N. Heck, P.J.J. Alvarez and M.S. Wong. *Kinetics Analysis of Palladium/Gold Nanoparticles as Colloidal Hydrodechlorination Catalysts.* ACS Catal. **1**, 128 (2011).

[30] S. Ordóñez, F.V. Díez and H. Sastre. *Catalytic hydrodechlorination of chlorinated olefins.* Ind. Eng. Chem. Res. **41**, 505 (2002).

[31] F.J. Urbano and J.M. Marinas. *Hydrogenolysis of organohalogen compounds over palladium supported catalysts.* J. Mol. Catal. A **173**, 329 (2001).

[32] J. Sepulveda and N. Figoli. *Effect of residual chlorine on the activity of Pd/SiO_2 catalysts during the selective hydrogenation of styrene.* React. Kinet. Catal. Lett. **53**, 155 (1994).

[33] J.L. Benitez and G. Del Angel. *Effect of chlorine released during hydrodechlorination of chlorobenzene over Pd, Pt and Rh supported catalysts.* React. Kinet. Catal. Lett. **70**, 67 (2000).

[34] S. Ordóñez, B.P. Vivas and F.V. Díez. *Minimization of the deactivation of palladium catalysts in the hydrodechlorination of trichloroethylene in wastewaters.* Appl. Catal., B **95**, 288 (2010).

[35] F.D. Kopinke, K. Mackenzie and R. Köhler. *Catalytic hydrodechlorination of groundwater contaminants in water and in the gas phase using Pd/ γ-Al_2O_3.* Appl. Catal. B **44**, 15 (2003).

[36] V.I. Simagina, E.S. Tayban, E.D. Grayfer, A.G. Gentsler, O.V. Komova and O.V. Netskina. *Liquid-phase hydrodechlorination of chlorobenzene by molecular hydrogen: The influence of reaction medium on process efficiency.* Pure Appl. Chem. **81**, 2107 (2009).

[37] K.N. Heck, M.O. Nutt, P. Alvarez and M.S. Wong. *Deactivation resistance of Pd/Au nanoparticle catalysts for water-phase hydrodechlorination.* J. Catal. **267**, 97 (2009).

[38] M.O. Nutt, J.B. Hughes and M.S. Wong. *Designing Pd-on-Au Bimetallic Nanoparticle Catalysts for Trichloroethene Hydrodechlorination.* Environ. Sci. Technol. **39**, 1346 (2005).

[39] M.O. Nutt, K.N. Heck, P. Alvarez and M.S. Wong. *Improved Pd-on-Au bimetallic nanoparticle catalysts for aqueous-phase trichloroethene hydrodechlorination.* Appl. Catal. B **69**, 115 (2006).

[40] B. Hammer and J.K. Nørskov. *Electronic factors determining the reactivity of metal surfaces.* Surf. Sci. **343**, 211 (1995).

[41] F. Abild-Pedersen, J. Greeley and J.K. Nørskov. *Understanding the effect of steps, strain, poisons, and alloying: Methane activation on Ni surfaces.* Catal. Lett. **105**, 9 (2005).

[42] B. Hammer and J.K. Nørskov. *Chemisorption and Reactivity on Supported clusters and Thin Films*, chapter Theory of Adsorption and Surface Reactions, 285–351. Kluwer Academic Publishers (1997).

[43] M. Gsell, P. Jakob and D. Menzel. *Effect of substrate strain on adsorption.* Science **280**, 717 (1998).

[44] M. Mavrikakis, B. Hammer and J.K. Nørskov. *Effect of strain on the reactivity of metal surfaces.* Phys. Rev. Lett. **81**, 2819 (1998).

[45] A. Schlapka, M. Lischka, A. Groß, U. Käsberger and P. Jakob. *Surface strain versus substrate interaction in heteroepitaxial metal layers: Pt on Ru(0001).* Phys. Rev. Lett. **91**, 016101 (2003).

[46] A. Roudgar and A. Groß. *Local reactivity of metal overlayers: Density functional theory calculations of Pd on Au.* Phys. Rev. B **67**, 033409 (2003).

[47] A. Roudgar and A. Groß. *Local reactivity of supported metal clusters: Pd_n on Au(111).* Surf. Sci. **559** (2004).

[48] S. Schnur and A. Groß. *Strain and coordination effects in the adsorption properties of early transition metals.* Phys. Rev. B **81**, 033402 (2010).

[49] R. Ferrando, J. Jellinek and R.L. Johnston. *Nanoalloys: From Theory to Applications of Alloy Clusters and Nanoparticles.* Chem. Rev. **108**, 845 (2008).

[50] J.G. Chen, C.A. Menning and M.B. Zellner. *Monolayer bimetallic surfaces: Experimental and theoretical studies of trends in electronic and chemical properties.* Surf. Sci. Rep. **63**, 201 (2008).

[51] A. Groß. *Reactivity of bimetallic systems studied from first principles.* Top. Catal. **37**, 29 (2006).

[52] J.W.A. Sachtler and G.A. Somorjai. *Influence of ensemble size on CO chemisorption and catalytic n-hexane conversion by Au-Pt(111) bimetallic single-crystal surfaces.* J. Catal. **81**, 77 (1983).

[53] P. Liu and J.K. Nørskov. *Ligand and ensemble effects in adsorption on alloy surfaces.* Phys. Chem. Chem. Phys. **3**, 3814 (2001).

[54] C. Jaffé, D. Farrelly and T. Uzer. *Transition state in atomic physics.* Phys. Rev. A **60**, 3833 (1999).

[55] H. Eyring. *The Activated Complex in Chemical Reactions.* J. Chem. Phys. **3**, 107 (1934).

[56] P. Hänggi, P. Talkner and M. Borkovec. *Reaction-rate theory: fifty years after Kramers.* Rev. Mod. Phys. **62**, 251 (1990).

[57] H. Jønsson. *Thermodynamics and Introduction to Statistical Mechanics.* Course material, University of Iceland (2009).

[58] K.J. Laidler and M.C. King. *The Development of Transition-State Theory.* J. Phys. Chem. **87**, 2657 (1983).

[59] R.A. Van Santen and H.J.W. Niemantsverdriet. *Chemical kinetics and catalysis.* Springer (1995).

[60] J.N. Brønsted. *Acid and Basic Catalysis.* Chem. Rev. **5**, 231 (1928).

[61] M.G. Evans and M. Polanyi. *Inertia and Driving Force of Chemical Reactions.* Trans. Faraday Soc. **34**, 11 (1938).

[62] J.K. Nørskov, T. Bligaard, A. Logadottir, S. Bahn, L.B. Hansen, M. Bollinger, H. Bengaard, B. Hammer, Z. Sljivancanin, M. Mavrikakis, Y. Xu, S. Dahl and C.J.H. Jacobsen. *Universality in Heterogeneous Catalysis.* J. Catal. **209**, 275 (2002).

[63] S. Wang, B. Temel, J. Shen, G. Jones, L.C. Grabow, F. Studt, T. Bligaard, F. Abild-Pedersen, C.H. Christensen and J.K. Nørskov. *Universal Brønsted-Evans-Polanyi Relations for C-C, C-O, C-N, N-O, N-N, and O-O Dissociation Reactions.* Catal. Lett. **141**, 370 (2011).

[64] A. Logadottir, T.H. Rod and J.K. Nørskov and B. Hammer and S. Dahl and C.J.H. Jacobsen. *The Brønsted-Evans-Polanyi Relation and the Volcano Plot for Ammonia Synthesis over Transition Metal Catalysts.* J. Catal. **197**, 229 (2001).

[65] S. Dahl, A. Logadottir, R.C. Egeberg, J.H. Larsen and I. Chorkendorff. *Role of Steps in N_2 Activation on Ru(0001).* Phys. Rev. Lett. **83**, 1814 (1999).

[66] F. Abild-Pedersen, J. Greeley, F. Studt, J. Rossmeisl, T.R. Munter, P.G. Moses, E. Skulason, T. Bligaard and J.K. Nørskov. *Scaling properties of adsorption energies for hydrogen-containing molecules on transition-metal surfaces.* Phys. Rev. Lett. **99**, 016105 (2007).

[67] G. Jones, T. Bligaard, F. Abild-Pedersen and J.K. Nørskov. *Using scaling relations to understand trends in the catalytic activity of transition metals.* J. Phys. Condens. Matter **20**, 064239 (2008).

[68] F. Studt, F. Abild-Pedersen, T. Bligaard, R.Z. Sørensen, C.H. Christensen and J.K. Nørskov. *Identification of non-precious metal alloy catalysts for selective hydrogenation of acetylene.* Science **320**, 1320 (2008).

[69] G. Jones, T. Bligaard, F. Abild-Pedersen and J.K. Nørskov. *Modeling Ethanol Decomposition on Transition Metals: A Combined Application of Scaling and Brønsted-Evans-Polanyi Relations.* J. Am. Chem. Soc. **131**, 5809 (2009).

[70] G.A. Somorjai and M. Yang. *The surface science of catalytic selectivity.* Top. Catal. **24**, 61 (2003).

[71] T. Bligaard, J.K. Nørskov, S. Dahl, J. Matthiesen, C.H. Christensen and J. Sehested. *The Brønsted-Evans-Polanyi relation and the volcano curve in heterogeneous catalysis.* J. Catal. **224**, 206 (2004).

[72] R. M. Martin. *Electronic structure - Basic theory and practical methods.* Cambridge university press, UK (2004).

[73] R. van Leeuwen. *Density functional theory and its applications in nanoscience.* Lecture notes, University of Jyväskylä (2008).

[74] J.P. Perdew and S. Kurth. *Density functionals for non-relativistic coulomb systems.* Lect. Notes in Phys., Springer, Germany **500**, 8 (1998).

[75] U. von Barth. *Basic density-functional theory - an overview.* Physica Scripta **109**, 9 (2004).

[76] P. Hohenberg and W. Kohn. *Inhomogeneous electron gas.* Phys. Rev. **136**, 864 (1964).

[77] W. Kohn and L.J. Sham. *Self-consistent equations including exchange and correlation effects.* Phys. Rev. **140**, 1133 (1965).

[78] W. Kohn and L.J. Sham. *Self-consistent equations including exchange and correlation effects.* Phys. Rev. Lett. **140**, 1133 (1965).

[79] J.P. Perdew and K. Schmidt. *AIP Conference Proceedings 577, edited by V.E. Van Doren, C. Van Alsenoy, and P. Geerlings*, chapter Density Functional Theory and Its Applications to Materials. The American Institute of Physics (2001).

[80] J.P. Perdew, K. Burke and M. Ernzerhof. *Generalized gradient approximation made simple.* Phys. Rev. Lett. **77**, 3865 (1996).

[81] B. Hammer, L.B. Hansen and J.K. Nørskov. *Improved adsorption energetics within density-functional theory using revised Perdew-Burke-Ernzerhof functionals.* Phys. Rev. B. **59**, 7413 (1999).

[82] N. Troullier and J.L. Martins. *Efficient pseudopotentials for plane wave calculations.* Phys. Rev. B **43**, 1993 (1991).

[83] B. Meyer. *Computational Nanoscience: Do It Yourself!, J. Grotendorst, S. Blügel, D. Marx (Eds.)*, chapter The Pseudopotential Plane Wave Approach, Vol. 31, p. 71-83. John von Neumann Institute for Computing, Jülich, NIC series (2006).

[84] P.E. Blöchl. *Projector augmented-wave method.* Phys. Rev. B **50**, 17953 (1994).

[85] P.E. Blöchl, C.J. Först and J. Schimpl. *Projector augmented wave method: ab-initio molecular dynamics with full wave functions.* Bull. Mat. Sci. **26**, 33 (2003).

[86] G. Kresse and D. Joubert. *From ultrasoft pseudopotentials to the projector augmented-wave method.* Phys. Rev. B **59**, 1758 (1999).

[87] Http://dcwww.camd.dtu.dk/campos/Dacapo/.

[88] J.J. Mortensen, L.B. Hansen and K.W. Jacobsen. *Real-space grid implementation of the projector augmented wave method.* Phys. Rev. B **71**, 035109 (2005). Https://wiki.fysik.dtu.dk/gpaw/.

[89] J. Enkovaara *et al. Electronic structure calculations with GPAW: a real-space implementation of the projector augmented-wave method.* J. Phys.: Condens. Matter **22**, 253202 (2010).

[90] F. Bloch. *Über die Quantenmechanik der Elektronen in Kristallgittern.* Z. Phys. **52**, 555 (1928).

[91] H.J. Monkhorst and J.D. Pack. *Special points for Brillouin-zone integrations.* Phys. Rev. B **13**, 5188 (1976).

[92] D. Vanderbilt. *Soft self-consistent pseudopotentials in a generalized eigenvalue formalism.* Phys. Rev. B **41**, 7892 (1990).

[93] Https://wiki.fysik.dtu.dk/ase/.

[94] R. Fletcher. *Practical Methods of Optimization.* John Wiley & Sons (1987).

[95] H. Jónsson, G. Mills and K.W. Jacobsen. *Classical and Quantum Dynamics in Condensed Phase Simulations, B.J. Berne, G. Ciccotti, D.F. Coker (Eds.)*, chapter Nudged elastic band method for finding minimum energy paths of transitions. World Scientific, Singapore (1998).

[96] G. Mills and H. Jónsson. *Quantum and Thermal Effects in H2 Dissociative Adsorption - Evaluation of Free-Energy Barriers in Multidimensional Quantum-Systems.* Phys. Rev. Lett. **72**, 1124 (1994).

[97] G. Mills, H. Jónsson and G. Schenter. *Reversible Work Transition-State Theory - Application to Dissociative Adsorption of Hydrogen.* Surf. Sci. **324**, 305 (1995).

[98] G. Henkelman, B.P. Uberuaga and H. Jónsson. *A climbing image nudged elastic band method for finding saddle points and minimum energy paths.* J. Chem. Phys. **113**, 9901 (2000).

[99] P. Maragakis, S.A. Andreev, Y. Brumer, D.R. Reichman and E. Kaxiras. *Adaptive nudged elastic band approach for transition state calculation.* J. Chem. Phys. **117**, 4651 (2002).

[100] W.T. Tysoe, G.L. Nyberg and R.M. Lambert. *Structural, Kinetic, and Reactive Properties of the Palladium(111)-Ethylene System.* J. Phys. Chem. **88**, 1960 (1984).

[101] A. Vojvodic. *Reactivity of Transition-Metal Compounds from Electronic Structure.* Chalmers University of Technology, Göteborg, Sweden (2009).

[102] D. Stacchiola and W.T. Tysoe. *The Kinetics of Ethylidyne Formation from Ethylene on Pd(111).* J. Phys. Chem. C **113**, 8000 (2009).

[103] R.T. Vang, K. Honkala, S. Dahl, E.K. Vestergaard, J. Schnadt, E. Lægsgaard, B.S. Clausen, J.K. Nørskov and F. Besenbacher. *Controlling the catalytic bond-breaking selectivity of Ni surfaces by step blocking.* Nat. Mater. **4**, 160 (2005).

[104] I. Jungwirthova and L.L. Kesmodel. *Thermal Evolution of Acetylene Overlayers on Pd(111).* J. Phys. Chem. B **105**, 674 (2001).

[105] M. Li, W. Guo, R. Jiang, L. Zhao and H. Shan. *Decomposition of Ethanol on Pd(111): A Density Functional Theory Study.* Langmuir **26**, 1879 (2009).

[106] H.-F. Wang and Z.-P. Liu. *Comprehensive Mechanism and Structure-Sensitivity of Ethanol Oxidation on Platinum: New Transition-State Searching Method for Resolving the Complex Reaction Network.* J. Am. Chem. Soc. **130**, 10996 (2008).

[107] D.E. Hunka, D.C. Herman, L.I. Lopez, K.D. Lormand and D.P. Land. *The Adsorption and Reaction of HCl on Pd(111).* J. Phys. Chem. **105**, 4973 (2001).

[108] M.A. Henderson. *The interaction of water with solid surfaces: fundamental aspects revisited.* Surf. Sci. Rep. **46**, 1 (2002).

[109] B.N. Zope, D.D. Hibbitts, M. Neurock and R.J. Davis. *Reactivity of the Gold/Water Interface During Selective Oxidation Catalysis.* Science **330**, 74 (2010).

[110] M. Calatayud, D. Courmier and C. Minot. *Ionization of HCl and HF in ice: a periodic DFT study.* Chem. Phys. Lett. **369**, 287 (2003).

[111] P. Parkkinen. *Veden vaikutus trikloorieteenin hydrodeklorinaatioon osallistuvien yhdisteiden adsorptioon Pd(111)- ja Pd7/Au(111)-pinnoilla.* University of Jyväskylä, Finland (2011).

[112] A.G. Shard, V.R. Dhanak and A. Santoni. *Structures of chlorine on palladium (111).* Surf. Sci. **445**, 309 (2000).

[113] Computational Chemistry Comparison and Benchmark Database, National Institute of Standards and Technology, U.S. Department of Commerce, 2010.

[114] D.W. Blaylock, T. Ogura, W.H. Green and G.J.O. Beran. *Computational Investigation of Thermochemistry and Kinetics of Steam Methane Reforming on Ni(111) under Realistic Conditions.* J. Phys. Chem. C **113**, 4898 (2009).

[115] K.N. Heck, B.G. Janesko, G.E. Scuseria, N.J. Halas and M.S. Wong. *Observing Metal-Catalyzed Chemical Reactions in Situ Using Surface-Enhanced Raman Spectroscopy on Pd-Au Nanoshells.* J. Am. Chem. Soc **130**, 16592 (2008).

[116] A.W. Stephenson, C.J. Baddeley, M.S. Tikhov and R.M. Lambert. *Nucleation and growth of catalytically active Pd islands on Au(111)-22 x* $\sqrt{3}$ *studied by scanning tunnelling microscopy.* Surf. Sci. **398**, 172 (1998).

[117] A.E. Baber, H.L. Tierney and E.C.H. Sykes. *Atomic-Scale Geometry and Electronic Structure of Catalytically Important Pd/Au Alloys.* ACS Nano **4**, 1637 (2010).

[118] C.S. Casari, S. Foglio, F. Siviero, A. Li Bassi, M. Passoni and C.E. Bottani. *Direct observation of the basic mechanisms of Pd island nucleation on Au(111).* Phys. Rev. B **79**, 195402 (2009).

[119] A. Roudgar and A. Groß. *Local reactivity of thin Pd overlayers on Au single crystals.* J. Electroanal. Chem. **548**, 121 (2003).

[120] Sh.K. Shaikhutdinov, M. Frank, M. Bäumer, S.D. Jackson, R.J. Oldman, J.C. Hemminger and H.-J. Freund. *Effect of carbon deposits on reactivity of supported Pd model catalysts.* Cat. Lett. **80**, 115 (2002).

DEPARTMENT OF CHEMISTRY, UNIVERSITY OF JYVÄSKYLÄ

RESEARCH REPORT SERIES

1. Vuolle, Mikko: Electron paramagnetic resonance and molecular orbital study of radical ions generated from (2.2)metacyclophane, pyrene and its hydrogenated compounds by alkali metal reduction and by thallium(III)trifluoroacetate oxidation. (99 pp.) 1976
2. Pasanen, Kaija: Electron paramagnetic resonance study of cation radical generated from various chlorinated biphenyls. (66 pp.) 1977
3. Carbon-13 Workshop, September 6-8, 1977. (91 pp.) 1977
4. Laihia, Katri: On the structure determination of norbornane polyols by NMR spectroscopy. (111 pp.) 1979
5. Nyrönen, Timo: On the EPR, ENDOR and visible absorption spectra of some nitrogen containing heterocyclic compounds in liquid ammonia. (76 pp.) 1978
6. Talvitie, Antti: Structure determination of some sesquiterpenoids by shift reagent NMR. (54 pp.) 1979
7. Häkli, Harri: Structure analysis and molecular dynamics of cyclic compounds by shift reagent NMR. (48 pp.) 1979
8. Pitkänen, Ilkka: Thermodynamics of complexation of 1,2,4-triazole with divalent manganese, cobalt, nickel, copper, zinc, cadmium and lead ions in aqueous sodium perchlorate solutions. (89 pp.) 1980
9. Asunta, Tuula: Preparation and characterization of new organometallic compounds synthesized by using metal vapours. (91 pp.) 1980
10. Sattar, Mohammad Abdus: Analyses of MCPA and its metabolites in soil. (57 pp.) 1980
11. Bibliography 1980. (31 pp.) 1981
12. Knuuttila, Pekka: X-Ray structural studies on some divalent 3d metal compounds of picolinic and isonicotinic acid N-oxides. (77 pp.) 1981
13. Bibliography 1981. (33 pp.) 1982
14. 6th National NMR Symposium, September 9-10, 1982, Abstracts. (49 pp.) 1982
15. Bibliography 1982. (38 pp.) 1983
16. Knuuttila, Hilkka: X-Ray structural studies on some Cu(II), Co(II) and Ni(II) complexes with nicotinic and isonicotinic acid N-oxides. (54 pp.) 1983
17. Symposium on inorganic and analytical chemistry, May 18, 1984, Program and Abstracts. (100 pp.) 1984
18. Knuutinen, Juha: On the synthesis, structure verification and gas chromatographic determination of chlorinated catechols and guaiacols occuring in spent bleach liquors of kraft pulp mill. (30 pp.) 1984
19. Bibliography 1983. (47 pp.) 1984

20. Pitkänen, Maija: Addition of BrCl, B_2 and Cl_2 to methyl esters of propenoic and 2-butenoic acid derivatives and ^{13}C NMR studies on methyl esters of saturated aliphatic mono- and dichlorocarboxylic acids. (56 pp.) 1985

21. Bibliography 1984. (39 pp.) 1985

22. Salo, Esa: EPR, ENDOR and TRIPLE spectroscopy of some nitrogen heteroaromatics in liquid ammonia. (111 pp.) 1985

23. Humppi, Tarmo: Synthesis, identification and analysis of dimeric impurities of chlorophenols. (39 pp.) 1985

24. Aho, Martti: The ion exchange and adsorption properties of sphagnum peat under acid conditions. (90 pp.) 1985

25. Bibliography 1985 (61 pp.) 1986

26. Bibliography 1986. (23 pp.) 1987

27. Bibliography 1987. (26 pp.) 1988

28. Paasivirta, Jaakko (Ed.): Structures of organic environmental chemicals. (67 pp.) 1988

29. Paasivirta, Jaakko (Ed.): Chemistry and ecology of organo-element compounds. (93 pp.) 1989

30. Sinkkonen, Seija: Determination of crude oil alkylated dibenzothiophenes in environment. (35 pp.) 1989

31. Kolehmainen, Erkki (Ed.): XII National NMR Symposium Program and Abstracts. (75 pp.) 1989

32. Kuokkanen, Tauno: Chlorocymenes and Chlorocymenenes: Persistent chlorocompounds in spent bleach liquors of kraft pulp mills. (40 pp.) 1989

33. Mäkelä, Reijo: ESR, ENDOR and TRIPLE resonance study on substituted 9,10-anthraquinone radicals in solution. (35 pp.) 1990

34. Veijanen, Anja: An integrated sensory and analytical method for identification of off-flavour compounds. (70 pp.) 1990

35. Kasa, Seppo: EPR, ENDOR and TRIPLE resonance and molecular orbital studies on a substitution reaction of anthracene induced by thallium(III) in two fluorinated carboxylic acids. (114 pp.) 1990

36. Herve, Sirpa: Mussel incubation method for monitoring organochlorine compounds in freshwater recipients of pulp and paper industry. (145 pp.) 1991

37. Pohjola, Pekka: The electron paramagnetic resonance method for characterization of Finnish peat types and iron (III) complexes in the process of peat decomposition. (77 pp.) 1991

38. Paasivirta, Jaakko (Ed.): Organochlorines from pulp mills and other sources. Research methodology studies 1988-91. (120 pp.) 1992

39. Veijanen, Anja (Ed.): VI National Symposium on Mass Spectrometry, May 13-15, 1992, Abstracts. (55 pp.) 1992

40. Rissanen, Kari (Ed.): The 7. National Symposium on Inorganic and Analytical Chemistry, May 22, 1992, Abstracts and Program. (153 pp.) 1992

41. Paasivirta, Jaakko (Ed.): CEOEC'92, Second Finnish-Russian Seminar: Chemistry and Ecology of Organo-Element Compounds. (93 pp.) 1992

42. Koistinen, Jaana: Persistent polychloroaromatic compounds in the environment: structure-specific analyses. (50 pp.) 1993

43. Virkki, Liisa: Structural characterization of chlorolignins by spectroscopic and liquid chromatographic methods and a comparison with humic substances. (62 pp.) 1993

44. Helenius, Vesa: Electronic and vibrational excitations in some biologically relevant molecules. (30 pp.) 1993

45. Leppä-aho, Jaakko: Thermal behaviour, infrared spectra and x-ray structures of some new rare earth chromates(VI). (64 pp.) 1994

46. Kotila, Sirpa: Synthesis, structure and thermal behavior of solid copper(II) complexes of 2-amino-2- hydroxymethyl-1,3-propanediol. (111 pp.) 1994

47. Mikkonen, Anneli: Retention of molybdenum(VI), vanadium(V) and tungsten(VI) by kaolin and three Finnish mineral soils. (90 pp.) 1995

48. Suontamo, Reijo: Molecular orbital studies of small molecules containing sulfur and selenium. (42 pp.) 1995

49. Hämäläinen, Jouni: Effect of fuel composition on the conversion of fuel-N to nitrogen oxides in the combustion of small single particles. (50 pp.) 1995

50. Nevalainen, Tapio: Polychlorinated diphenyl ethers: synthesis, NMR spectroscopy, structural properties, and estimated toxicity. (76 pp.) 1995

51. Aittola, Jussi-Pekka: Organochloro compounds in the stack emission. (35 pp.) 1995

52. Harju, Timo: Ultrafast polar molecular photophysics of (dibenzylmethine)borondifluoride and 4-aminophthalimide in solution. (61 pp.) 1995

53. Maatela, Paula: Determination of organically bound chlorine in industrial and environmental samples. (83 pp.) 1995

54. Paasivirta, Jaakko (Ed.): CEOEC'95, Third Finnish-Russian Seminar: Chemistry and Ecology of Organo-Element Compounds. (109 pp.) 1995

55. Huuskonen, Juhani: Synthesis and structural studies of some supramolecular compounds. (54 pp.) 1995

56. Palm, Helena: Fate of chlorophenols and their derivatives in sawmill soil and pulp mill recipient environments. (52 pp.) 1995

57. Rantio, Tiina: Chlorohydrocarbons in pulp mill effluents and their fate in the environment. (89 pp.) 1997

58. Ratilainen, Jari: Covalent and non-covalent interactions in molecular recognition. (37 pp.) 1997

59. Kolehmainen, Erkki (Ed.): XIX National NMR Symposium, June 4-6, 1997, Abstracts. (89 pp.) 1997

60. Matilainen, Rose: Development of methods for fertilizer analysis by inductively coupled plasma atomic emission spectrometry. (41 pp.) 1997

61. Koistinen, Jari (Ed.): Spring Meeting on the Division of Synthetic Chemistry, May 15-16, 1997, Program and Abstracts. (36 pp.) 1997

62. Lappalainen, Kari: Monomeric and cyclic bile acid derivatives: syntheses, NMR spectroscopy and molecular recognition properties. (50 pp.) 1997

63. Laitinen, Eira: Molecular dynamics of cyanine dyes and phthalimides in solution: picosecond laser studies. (62 pp.) 1997

64. Eloranta, Jussi: Experimental and theoretical studies on some quinone and quinol radicals. (40 pp.) 1997

65. Oksanen, Jari: Spectroscopic characterization of some monomeric and aggregated chlorophylls. (43 pp.) 1998

66. Häkkänen, Heikki: Development of a method based on laser-induced plasma spectrometry for rapid spatial analysis of material distributions in paper coatings. (60 pp.) 1998

67. Virtapohja, Janne: Fate of chelating agents used in the pulp and paper industries. (58 pp.) 1998

68. Airola, Karri: X-ray structural studies of supramolecular and organic compounds. (39 pp.) 1998

69. Hyötyläinen, Juha: Transport of lignin–type compounds in the receiving waters of pulp mills. (40 pp.) 1999

70. Ristolainen, Matti: Analysis of the organic material dissolved during totally chlorine-free bleaching. (40 pp.) 1999

71. Eklin, Tero: Development of analytical procedures with industrial samples for atomic emission and atomic absorption spectrometry. (43 pp.) 1999

72. Välisaari, Jouni: Hygiene properties of resol-type phenolic resin laminates. (129 pp.) 1999

73. Hu, Jiwei: Persistent polyhalogenated diphenyl ethers: model compounds syntheses, characterization and molecular orbital studies. (59 pp.) 1999

74. Malkavaara, Petteri: Chemometric adaptations in wood processing chemistry. (56 pp.) 2000

75. Kujala Elena, Laihia Katri, Nieminen Kari (Eds.): NBC 2000, Symposium on Nuclear, Biological and Chemical Threats in the 21st Century. (299 pp.) 2000

76. Rantalainen, Anna-Lea: Semipermeable membrane devices in monitoring persistent organic pollutants in the environment. (58 pp.) 2000

77. Lahtinen, Manu: *In situ* X-ray powder diffraction studies of Pt/C, CuCl/C and Cu_2O/C catalysts at elevated temperatures in various reaction conditions. (92 pp.) 2000

78. Tamminen, Jari: Syntheses, empirical and theoretical characterization, and metal cation complexation of bile acid-based monomers and open/closed dimers. (54 pp.) 2000

79. Vatanen, Virpi: Experimental studies by EPR and theoretical studies by DFT calculations of α-amino-9,10-anthraquinone radical anions and cations in solution. (37 pp.) 2000

80. Kotilainen, Risto: Chemical changes in wood during heating at 150-260 °C. (57 pp.) 2000

81. Nissinen, Maija: X-ray structural studies on weak, non-covalent interactions in supramolecular compounds. (69 pp.) 2001

82. Wegelius, Elina: X-ray structural studies on self-assembled hydrogen-bonded networks and metallosupramolecular complexes. (84 pp.) 2001

83. Paasivirta, Jaakko (Ed.): CEOEC'2001, Fifth Finnish-Russian Seminar: Chemistry and Ecology of Organo-Element Compounds. (163 pp.) 2001

84. Kiljunen, Toni: Theoretical studies on spectroscopy and atomic dynamics in rare gas solids. (56 pp.) 2001

85. Du, Jin: Derivatives of dextran: synthesis and applications in oncology. (48 pp.) 2001

86. Koivisto, Jari: Structural analysis of selected polychlorinated persistent organic pollutants (POPs) and related compounds. (88 pp.) 2001

87. Feng, Zhinan: Alkaline pulping of non-wood feedstocks and characterization of black liquors. (54 pp.) 2001

88. Halonen, Markku: Lahon havupuun käyttö sulfaattiprosessin raaka-aineena sekä havupuun lahontorjunta. (90 pp.) 2002

89. Falábu, Dezsö: Synthesis, conformational analysis and complexation studies of resorcarene derivatives. (212 pp.) 2001

90. Lehtovuori, Pekka: EMR spectroscopic studies on radicals of ubiquinones Q-*n*, vitamin K_3 and vitamine E in liquid solution. (40 pp.) 2002

91. Perkkalainen, Paula: Polymorphism of sugar alcohols and effect of grinding on thermal behavior on binary sugar alcohol mixtures. (53 pp.) 2002

92. Ihalainen, Janne: Spectroscopic studies on light-harvesting complexes of green plants and purple bacteria. (42 pp.) 2002

93. Kunttu, Henrik, Kiljunen, Toni (Eds.): 4th International Conference on Low Temperature Chemistry. (159 pp.) 2002

94. Väisänen, Ari: Development of methods for toxic element analysis in samples with environmental concern by ICP-AES and ETAAS. (54 pp.) 2002

95. Luostarinen, Minna: Synthesis and characterisation of novel resorcarene derivatives. (200 pp.) 2002

96. Louhelainen, Jarmo: Changes in the chemical composition and physical properties of wood and nonwood black liquors during heating. (68 pp.) 2003

97. Lahtinen, Tanja: Concave hydrocarbon cyclophane B-prismands. (65 pp.) 2003

98. Laihia, Katri (Ed.): NBC 2003, Symposium on Nuclear, Biological and Chemical Threats – A Crisis Management Challenge. (245 pp.) 2003

99. Oasmaa, Anja: Fuel oil quality properties of wood-based pyrolysis liquids. (32 pp.) 2003

100. Virtanen, Elina: Syntheses, structural characterisation, and cation/anion recognition properties of nano-sized bile acid-based host molecules and their precursors. (123 pp.) 2003

101. Nättinen, Kalle: Synthesis and X-ray structural studies of organic and metallo-organic supramolecular systems. (79 pp.) 2003

102. Lampiselkä, Jarkko: Demonstraatio lukion kemian opetuksessa. (285 pp.) 2003

103. Kallioinen, Jani: Photoinduced dynamics of $Ru(dcbpy)_2(NCS)_2$ – in solution and on nanocrystalline titanium dioxide thin films. (47 pp.) 2004

104. Valkonen, Arto (Ed.): VII Synthetic Chemistry Meeting and XXVI Finnish NMR Symposium. (103 pp.) 2004

105. Vaskonen, Kari: Spectroscopic studies on atoms and small molecules isolated in low temperature rare gas matrices. (65 pp.) 2004

106. Lehtovuori, Viivi: Ultrafast light induced dissociation of $Ru(dcbpy)(CO)_2I_2$ in solution. (49 pp.) 2004

107. Saarenketo, Pauli: Structural studies of metal complexing schiff bases , Schiff base derived *N*-glycosides and cyclophane π-prismands. (95 pp.) 2004

108. Paasivirta, Jaakko (Ed.): CEOEC'2004, Sixth Finnish-Russian Seminar: Chemistry and Ecology of Organo-Element Compounds. (147 pp.) 2004

109. Suontamo, Tuula: Development of a test method for evaluating the cleaning efficiency of hard-surface cleaning agents. (96 pp.) 2004

110. Güneş, Minna: Studies of thiocyanates of silver for nonlinear optics. (48 pp.) 2004

111. Ropponen, Jarmo: Aliphatic polyester dendrimers and dendrons. (81 pp.) 2004

112. Vu, Mân Thi Hong: Alkaline pulping and the subsequent elemental chlorine-free bleaching of bamboo (*Bambusa procera*). (69 pp.) 2004

113. Mansikkamäki, Heidi: Self-assembly of resorcinarenes. (77 pp.) 2006

114. Tuononen, Heikki M.: EPR spectroscopic and quantum chemical studies of some inorganic main group radicals. (79 pp.) 2005

115. Kaski, Saara: Development of methods and applications of laser-induced plasma spectroscopy in vacuum ultraviolet. (44 pp.) 2005

116. Mäkinen, Riika-Mari: Synthesis, crystal structure and thermal decomposition of certain metal thiocyanates and organic thiocyanates. (119 pp.) 2006

117. Ahokas, Jussi: Spectroscopic studies of atoms and small molecules isolated in rare gas solids: photodissociation and thermal reactions. (53 pp.) 2006

118. Busi, Sara: Synthesis, characterization and thermal properties of new quaternary ammonium compounds: new materials for electrolytes, ionic liquids and complexation studies. (102 pp.) 2006

119. Mäntykoski, Keijo: PCBs in processes, products and environment of paper mills using wastepaper as their raw material. (73 pp.) 2006

120. Laamanen, Pirkko-Leena: Simultaneous determination of industrially and environmentally relevant aminopolycarboxylic and hydroxycarboxylic acids by capillary zone electrophoresis. (54 pp.) 2007

121. Salmela, Maria: Description of oxygen-alkali delignification of kraft pulp using analysis of dissolved material. (71 pp.) 2007

122. Lehtovaara, Lauri: Theoretical studies of atomic scale impurities in superfluid ^{4}He. (87 pp.) 2007

123. Rautiainen, J. Mikko: Quantum chemical calculations of structures, bonding, and spectroscopic properties of some sulphur and selenium iodine cations. (71 pp.) 2007

124. Nummelin, Sami: Synthesis, characterization, structural and retrostructural analysis of self-assembling pore forming dendrimers. (286 pp.) 2008

125. Sopo, Harri: Uranyl(VI) ion complexes of some organic aminobisphenolate ligands: syntheses, structures and extraction studies. (57 pp.) 2008

126. Valkonen, Arto: Structural characteristics and properties of substituted cholanoates and *N*-substituted cholanamides. (80 pp.) 2008

127. Lähde, Anna: Production and surface modification of pharmaceutical nano- and microparticles with the aerosol flow reactor. (43 pp.) 2008

128. Beyeh, Ngong Kodiah: Resorcinarenes and their derivatives: synthesis, characterization and complexation in gas phase and in solution. (75 pp.) 2008

129. Välisaari, Jouni, Lundell, Jan (Eds.): Kemian opetuksen päivät 2008: uusia oppimisympäristöjä ja ongelmalähtöistä opetusta. (118 pp.) 2008

130. Myllyperkiö, Pasi: Ultrafast electron transfer from potential organic and metal containing solar cell sensitizers. (69 pp.) 2009

131. Käkölä, Jaana: Fast chromatographic methods for determining aliphatic carboxylic acids in black liquors. (82 pp.) 2009

132. Koivukorpi, Juha: Bile acid-arene conjugates: from photoswitchability to cancer cell detection. (67 pp.) 2009

133. Tuuttila, Tero: Functional dendritic polyester compounds: synthesis and characterization of small bifunctional dendrimers and dyes. (74 pp.) 2009

134. Salorinne, Kirsi: Tetramethoxy resorcinarene based cation and anion receptors: synthesis, characterization and binding properties. (79 pp.) 2009

135. Rautiainen, Riikka: The use of first-thinning Scots pine (*Pinus sylvestris*) as fiber raw material for the kraft pulp and paper industry. (73 pp.) 2010

136. Ilander, Laura: Uranyl salophens: synthesis and use as ditopic receptors. (199 pp.) 2010

137. Kiviniemi, Tiina: Vibrational dynamics of iodine molecule and its complexes in solid krypton - Towards coherent control of bimolecular reactions? (73 pp.) 2010

138. Ikonen, Satu: Synthesis, characterization and structural properties of various covalent and non-covalent bile acid derivatives of N/O-heterocycles and their precursors. (105 pp.) 2010

139. Siitonen, Anni: Spectroscopic studies of semiconducting single-walled carbon nanotubes. (56 pp.) 2010

140. Raatikainen, Kari: Synthesis and structural studies of piperazine cyclophanes – Supramolecular systems through Halogen and Hydrogen bonding and metal ion coordination. (69 pp.) 2010

141. Leivo, Kimmo: Gelation and gel properties of two- and three-component Pyrene based low molecular weight organogelators. (116 pp.) 2011

142. Martiskainen, Jari: Electronic energy transfer in light-harvesting complexes isolated from *Spinacia oleracea* and from three photosynthetic green bacteria *Chloroflexus aurantiacus*, *Chlorobium tepidum*, and *Prosthecochloris aestuarii*.(55 pp.) 2011

143. Wichmann, Oula: Synthesis, characterization and structural properties of [O,N,O,X´] aminobisphenolate metal complexes. (101 pp.) 2011

144. Ilander, Aki: Development of ultrasound-assisted digestion methods for the determination of toxic element concentrations is ash samples by ICP-OES. (58 pp.) 2011

145. The Combined XII Spring Meeting of the Division of Synthetic Chemistry and XXXIII Finnish NMR Symposium. Book of Abstracts. (90 pp.) 2011

146. Valto, Piia: Development of fast analysis methods for extractives in papermaking process waters. (73pp.) 2011